CHEMICAL REVIEWS

Review

Cite This: Chem. Rev. XXXX, XXX, XXX−XXX

pubs.acs.org/CR

Thermoelectrics of Nanowires

Renkun Chen,[†] Jaeho Lee,[‡] Woochul Lee,[§] and Deyu Li*[,∥]

[†]Department of Mechanical and Aerospace Engineering, The University of California—San Diego, La Jolla, California 92093, United States

[‡]Department of Mechanical and Aerospace Engineering, The University of California—Irvine, Irvine, California 92697, United States

[§]Department of Mechanical Engineering, The University of Hawaii at Manoa, Honolulu, Hawaii 96822, United States

[∥]Department of Mechanical Engineering, Vanderbilt University, Nashville, Tennessee 37235-1592, United States

ABSTRACT: The field of thermoelectric research has undergone a renaissance and boom in the past two and a half decades, largely fueled by the prospect of engineering electronic and phononic properties in nanostructures, among which semiconductor nanowires (NWs) have served both as an important platform to investigate fundamental thermoelectric transport phenomena and as a promising route for high thermoelectric performance for diverse applications. In this Review, we provide a comprehensive look at various aspects of thermoelectrics of NWs. We start with a brief introduction of basic thermoelectric phenomena, followed by synthetic methods for thermoelectric NWs and a summary of their thermoelectric figures of merit (ZT). We then focus our discussion on charge and heat transport, which dictate thermoelectric power factor and thermal conductivity, respectively. For charge transport, we cover the basic principles governing the power factor and then review several strategies using NWs to enhance it, including earlier theoretical and experimental work on quantum confinement effects and semimetal-to-semiconductor transition, surface engineering and complex heterostructures to enhance the carrier mobility and power factor, and the recent emergence of topological insulator NWs. For phonon transport, we broadly categorize the work on thermal conductivity of NWs into five different effects: classic size effect, acoustic softening, surface roughness, complex NW morphology, and dimensional crossover. Finally, we discuss the integration of NWs for device applications for thermoelectric power generation and cooling. We conclude our review with some outlooks for future research.

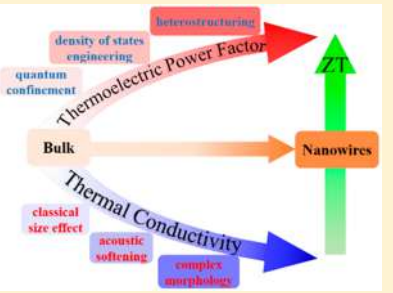

CONTENTS

Special Issue: 1D Nanomaterials/Nanowires

Received: October 15, 2018

DOI: 10.1021/acs.chemrev.8b00627
Chem. Rev. XXXX, XXX, XXX−XXX

1. INTRODUCTION

The intensive research on thermoelectrics in the past two and a half decades was largely inspired by the seminal work by Dresselhaus et al. in 1993, which predicted that quantum confinement effects can lead to a drastically enhanced thermoelectric power factor in low-dimensional materials.[1] It was also quickly realized that the thermal conductivity of nanowires could be reduced remarkably, and that the combined effects of enhanced power factor and reduced thermal conductivity provide an extremely promising route to achieve high thermoelectric figures of merit (ZT), as depicted in Figure 1.[2,3] These insights motivated extensive efforts on a full spectrum of research spanning nanowire synthesis, property characterization, and device integration. To date, tremendous progress has been made in terms of the design and fabrication of nanowires as well as understanding their thermoelectric properties.[4−6] However, limited by several key challenges, the goal of demonstrating $ZT > 4$ to make thermoelectric devices more competitive economically than current power generation and refrigeration systems still has not been achieved, which leaves rich opportunities for groundbreaking discoveries in the research field of thermoelectrics of nanowires.

Thermoelectrics describes direct conversion between thermal and electrical energy, which encompasses three separately identified physical phenomena: the Seebeck effect, the Peltier effect, and the Thomson effect.[7,8] Nearly two centuries ago, in 1821−1823, Thomas Seebeck first observed that a magnetic field was generated if two dissimilar conductors were attached together and one of the junctions was heated. What he really found is that a temperature gradient across certain materials will create a voltage drop between the hot and cold ends. The Seebeck coefficient S, named after him, describes the thermoelectric voltage change rate with respect to temperature at a given temperature. A more convenient parameter is the relative Seebeck coefficient, usually simply called Seebeck coefficient, defined as

$$S_{ab} = \frac{dV}{dT} \tag{1}$$

As shown in Figure 2a, S_{ab} is the relative Seebeck coefficient between materials a and b, V is the voltage drop, and T is temperature.

A complementary effect was found by Peltier in 1835 (Figure 2b). He observed temperature changes at the junctions between two dissimilar conductors through which an electrical current was passed. This effect is now called the Peltier effect. The temperature change is directly proportional to the current and a Peltier coefficient Π_{ab}, defined as

$$Q = \Pi_{ab} I \tag{2}$$

Here Q is the heat flow rate at the junctions and I is the electrical current. Later, in 1851, W. Thomson (Lord Kelvin) established a relationship between the Seebeck and Peltier coefficients and predicted a third thermoelectric effect, the Thomson effect, which he subsequently confirmed experimentally. The Thomson effect describes the heating or cooling of a single homogeneous conductor when a current is passed through the material in the presence of a fixed temperature gradient. This is attributed to the fact that the Seebeck coefficient S is temperature dependent. The magnitude of the additional heat flux, which is proportional to both the temperature gradient and the current, is given by

$$\nabla q'' = \tau J \nabla T \tag{3}$$

where q'' is the heat flux, τ is the Thomson coefficient, and J is the current density. Kelvin's theoretical derivation relates the Seebeck and Peltier effects and shows that

$$\tau_a - \tau_b = T\frac{dS_{ab}}{dT} \tag{4}$$

and

$$\Pi_{ab} = S_{ab} T \tag{5}$$

As can be seen from these thermoelectric effects, thermoelectrics can be used for both electrical power generation and refrigeration. The performance of thermoelectric devices is determined by a figure of merit, ZT, that can be written as $ZT = S^2\sigma T/\kappa$, where σ and κ are the electrical and thermal conductivities, respectively. The thermoelectric figure of merit is roughly proportional to efficiency. A ZT of 1 corresponds to ~10% of Carnot efficiency, and ZT approaches ∞ for 100% of Carnot efficiency. If ZT were to be increased to about 4, thermoelectric coolers could operate at ~30% of Carnot efficiency, which would be comparable to current phase-change-based refrigerators. Increasing ZT is difficult because the three parameters, S, σ, and κ, are all related to the free charge carrier concentration and are not independent. Generally speaking, doping increases a semiconductor's electrical conductivity but decreases its Seebeck coefficient. Heat transport in a semiconductor is carried by both electrons and lattice vibrations (represented by quasi-particles called phonons). Adding free electrons not only decreases the Seebeck coefficient but also causes the thermal conductivity to increase. In addition, efforts to reduce the lattice thermal conductivity could also reduce the electrical conductivity by providing extra scattering mechanisms.

After these thermoelectric effects were discovered, the field developed slowly over about one century, with the conclusion that thermoelectric refrigeration and power generation were uneconomical, except for certain niche applications, by the early 20th century. Most work at that time was on metallic materials. Interest in thermoelectricity was renewed in the 1950s, when researchers discovered that semiconductors possessed much better thermoelectric properties than metals. Nearly all known semiconductor materials were examined for potential use as thermoelectric elements. By the end of the 1950s, the best thermoelectric materials were found to be alloys of bismuth tellurides and antimony, which gave a room-temperature ZT of about unity. Only marginal improvements were made over the next 40 years.

The stagnation in thermoelectric research was again broken in 1990s, with the discovery that nanoconfinement effects in low-dimensional materials can drastically enhance ZT; nanowires were identified as one class of promising materials that could produce transformative impacts.[2,3] In the following sections, we will review progress in the synthesis of various nanowires for thermoelectric applications, characterization of the electrical and thermal properties of nanowires, and integration of nanowires for thermoelectric devices. Importantly, in view of the significant insights obtained in nanowire research, we will also discuss their implications in the design of

DOI: 10.1021/acs.chemrev.8b00627
Chem. Rev. XXXX, XXX, XXX−XXX

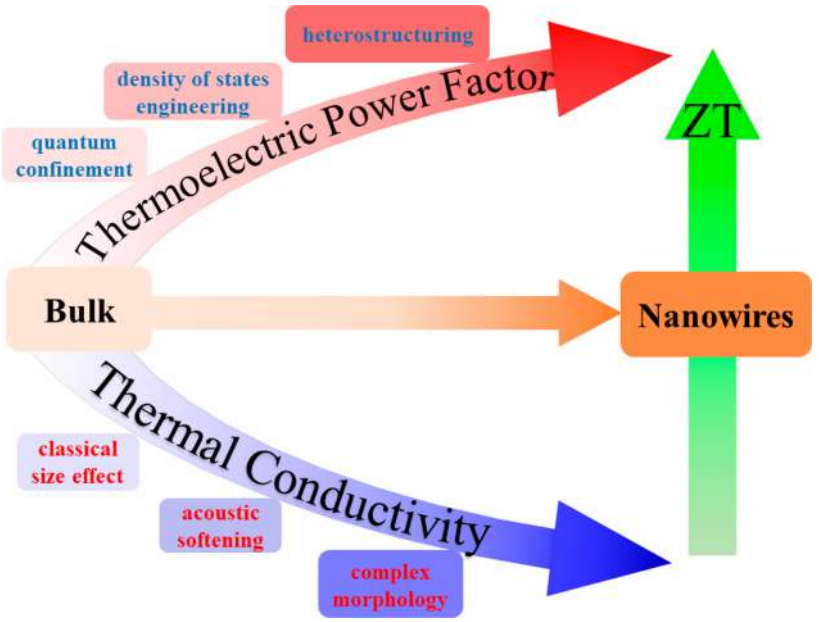

Figure 1. Nanowires can have significantly enhanced *ZT* because of the higher thermoelectric power factor achieved through quantum confinement, density of states engineering, and heterostructuring, as well as the lower thermal conductivity owing to the classical size effect, acoustic softening, and complex morphology. These factors are detailed in this Review.

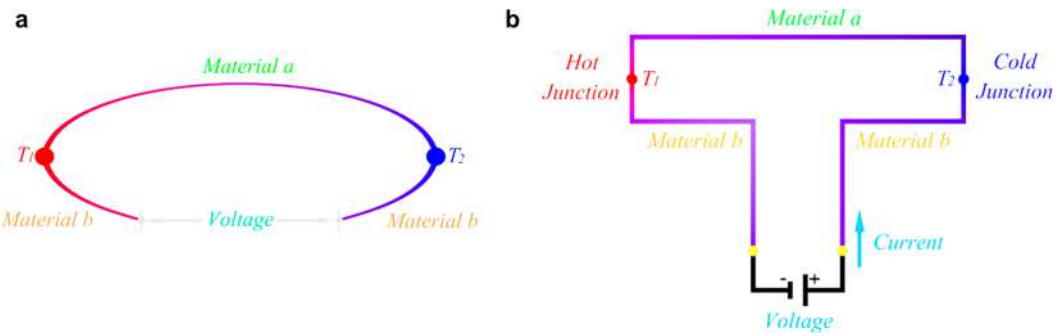

Figure 2. (a) Schematic of the Seebeck effect. An electrical voltage is generated when two dissimilar conductors are attached together with the two ends at different temperatures. (b) Schematic of the Peltier effect. A temperature change at the junction between two dissimilar conductors occurs when an electrical current is passed through the junction.

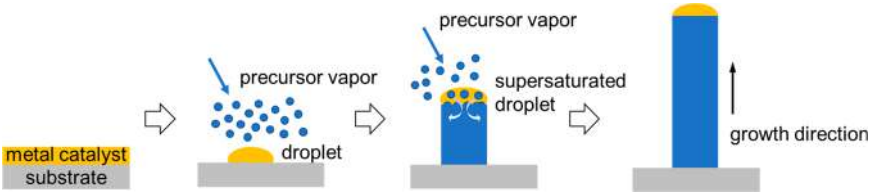

Figure 3. Schematic of the synthesis of nanowire arrays by the VLS method. Nanowires are grown epitaxially on a substrate at the bottom of the catalyst particles.

other thermoelectric materials, such as nanomeshes. We will conclude the review with a summary and outlook.

2. TYPES OF NANOWIRES FOR THERMOELECTRIC APPLICATIONS

2.1. Preparation of Nanowires for Thermoelectric Applications

Over the past two decades, a variety of methods for preparation of nanowires (NWs) have been demonstrated with controlled composition, crystallinity, and morphology,[9] which have led to diverse transport properties and have inspired many NW-based device applications, particularly in thermoelectric cooling and power generation.[10] Details of NW preparation methods, including bottom-up and top-down approaches, are available in the literature.[11−13]

For thermoelectric applications, bottom-up approaches based on vapor−liquid−solid (VLS) growth, solution−liquid−solid (SLS) growth, chemical vapor deposition (CVD), electrospinning, and electrochemical deposition have provided a wide variety of NWs and offered advantages in controlling phase purity, crystallinity, NW density, and dimensions. For instance, the VLS method (Figure 3)[14,15] can produce epitaxially aligned single-crystalline NWs, and

DOI: 10.1021/acs.chemrev.8b00627
Chem. Rev. XXXX, XXX, XXX−XXX

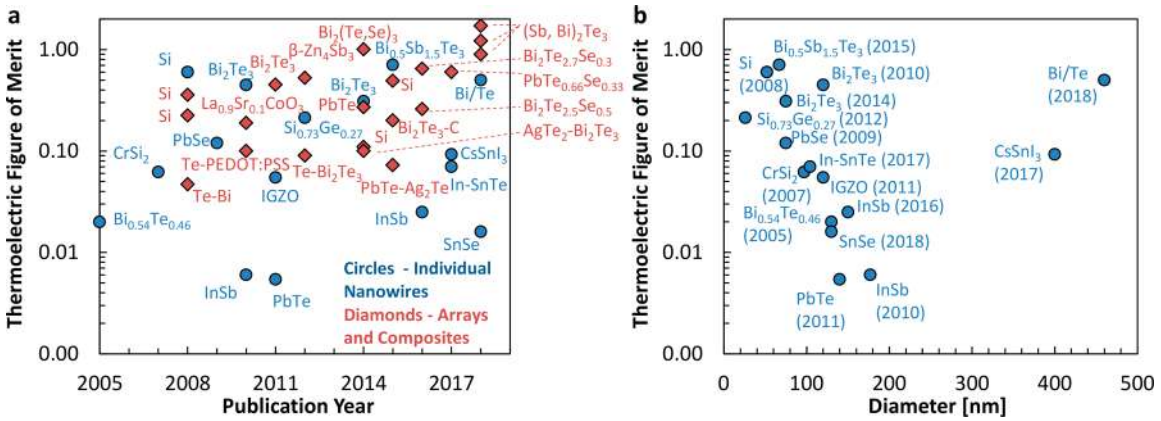

Figure 4. Reported thermoelectric figures of merit (ZT) of representative nanowires at room temperature, (a) in chronological order and (b) as a function of wire diameter. The investigated individual nanowires include $Bi_{0.54}Te_{0.46}$,[31] $CrSi_2$,[38] Si,[33] PbSe,[27] Bi_2Te_3,[44,45] InSb,[46] IGZO,[53] PbTe,[47] $Si_{0.73}Ge_{0.27}$,[43] $Bi_{0.5}Sb_{1.5}Te_3$,[32] InSb,[48] $CsSnI_3$,[49] SnTe,[50] Bi/Te,[51] and SnSe.[52] The investigated nanowire arrays and composite materials include Si NW arrays,[35,36,39] Te/Bi core/shell composites,[54] Te NW-PEDOS:PSS hybrid,[55] Bi_2Te_3 composites,[28] β-Zn_4SB_3,[56] Te-Bi_2Te_3,[57] $AgTe_2$-Bi_2Te_3,[58] PbTe,[29] $La_{0.9}Sr_{0.1}CoO_3$,[59] $Bi_2(Te,Se)_3$,[60] PbTe-Ag_2Te,[30] Bi_2Te_3-graphene,[61] $Bi_2Te_{2.7}Se_{0.3}$ alloys,[62] Sb_2Se_3 NW bundles,[63] $Bi_2Te_{2.5}Se_{0.5}$,[64] $PbTe_{0.66}Se_{0.33}$,[65] and $(Sb,Bi)_2Te_3$.[66] The search for high ZT in NWs has continued to make progress, and NWs combined with heterostructuring and strain engineering have led to further improvements. While most of thermoelectric NWs focused on reducing the size in the past, some of recent NWs have achieved high ZT with relatively large diameters[49,51] due to the combination of inherently short phonon mean free path and high power factor.

using directed colloid seeding, precise control over NW diameter, growth density, and spatial distribution is possible.[16] The synthetic procedure typically starts with the deposition of metal catalyst on a substrate, which is required for VLS growth. The metal catalyst is then converted to a liquid alloy droplet by adsorbing the vapor component at a high temperature. Once the alloy droplet is supersaturated, a one-dimensional (1D) crystalline NW starts to grow at the liquid−solid interface by precipitation of the vapor component. The growth continues until the vapor component is no longer available. As the name of VLS suggests, vapor, liquid, and solid phases are all involved during the synthesis process. In terms of the role of each phase, vapor carries the component to create the NW structure, while the liquid alloy droplet is the catalyst and the solid phase is the synthesized NW. VLS-grown Si NWs led to the first experimental study of the classical size effects on the thermal conductivity of individual NWs.[17]

The VLS method is not only well-suited for creating homogeneous and high-purity NWs, such as Si and Ge NWs, but also capable of producing complex heterostructures,[18] which are often preferred for thermoelectric applications.[19] Additionally, the VLS method can be combined with pulsed laser ablation[20] and HF vapor etching[21] to create more complex structures such as superlattice NWs[22] and rough surface NWs,[21] respectively, which showed more significant thermal conductivity reduction. Other variations of VLS method such as iterative control over nucleation and growth can lead to complex structures such as kinked NWs,[23] which are also predicted to offer attractive thermoelectric properties.[24]

Another widely used bottom-up approach is based on SLS or solution-phase synthesis, and it offers advantages in systematically scaling down NW dimensions, controlling surface passivation, and producing large amounts of NWs at low costs. Because of the relatively low NW growth temperature and the limited growth rate in the SLS method, the resulting NW diameter and diameter distribution can be more precisely controlled. SLS-grown InAs NWs of diameters down to 5 nm were demonstrated, which enabled studies of quantum confinement of charge carriers[25] that has long been predicted to enhance thermoelectric properties.[1] In a separate study, oscillations of thermopower and thermoelectric power factor were observed near 40 K, along with stepwise increase in electrical conductance, as the Fermi level swept through the 1D electronic sub-bands by changing the gate voltage.[26] The thermal conductivity of solution-phase synthesized PbSe NWs showed a nearly 2-fold reduction compared to the bulk counterpart, but their thermopower was also low due to process dependent point defects.[27] Enabled by the high production yield and excellent growth controllability, a variety of solution-synthesized NWs have been consolidated into pellets via spark plasma sintering and characterized in the bulk form. The NW pellets of traditional thermoelectric materials such as Bi_2Te_3,[28] PbTe,[29] and Ag_2Te[30] showed strongly reduced thermal conductivity while maintaining the bulk-like Seebeck coefficient and electrical conductivity.

For conventional thermoelectric materials based on chalcogenide semiconductors, template-based methods are widely used for creating NWs. Nanoporous templates, often based on anodic aluminum oxide with 1D cylindrical channels, are used with electrochemical deposition. Electrochemical deposition offers simplicity, low cost, and low process temperature, but it could lead to relatively low crystal quality in the resulting NWs. In an early study, electrochemically deposited bismuth telluride NWs[31] showed reduced thermopower factor, and a later study showed that pulsed electrochemical deposition improved the crystalline quality and ZT.[32]

The bottom-up approaches are considered more attractive for micro- and nanoscale thermoelectric applications because of the scalability that can potentially overcome the resolution limits and other constraints of conventional top-down fabrication techniques. The possibility of creating high-density NW arrays and the material flexibility are also advantageous. On the other hand, top-down approaches, which rely on lithographic methods and etching processes, are well-suited for integrating with three-dimensional (3D) systems, hierarchical assemblies, and large-scale implementation. Si NWs created by both metal-assisted chemical etching (MACE)[33] and super-

DOI: 10.1021/acs.chemrev.8b00627
Chem. Rev. XXXX, XXX, XXX−XXX

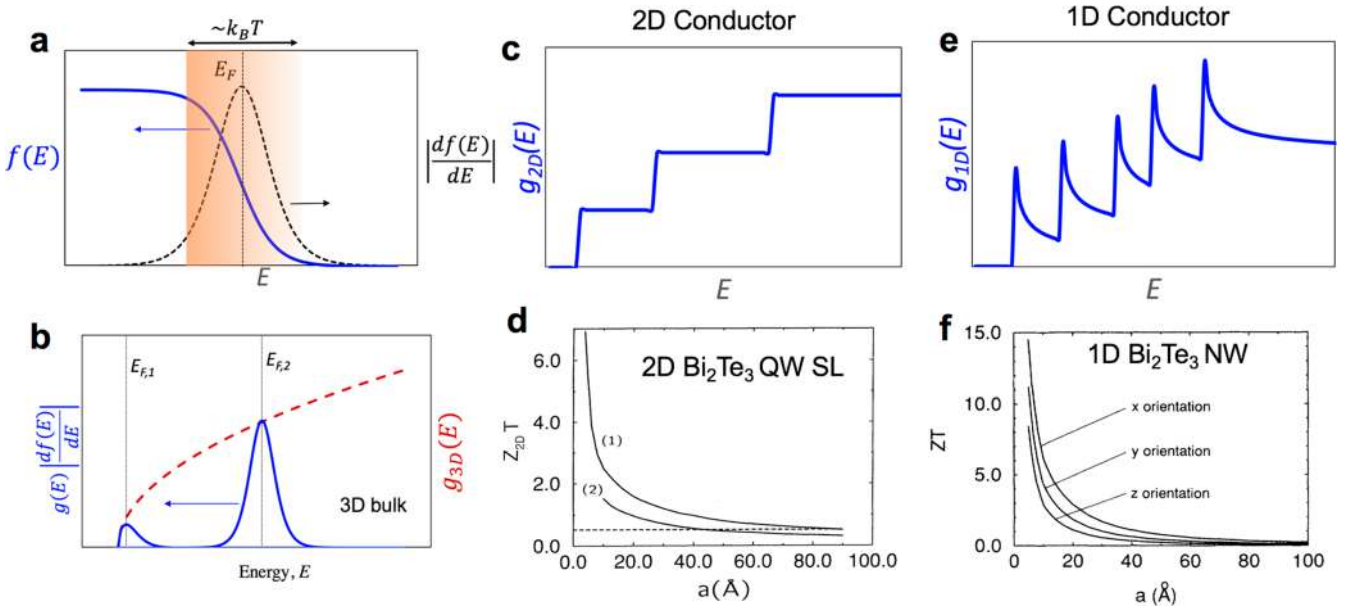

Figure 5. (a) Fermi−Dirac distribution function $f(E)$ (solid line, left axis) and its derivative $\left|\frac{df(E)}{dE}\right|$ (dashed line, right axis) as a function of energy E. The shaded area indicates the small energy window, on the order of k_BT, within which f changes from 1 to 0 and the derivative is non-zero (i.e., contributes to charge transport). (b) The product $g(E)\left|\frac{df(E)}{dE}\right|$ (solid line, left axis) in 3D with different Fermi energies, where the dashed line is the $g(E)$ for 3D (eq 9). A lower Fermi energy ($E_{F,1}$) has a lower $g(E)\left|\frac{df(E)}{dE}\right|$ product but a more asymmetric $g(E)$ around it, leading to low σ and high S. In contrast, a higher Fermi energy ($E_{F,2}$) has a higher product but a less asymmetric $g(E)$ around it, resulting in high σ and low S. (c) Density of states (DOS) as a function of the energy in a 2D conductor (e.g., a quantum well, QW). (d) Plot of $ZT(\eta_{opt})$ as a function of individual layer thickness a of Bi_2Te_3 QW superlattices (SLs, solid lines) calculated by Hicks and Dresselhaus,[1] where η_{opt} is the optimal value for the reduced chemical potential η. Curve (1) indicates the direction along the a_0-b_0 ($x-y$) plane, and curve (2) is along the a_0-c_0 ($x-z$) plane; dashed line is for bulk Bi_2Te_3. Reprinted with permission from ref 1. Copyright 1993 American Physical Society. (e) DOS as a function of the energy in a 1D conductor (e.g., a nanowire, NW). (f) Plot of $ZT(\eta_{opt})$ as a function of width a of Bi_2Te_3 NWs along x, y, z orientations, calculated by Hicks and Dresselhaus.[68] Reprinted with permission from ref 68. Copyright 1993 American Physical Society.

lattice nanowire pattern transfer (SNAP)[34] demonstrated a significant reduction in thermal conductivity without sacrificing electrical conductivity or Seebeck coefficient, leading to substantially enhanced ZT. Studies using the MACE method showed that individual NW properties were sustained in large-area NW arrays and demonstrated Si-NW-array-based thermoelectric generators.[35,36]

2.2. Survey of the Reported Nanowire Thermoelectric Figures of Merit

Since the establishment of individual NW measurement technique based a suspended microbridge device in 2003,[37] the ZT of individual NWs has been characterized for various materials (Figure 4). Shi and co-workers first reported the ZT of individual $Bi_{0.54}Te_{0.46}$ NWs[31] in 2005 and $CrSi_2$ NWs[38] in 2007 by combining separate measurements of the Seebeck coefficient and of electrical and thermal conductivities, respectively. Because chalcogenide and silicide materials have inherently short phonon mean free paths (MFPs), the thermal conductivity reduction was small, and the nanowire ZT values were not better than their bulk counterparts. In 2008, Hochbaum et al.[33] demonstrated that the ZT of individual rough Si NWs created by the MACE method was much greater than that of bulk Si, with a value of 0.6 at room temperature, due to a 100-fold reduction in thermal conductivity. At the same time, Boukai et al.[39] also reported high ZT in horizontal Si NW arrays produced by the SNAP method with the reported ZT of Si NWs as high as 1 at 200 K.[39] The ZT of Si NWs is expected to further increase at higher temperatures[40] and by optimizing doping and roughness conditions.[41,42] The individual NW properties were sustained in large-area NW arrays, and the vertically oriented Si NW arrays showed ZT of 0.11[35] and 0.49[36] at room temperature. While thermal conductivity reduction in NW is conducive to enhancing ZT, NWs are susceptible to trap states and defects, which can lead to low carrier mobility and low ZT. Liang et al.[27] showed thermal annealing improves the carrier mobility and reported that the ZT of PbSe NWs could be up to 0.12 at room temperature. Alloying as well as nanostructuring has been proven effective in improving ZT, too. Lee et al. characterized individual $Si_{0.73}Ge_{0.27}$ NWs and showed a ZT of 0.21 at room temperature and a peak ZT of 0.46 at 450 K.[43] Thermal conductivity measurements showed that the impact of Ge concentration or the alloy scattering is more important than the diameter or the boundary scattering in SiGe NWs.[21]

The size effect on thermal transport in materials that are conventionally known as good bulk thermoelectric materials is generally weak, and the ZT enhancement in NWs compared to bulk is not evident as shown in reports for individual NWs of Bi_2Te_3,[44,45] InSb,[46] PbTe,[47] $Si_{0.73}Ge_{0.27}$,[43] $Bi_{0.5}Sb_{1.5}Te_3$,[32] InSb,[48] $CsSnI_3$,[49] SnTe,[50] Bi/Te,[51] and SnSe.[52] However, the reported ZT data for NWs (Figure 4b) still demonstrate a trend of higher ZT values for smaller diameter NWs. Recently, some NWs have achieved high ZT with relatively large diameters[49,51] due to the combination of inherently short phonon MFP and high power factor. For example, Lee et al.

DOI: 10.1021/acs.chemrev.8b00627
Chem. Rev. XXXX, XXX, XXX−XXX

showed halide perovskite NWs possess ultra-low thermal conductivity due to cluster rattling motions and the possibility of developing efficient thermoelectric materials in inorganic crystals.[49] Kim et al. showed Bi NWs have a large ZT even with a large diameter (>400 nm) due to strain-induced allotropic transformation and enhanced Seebeck coefficient.[51]

3. ELECTRICAL PROPERTIES OF THERMOELECTRIC NANOWIRES

The interdependence of thermoelectric parameters has been one of the major barriers for achieving high ZT. Engineering material properties using the classic and quantum size effects emerged as a promising strategy to decouple the transport parameters for boosting ZT. In this section, we will review the basic principles dictating the thermoelectric power factor, namely, electrical conductivity (σ) and Seebeck coefficient (S). We will then briefly cover some historical accounts regarding the strategies to enhance the power factor, which can be dated back to the original quantum confinement effect and density of states (DOS) engineering proposed in the seminal landmark paper by Hicks and Dresselhaus.[1] Finally, we will focus on reviewing experimental and computational work covering thermoelectric power factor of several representative NW materials and structures, including Bi and $Bi_{1-x}Sb_x$ alloys, Group IV (Si, Ge, and $Si_{1-x}Ge_x$ alloys), radial core−shell heterostructures, radial inhomogeneous doping, and topological insulator NWs (e.g., bismuth chalcogenides Bi_2Te_3 and Bi_2Se_3 and their alloys).

3.1. Basic Principles

To understand various effects on the thermoelectric power factor, we can first examine the basic parameters leading to electrical conductivity (σ) and Seebeck coefficient or thermopower (S), e.g., through Boltzmann transport equations (BTE):[187]

$$\sigma = \frac{e^2}{3}\int g(E)v^2(E)\tau(E,T)\left(-\frac{\partial f(E)}{\partial E}\right)\mathrm{d}E \tag{6}$$

and

$$S = \frac{k_B}{e}\left[\frac{\int_0^\infty g(E)v^2(E)\frac{E-E_F}{k_BT}\tau(E,T)\left(-\frac{\partial f(E)}{\partial E}\right)\mathrm{d}E}{\int_0^\infty g(E)v^2(E)\tau(E,T)\left(-\frac{\partial f(E)}{\partial E}\right)\mathrm{d}E}\right] \tag{7}$$

where e is the elementary electron charge, k_B is the Boltzmann constant, $g(E)$ is the total electronic DOS, E_F is the Fermi energy, $v(E)$ is the electron velocity at energy E, $\tau(E,T)$ is the relaxation time of electrons at energy E and temperature T, and $f(E)$ is the energy distribution function, which for charge carriers is the Fermi−Dirac distribution function, namely,

$$f(E) = 1/\left(\exp\left(\frac{(E-E_F)}{k_BT}\right)+1\right) \tag{8}$$

The derivative of the Fermi−Dirac distribution with respect to energy, $-\frac{\partial f(E)}{\partial E}$, has a peak at the Fermi level and diminishes exponentially when E is $\sim 5k_BT$ away from E_F, as shown in Figure 5a. Therefore, only electrons and holes with energy close to E_F contribute to electrical and thermoelectric transport.

Equations 6 and 7 indicate that σ is proportional to the integral of the product $g(E)\left(-\frac{\partial f}{\partial E}\right)$, whereas S is proportional to the integral of the product $(E-E_F)g(E)\left(-\frac{\partial f}{\partial E}\right)$. In bulk (3D) semiconductors, $g(E)$ generally scales as $\sqrt{E}$ (including a spin-degeneracy factor of 2):

$$g(E) = \frac{1}{2\pi^2}\left(\frac{2m^*}{\hbar^2}\right)^{3/2}(E-E_C)^{1/2} \tag{9}$$

where m^* is the DOS effective mass of the charge carrier and $\hbar$ is the reduced Planck constant. The DOS $g_{3D}(E)$ as a function of $(E-E_c)$ for a bulk conductor is schematically shown in Figure 5b. For n-type conductors, $g_{3D}(E)$ increases gradually from 0 when energy increases from the conduction band energy minimum (E_c).

These equations and figures can help us understand several basic factors and their trade-offs influencing the thermoelectric power factor, including the doping concentration (n), effective mass (m^*), and carrier mobility (μ). First, the carrier concentration (n) in the conductor has contradicting effects on S and σ. As shown in Figure 5b, E_F increases for higher n (e.g., from $E_{F,1}$ to $E_{F,2}$ in Figure 5b), and the amplitude of $g(E)$ increases, leading to a larger product $g(E)\left|\frac{\partial f}{\partial E}\right|$, and consequently higher σ (eq 6). In the meantime, when E_F is higher, $g(E)$ as well as the product $(E-E_F)g(E)\frac{\partial f}{\partial E}$ is less asymmetric around E_F, causing a lower S (eq 7). The trade-off between S and σ leads to an optimal carrier concentration n and a peak power factor value for a given material, commonly seen in bulk semiconductors.

Second, the carrier scattering mechanisms, specifically the relaxation time (τ) and its energy dependence ($\tau(E)$), have pronounced effect on both σ and S, as shown in eqs 6 and 7, respectively. In practice, the relaxation time τ is manifested through the carrier mobility (μ), which is related to the average $\overline{\tau}$ weighted by eq 6, as

$$\mu = e\overline{\tau}/m^* \tag{10}$$

Therefore, σ is directly influenced by μ through τ (see eq 6). The influence of $\tau(E)$ on S can be seen in eq 7. If we explicitly consider the energy dependence of electron relaxation time and assume a power law scattering formula, $\tau(E) \sim E^r$, and also assume parabolic bands as $E = E_c + \hbar^2k^2/2m^*$ (for electrons) or $E = E_v - \hbar^2k^2/2m^*$ (for holes), we can reach the following compact equation for the power factor:[187]

$$S^2\sigma \propto \frac{E^r}{m^*}\left[\frac{E_F-E_C}{k_BT}+\left(r+\frac{5}{2}\right)\right]^2 \tag{11}$$

Equation 11 suggests that a larger r results in a higher maximum power factor. For typical semiconductors, r ranges from −1/2 for acoustic phonon scattering, 1/2 for optical phonon scattering, and 3/2 for impurity scattering. The benefit of a larger r on S can be physically understood by the preferential scattering of low-energy carriers,[67] which amplifies the asymmetry of the transport property around E_F. It should be noted that it is often unlikely to increase the mobility in a given bulk material, because the electron−phonon scattering is dictated by the intrinsic material properties and the material has to be doped to the optimal concentration, which gives rise to ionized impurity scattering.

Finally, the effective mass, m^* has complicated effects on the power factor and m^*/m_0 can have a large range of variations for different materials, from 0.01 to 2, where m_0 is the free

DOI: 10.1021/acs.chemrev.8b00627
Chem. Rev. XXXX, XXX, XXX−XXX

electron mass. On one hand, a larger effective mass reduces the mobility and the conductivity (eq 10). On the other hand, a larger effective mass is generally beneficial for a higher Seebeck coefficient. It has been suggested that a smaller effective mass m^* is beneficial for the power factor, as shown in eq 11, if the other material parameters are not affected when m^* is changed. As an example, Pei et al. showed an enhanced power factor in PbTe due to lighter effective hole mass.[69]

3.2. Quantum Confinement Effect and DOS Engineering in 1D Conductors

Due to the many complicated and often contradicting effects of several material parameters on S and σ, it has been extremely challenging to increase the thermoelectric power factor. As discussed earlier, the figure of merit ZT of thermoelectric materials had been largely stagnant for over 40 years since the discovery of bismuth tellurides and antimony tellurides in the 1950s. One strategy to break this limit is to use structures or materials with a density of states $g(E)$ deviated from the $\sqrt{E}$ dependence. In particular, if there is a resonance in $g(E)$ around E_F, the Seebeck coefficient and the power factor may be improved over the typical bulk values. In Mahan and Sofo's paper,[70] they showed that a δ-function-like transport distribution, $g(E)v_x^2(E)\tau(E)$, would maximize the power factor and ZT. In reality, "a Lorentzian of very narrow width" would most closely resemble the δ-function, as in the case of f-level electronic states in $YbAl_3$. Another notable example is the introduction of resonance in DOS through chemical doping. This "resonant doping" idea has been demonstrated in Tl-doped PbTe[71] and In-doped SnTe[72] and has been reviewed by Heremans et al.[73]

An alternative approach to modify the DOS, which is perhaps more controllable and generic, and hence more desirable for thermoelectrics, is based on quantum structures due to the quantum confinement effect. Since early 1990s, significant attentions have been turned to nanostructures and low-dimensional materials, in which the quantum confinement effect is suggested to engineer the electronic DOS in NWs (and more broadly in nanostructures). In 1993, Hicks and Dresselhaus wrote landmark papers suggesting the quantum confinement effect as a promising strategy to enhance the power factor and thermoelectric figure of merit in two-dimensional (2D) quantum-well structures[1] and 1D conductors.[68]

The basis of this enhancement can be understood by the sharp DOS at the low dimensions and the quantum confined sub-bands, which are qualitatively different from those of bulk (eq 9 and Figure 5b). For instance, within the parabolic band approximation, for a 1D conductor with a square cross section of a,[2] the electronic dispersion for free-electron-like motion along the x- direction and infinite potential barriers in the y- and z- directions is[68]

$$E(k_x) = \frac{\hbar\pi^2}{2a^2}\left(\frac{1}{m_y} + \frac{1}{m_z}\right) + \frac{\hbar k_x^2}{2m_x} \tag{12}$$

where m_i is the DOS effective mass along the i direction ($i = x, y, z$). When the size of the 1D conductor (a) is sufficiently small, the separation between two neighboring sub-bands will be larger than the k_BT spread of the $\left|\frac{df(E)}{dE}\right|$ window shown in Figure 5a, or

$$\frac{\hbar\pi^2}{2a^2}\frac{1}{\max(m_x, m_y)} > k_BT \tag{13}$$

In this case, the transport will be governed by one single sub-band, and consequently the Seebeck coefficient will be dictated by that sub-band only, which is expected to be higher than that in the bulk case. In a 3D conductor, S has contributions from energy levels both below and above E_F (namely, holes and electrons, respectively); see eq 7 and Figure 5a. In single sub-bands, however, there is only one sign of $(E - E_F)$ contributing to S (eq 7).

The DOSs, $g(E)$, for a single band in 2D and 1D systems are different from the bulk:

$$g_{2D}(E) = \frac{m^*}{\pi\hbar^2} \tag{14}$$

$$g_{1D}(E) = \frac{1}{\pi}\left(\frac{2m^*}{\hbar^2}\right)^{1/2} E^{-1/2} \tag{15}$$

The DOS are schematically displayed in Figure 5c,e for 2D and 1D conductors, respectively. In each of these cases, if the E_F is suitably located at an energy level that has a drastic change in $g(E)$, namely, within $\sim k_BT$ around the lowest occupied sub-band of the QW or quantum wire,[1,68,74] then the power factor could be drastically enhanced.

Based on assumptions of single sub-band transport and low-dimensional DOS, Hicks and Dresselhaus predicted very high ZT for 2D Bi_2Te_3 QW superlattices (SLs)[1] and 1D Bi_2Te_3 quantum wires, as shown in Figure 5d,f, respectively. In these plots, the shown ZT values were the peak ones for the optimized chemical potential (or doping concentration) at each a value. This can also be understood from the DOS diagrams in Figure 5c,e, which shows that only when E_F is properly located, namely, within $\sim k_BT$ around the lowest occupied sub-band, can the S and power factor be enhanced.

Quantum confinement effect itself has been unambiguously observed in several low-dimensional systems, such as quantum wells (2D electron gas),[75] quantum wires (1D electron gas),[76,77] and NWs.[18] The fingerprint of the quantum confinement effect is the stepwise change of the conductance (or conductance quantization) as the Fermi level, which is usually controlled by an electrostatic gate voltage, is shifted through various sub-bands.[18,77] In the cases where the thermopower was also measured, the thermopower would exhibit oscillation in conjunction with the stepwise increase in the conductance,[26] as one can expect from eq 7 and Figure 5c,e.

However, to our best knowledge, enhanced power factor due to the quantum confinement effect has not been experimentally observed in NWs. As nicely summarized by Wu et al.,[78] this is likely due to the following reasons: (i) Stringent requirement of sufficiently small diameter that is comparable to the de-Broglie wavelength, which is usually very challenging to obtain experimentally. For instance, for a ⟨110⟩ Ge NW, the diameter has to be less than 5 nm in order to observe truly 1D transport at room temperature, that is, the separation of the energy sub-bands is much larger than k_BT.[79] (ii) Even when there are clearly separated 1D sub-bands (similar to the one shown in Figure 5e), the Fermi level has to be located right at the vicinity of the peak DOS such that both the conductance and the thermopower, which is related to the slope of the DOS versus energy (eq 7), are simultaneously high. This would

DOI: 10.1021/acs.chemrev.8b00627
Chem. Rev. XXXX, XXX, XXX−XXX

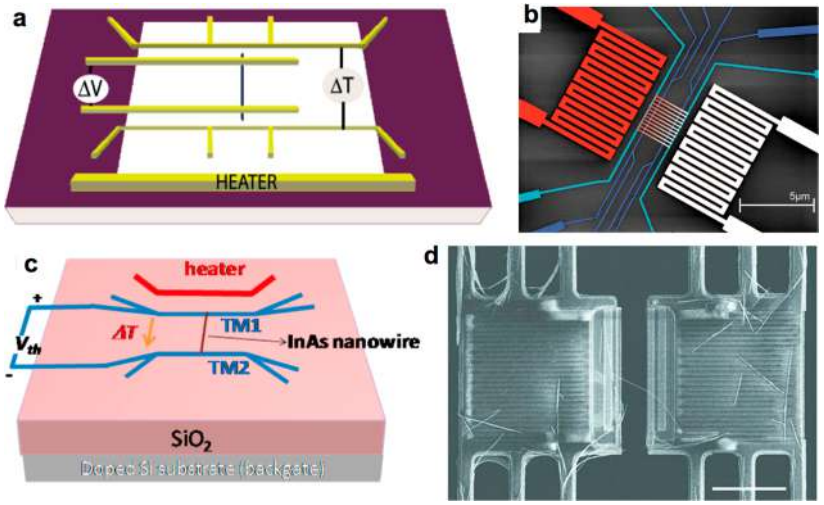

Figure 6. Representative device platforms for thermoelectric power factor (thermopower and electrical conductivity) measurements of individual nanowires or a known number of nanowires. In all these platforms, the electrical conductance is measured using standard two-probe or four-probe current−voltage (I−V) characterization, and the thermopower is measured by creating a temperature gradient along the wires with an on-chip microheater and measuring the temperature difference and thermo-voltage using the two inner electrodes that serve as both thermometers and voltage probes. (a) Schematic of the device used to measure power factor of carbon nanotubes by Llaguno et al.[83] The nanotube and the electrodes were placed on top of a thin and suspended membrane to generate a sufficiently large temperature gradient. Reprinted with permission from ref 83. Copyright 2004 American Chemical Society. (b) SEM image of the device used to measure power factor of Bi nanowire array by Boukai et al.[84] The Bi nanowires were patterned along with the electrodes to ensure good electrical contacts. The heater and voltage/temperature probes were patterned on a doped Si substrate, which also served as the gate electrode. Reprinted with permission from ref 84. Copyright 2006 Wiley. (c) Schematic of the device used to measure power factor of InAs nanowires by Tian et al.[26] using microfabricated heater and electrodes on a doped Si substrate. The nanowires were synthesized first and then transferred to the substrate. Reprinted with permission from ref 26. Copyright 2012 American Chemical Society. (d) SEM image of the device used to measure power factor of individual nanowire using a fully suspended device by Mavrokefalos et al.[93] The nanowires were transferred to the device and the electrical contact between the wires and the electrodes was enhanced using various techniques. The scale bar is 10 μm. Reprinted with permission from ref 93. Copyright 2009 American Institute of Physics.

require a precise control of the chemical doping or the use of the electrostatic gating, neither of which is easy to implement in NW systems. (iii) Even when the separation of 1D sub-bands is greater than k_BT (e.g., low temperature and/or materials with small effective mass) and when the Fermi level can be precisely tuned (e.g., using a gate voltage), scattering of charge carriers, which is inevitable due to NW surface and chemical impurities, could induce energy level broadening and could consequently smear out the 1D sub-bands, as in the case of InAs NWs we discussed earlier.[26] As such, the 1D effect is difficult to observe unless the wire is of very high quality and also very short length. Wu et al.[78] experimentally measured the power factor of InAs NWs and found oscillation of the power factor as well as enhancement over the corresponding bulk values at low temperatures. However, in their case, the oscillation and enhancement were attributed to the Coulomb blockade effect, namely, the quantum-dot like states formed in the electrostatically non-uniform NWs.[78]

In addition to engineering the DOS around the E_F in single valleys, there is also a clear advantage of increasing the valley degeneracy (N_V)—an approach termed "carrier pocket engineering".[80] This is because the DOS effective mass is related to N_V via $m^* = N_V^{2/3} m_b^*$, where m_b^* is the average DOS effective mass for a single valley, while the mobility μ usually is not affected by the increased N_V. This carrier pocket engineering approach was introduced by Dresselhaus and co-workers initially on $Bi_{1-x}Sb_x$ NWs, which was found to show coalescence of the extrema of all 10 hole pockets under suitable conditions.[80] The same approach was also theoretically investigated in GaAs/AlAs superlattices.[80] This idea was experimentally realized in bulk $PbTe_{1-x}Se_x$, which showed the convergence of the high-degeneracy and low-degeneracy hole pockets.[81]

3.3. Experimental Measurement Techniques

Before introducing thermoelectric transport behaviors of specific NW materials, here we will briefly summarize the common experimental techniques to measure thermoelectric power factor of NWs. In general, there are two categories of measurement techniques: first, on an ensemble of NWs, either in the form of aligned NW arrays or composites; second, on individual NWs or a known number of NWs (generally less than tens of NWs). The first category can be seen from earlier work on Bi and $Bi_{1-x}Sb_x$ NWs aiming to observe quantum confinement effects, as we shall discuss in section 3.4. These NWs were often fabricated in a nanoporous template with aligned pores, either through pressurized injection of molten materials or electrochemical deposition. The measurements were often realized via two-point electrical measurements; hence, the contact resistance might be non-trivial in some of the measurements.

The second category of measurements on individual NWs were more commonly seen in more recent literature, due to the advancement of micro- and nanofabrication techniques. Several variations of the measurement platforms have been developed for measurements of different materials and sometimes for specific measurement needs, as shown in Figure 6. In all these platforms, the electrical conductance is measured using standard two-probe or four-probe current−voltage (I−V) characterization, and the thermopower is measured by creating a temperature gradient along the wires with an on-chip microheater and measuring the temperature difference and thermo-voltage using the two inner electrodes that serve as

DOI: 10.1021/acs.chemrev.8b00627
Chem. Rev. XXXX, XXX, XXX−XXX

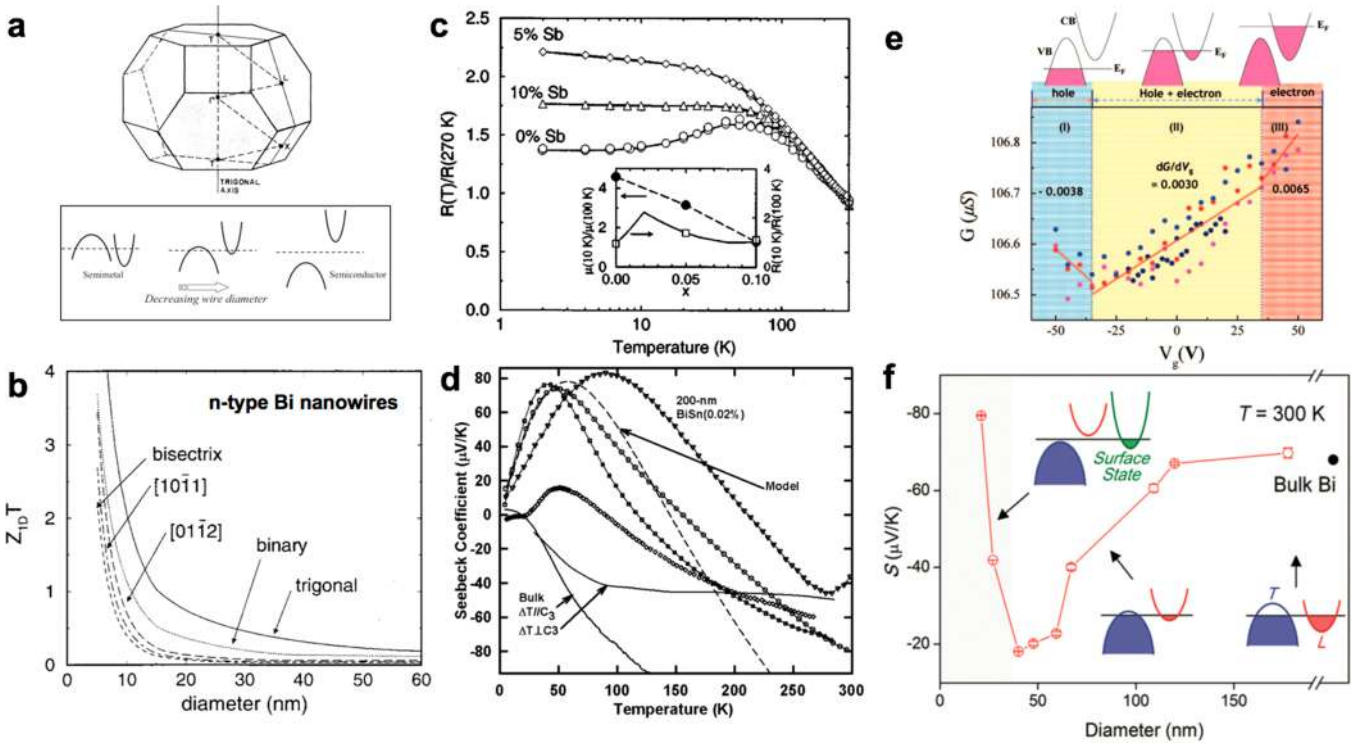

Figure 7. Thermoelectric power factor of Bi and $Bi_{1-x}Sb_x$ nanowires. (a) (Top) Brillouin zone of Bi, showing the T points (centers of the hexagonal faces) and L points (center of a pseudohexagonal face). Reprinted with permission from ref 107. Copyright 1968 American Physical Society. (Bottom) Schematic illustration of the semimetal−semiconductor (SMSC) transition in Bi and $Bi_{1-x}Sb_x$ nanowires: as the diameter decreases, the lowest conduction sub-band at the L-point moves up and the highest valence sub-band at the T-point moves down, creating a bandgap at a critical diameter. Reprinted with permission from ref 108. Copyright 2007 Wiley-VCH. (b) Calculated $Z_{1D}T$ values of n-type Bi nanowires as a function of diameter at 77 K, along different crystal orientations. Reprinted with permission from ref 99. Copyright 2000 American Physical Society. (c) Resistance of 65 nm diameter $Bi_{1-x}Sb_x$ nanowires (normalized to the resistance at 270 K) as a function of temperature of different Sb concentrations (x = 0, 5%, 10%). Reprinted with permission from ref 103. Copyright 2000 American Institute of Physics. (d) Measured thermopower of Bi nanowires with various diameters of 150, 240, and 480 nm (represented by open circles, squares, and diamonds, respectively). Reprinted with permission from ref 106. Copyright 2008 American Physical Society. (e) Ultra-high mobility (76 900 $cm^2/V{\cdot}s$) in a 120 nm diameter Bi nanowire grown from the OFF-ON method, as extracted from the field effect measurements (conductance G vs gate voltage V_g). Reprinted with permission from ref 109. Copyright 2009 American Chemical Society. (f) Diameter-dependent thermopower of Bi nanowire grown from the OFF-ON method. Reprinted with permission from ref 89. Copyright 2015 Royal Society of Chemistry.

both thermometers and voltage probes. In many cases (Figure 6a−c), the power factor measurements have been often utilized in a field-effect transistor configuration, where the carrier concentration in the NWs can be modulated by electrostatic gating. The fabrication and measurement strategies can be traced back to earlier studies on carbon nanotubes (NTs), e.g., by Small et al.[82] and Llaguno et al.[83] Figure 6a shows the schematic of the device developed by Llaguno et al.[83] to study conductance and thermopower oscillation in single carbon NTs in the Coulomb blockade regime. The NT and the electrodes were placed on a thin suspended membrane for large temperature gradient. Boukai et al.[84] developed a fabrication technique that patterned Bi NWs from a polycrystalline Bi films along with the four metal electrodes (Figure 6b). This allowed for accurate four-point I−V measurements without the influence of contact resistance, which had been a challenge for Bi NWs as they tend to form a stable native oxide layer. The device was fabricated on a doped Si substrate that also served as a back gate, thus the Fermi level of the wires could be electrostatically tuned. A suspended version of similar devices was later employed by Boukai et al.[39] to measure power factor and thermal conductivity of single crystalline Si NWs patterned from the Si device layer of a silicon-on-insulator (SOI) wafer.

Figure 6c shows a similar version of the device that has been more commonly used for the majority of the NWs, which were not patterned from a film but rather synthesized from a variety of bottom-up techniques, as discussed in section 2.1. For these devices, NWs were usually transferred to a substrate, and then the heaters and electrodes were fabricated around one or a few specific NWs using e-beam or photolithography and metal patterning. Similar to Figure 6b, the substrate can also be used as a gate electrode to provide the electrostatic gating. These devices have been used to measure and tune power factor in PbSe NWs (Liang et al.[85]), InAs NWs (Tian et al.,[26] Wu et al.[78]), Ge/Si core-shell NWs (Moon et al.,[86] Brovman et al.[87]), Si NWs (Curtin et al.[88]), Bi NWs,[89] Sb_2Te_3 NWs,[90] and wide bandgap semiconductor NWs (Lee et al.[91]). The measurement scheme was also able to extract field effect carrier mobility and the scattering factor.[85,86] An ionic-liquid-based electric double-layer transistor technique has also been employed to induce a wider range of carrier concentration modulation compared with the solid dielectric gate modulation, for example, across the band gap, p-type to n-type switching of thermopower in 1D carbon NT networks.[92]

Lastly, the power factor of certain NWs has also been measured using another version of the suspended microdevice platforms that were developed by Shi and co-workers[31,93,94]

DOI: 10.1021/acs.chemrev.8b00627
Chem. Rev. XXXX, XXX, XXX−XXX

and have been widely used for NW thermal conductivity measurements, as we shall discuss in detail in section 4.1. As shown in Figure 6d, a single NW can be placed onto a prefabricated device consisting of two suspended pads, each of which contains a serpentine heater and two electrodes.[93] The heater is used for heating and thermometry, and the four electrodes are for $I-V$ and thermo-voltage measurements. Along with the thermal conductivity measurement, this platform has be used to directly obtain ZT values of individual NWs and other similar nanostructures, such as Bi_xTe_{1-x} NWs,[31,93] BiTe and Bi_2Te_3 NWs,[95] silicide NWs,[38] SiC NWs,[96] and $(Bi_xSb_{1-x})_2Te_3$ nanoplates.[97,98] The biggest challenge of using this technique lies in the difficulty of obtaining reliable electrical contact to the NWs. Techniques such as e-beam or ion beam induced metal deposition and annealing have often been employed to improve the contacts.[31,38]

3.4. Bi and $Bi_{1-x}Sb_x$ Nanowires

Some of the earlier thermoelectric studies were focused on Bi and $Bi_{1-x}Sb_x$ NWs, as a result of the promises of the quantum confinement effect that is more pronounced in the Bi system due to its small effective mass and long Fermi wavelength: depending of the orientation, Bi has effective mass ranging from $0.0012m_o$ for electron pocket L (here m_o is the bare electron mass) to $0.059m_o$ for T-point hole pocket,[99] whereas the total DOS effective mass of Bi_2Te_3 is $0.69m_o$.[100] Due to this small effective mass, the separation of energy sub-bands can be comparable to k_BT for Bi NWs with a relatively large wire diameter (d_W) of ∼50 nm (see eq 13). Through detailed calculation, Dresselhaus and co-workers[99] investigated the thermoelectric power factor and ZT in cylindrical Bi NWs. The calculated electronic sub-band structure showed that as the NW diameter decreases, the conduction sub-bands move up while the valence sub-bands move down. At 77 K, when the NW diameter reached a critical value of 49 nm for Bi NWs along the $[01\bar{1}2]$ direction, the highest T-point valence sub-band edge crosses the lowest L-point conduction sub-band edge, indicating the onset of the semimetal-to-semiconductor (SMSC) transition, see Figure 7a. Other NW directions showed similar critical diameters ranging from 40 to 55 nm at 77 K. At 300 K, however, the critical diameter for the SMSC transitions reduced to 11−15 nm. Based on these considerations, $ZT > 1.0$ at 77 K was predicted for n-type Bi when the diameter is smaller than 10 nm (see Figure 7b), and high ZT (∼2 at 77 K) was also predicted for p-type 10 nm-diameter Bi NWs if the T-point valence sub-band was removed. The SMSC in Bi NWs was experimentally confirmed[101,102] on the basis of monotonically increasing resistivity at lower temperature (semiconducting behavior) when the NW diameter was below 48 nm, as opposed to the non-monotonic temperature dependence for semimetallic NWs with larger diameters. This SMSC behavior and its effect on the thermopower was also studied in individual polycrystalline Bi NWs.[84]

Dresselhaus and co-workers[80] further computed the electronic structure of $Bi_{1-x}Sb_x$ NWs and found that the extrema of all 10 hole pockets (1 T-point, 3 L-points, 6 H-points) coalesce in energy when $x = 0.13$ and NW diameter is 60 nm. It also revealed an increasingly larger critical diameter for the SMSC when Sb concentration is higher in $Bi_{1-x}Sb_x$. As a result, high thermoelectric power factor and figure of merit were predicted for $Bi_{1-x}Sb_x$ NWs with diameter around 40 nm.[80] Subsequent temperature-dependent resistivity and thermopower measurements by Dresselhaus and co-workers[103,104] indeed showed several pieces of evidence of the SMSC transition, including monotonic temperature dependent resistance, enhanced $|S|$ as a result of Sb doping (e.g., in $Bi_{0.95}Sb_{0.05}$ NWs) and as the NW diameter decreased. In particular, the combined results on both $Bi_{1-x}Sb_x$ NWs[103,104] and Bi NWs[101,102] confirmed the theoretical prediction[80] that the addition of Sb increased the critical diameter for the SMSC transition, as indicated by the semiconducting behavior (monotonic temperature dependence of resistivity) for the 65 nm diameter $Bi_{1-x}Sb_x$ NWs (x = 5 and 10%) and the lack thereof for the Bi NW of the same diameter (see Figure 7c).

In addition, Masayuki et al.[105] studied thermoelectric properties of Bi micro- and NWs fabricated by high-pressure injection of molten Bi into quartz templates. For the smallest wire measured (d = 850 nm), they observed bulk-like σ (7.63×10^5 S/cm) and S (−57 μV/K). They further analyzed the temperature dependence of the resistivity and attributed it to the reduced mobility (1−2 $cm^2/V{\cdot}s$ at room temperature) relative to that of a bulk single crystal. Nikolaeva et al.[106] observed the diameter- and temperature-dependent thermopower, including sign changes, of Bi NWs 150−480 nm in diameter (Figure 7d), and they attributed the variations in the thermopower to the classical size effect, namely, stronger mobility limitation posed by hole-boundary scattering with respect to electron-boundary scattering.[106]

Lee and co-workers used an on-film formation of nanowires (OFF-ON) method to grow single-crystal Bi NWs.[109] The method was based on the spontaneous growth of metal NWs from metal thin films, driven by the thermal stress due to thermal expansion mismatch between the deposited Bi thin films and the substrate (e.g., SiO_2/Si), a process that has been observed in whiskers formation in solders and other low-melting point metals.[110] Because of the single crystal nature, the grown NWs exhibited an extraordinarily high electron mobility (76 900 $cm^2/V{\cdot}s$) and a long MFP of 1.35 μm,[109] see Figure 7e. The high-quality single-crystal nature of the Bi NWs grown from the OFF-ON method was further evidenced from the observed high magnetoresistance,[111] Shubnikov−de Hass (SdH) oscillations,[112] weak anti-localization and conductance fluctuation,[113] and anisotropic thermoelectric power factor for NWs grown along different crystal orientations.[114] The same group further demonstrated quantum size effect of SdH oscillations observed in a 100 nm-diameter Bi NW, which led to sub-band energy shifts and enhanced electron and hole effective masses due to the electron−hole coupling.[115] They further carried out a systematic study on the size effect of S and σ.[89] Within the diameter range of 178 and 40 nm, they found $|S|$ gradually reduced from the bulk value for larger-diameter NWs (e.g., $S = -60$ μV/K when d = 178 nm) to a very small value ($S = -20$ μV/K for d = 40 nm) while the resistivity increased significantly from the bulk value ($\sim 2 \times 10^{-4}$ $\Omega{\cdot}$cm) with reducing diameter. This behavior was attributed to the decreasing overlap between these two sub-bands (for decreasing σ) and the cancellation effect of the T-point holes and L-point electrons on the thermopower (Figure 7f). However, when the diameter decreased further below 40 nm, both σ and $|S|$ gradually increased with reducing diameter, which was attributed to the effect of the surface states (Figure 7f). As a result, they obtained the highest power factor of 55 $\mu W/cm\text{-}K^2$, which is, notably, higher than that of $Bi_{0.5}Sb_{1.5}Te_3$.

DOI: 10.1021/acs.chemrev.8b00627
Chem. Rev. XXXX, XXX, XXX−XXX

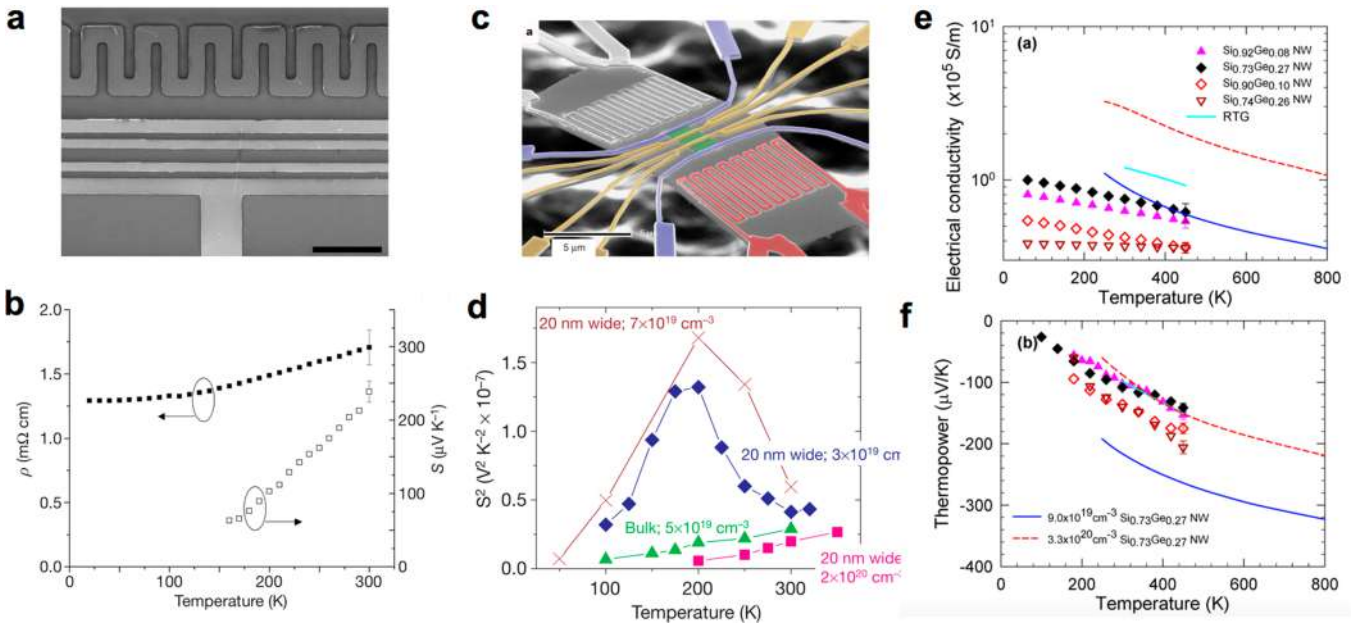

Figure 8. Thermoelectric power factor of Group IV (Si, $Si_{1-x}Ge_x$) nanowires. (a) Electron micrograph of a microfabricated device for power factor measurement (the scale bar is 10 μm) and (b) measured S and ρ of individual electrolessly etched Si nanowires. Reprinted with permission from ref 33. Copyright 2008 Nature Publishing Group. (c) Electron micrograph of a suspended microfabricated device for power factor measurement of lithographically patterned Si nanowire arrays with 10−20 nm width and thickness, made from the SNAP method. (d) Measured S of the nanowire array. Reprinted with permission from ref 39. Copyright 2008 Nature Publishing Group. (e) Measured electrical conductivity and (f) thermopower of individual $Si_{1-x}Ge_x$ nanowires with various Ge contents and doping concentrations. Reprinted with permission from ref 43. Copyright 2012 American Chemical Society.

3.5. Group IV Nanowires

Group IV materials, including Si, Ge, and SiGe alloys, are the most widely studied semiconductors for microelectronics. They have attractive electronic properties for thermoelectrics, such as high mobility, and their doping and contacts (i.e., metallization) have been widely studied and well-established. As such, Group IV NWs were among the first NWs grown and reported.[116−119] In fact, Si NWs as small as 1.3 nm diameter have been prepared with their surface morphology and electronic energy band structure studied via scanning tunneling microscopy (STM).[120]

In the bulk form, SiGe alloy is a well-known and one of the most widely used thermoelectric material at high temperature, for instance, in the radioisotope thermoelectric generators (RTGs) for NASA's spacecraft.[121] On the other hand, Si has been known as a poor thermoelectric materials due to its high lattice thermal conductivity (over 100 W/m-K for bulk Si). The attention to Si NWs for thermoelectricity had not been significant until it was recognized that the lattice thermal conductivity can be drastically reduced in Si thin films and NWs, as we shall discuss in section 4. As a result, there have been tremendous efforts to enhance the thermoelectric power factor of Group IV NWs in general and Si NWs in particular.

Some of the earlier power factor studies on Si NWs focused on the wires fabricated from different techniques. For instance, Hochbaum et al.[33] fabricated Si NWs by electrolessly etching bulk Si wafers with suitable dopant concentration. The process resulted in NWs with rather rough surfaces, which was then post-doped with boron to reach a suitable carrier concentration. They used microfabricated device to measure S and ρ of individual rough Si NWs[33] (Figure 8a,b). The measured resistivity ranged in 3 ± 1.4 mΩ·cm at room temperature, and monotonically decreased at lower temperature, consistent with the metallic behavior of degenerately doped Si (~10^{19} cm^{-3} dopant concentration).[33] The measured S also decreased with decreasing temperature (Figure 8b), also indicating the metallic behavior (i.e., S mostly contributed by the diffusion of electrons).[33] Boukai et al.[39] measured thermopower and conductivity of arrays of individual NWs with cross-sectional areas of 10 nm × 20 nm and 20 nm × 20 nm made from the SNAP method (Figure 8c). Interestingly, they observed significantly increased thermopower in these small-sized NWs compared to that of bulk Si with similar doping concentration (mid to high 10^{19} cm^{-3}), see Figure 8d. This giant thermopower was attributed to the phonon drag effect,[39] which is originated from the non-equilibrium energy transfer from thermally driven phonons flowing to charger carriers.

While the phonon drag effect is commonly known to be diminished in reduced specimen size due to the phonon-boundary scattering,[122] it was postulated that there is a 3D-to-1D transition in phonon modes when the phonon wavelength is larger than or on the same order of the NW width.[39] 1D modes already incorporated the boundaries and their MFPs are not affected by the boundaries.[39] Sadhu et al. measured the thermopower of vertical arrays of electrolessly etched Si NWs and found that the phonon drag effect was quenched in these NWs due to the phonon boundary scattering.[123] The different roles of the phonon drag effect on the thermopower revealed by Boukai et al.[39] and Sadhu et al.[123] could be due to the different sizes and surface morphologies in the NWs, namely, ~100 nm diameter rough NWs and 3D phonon spectrum in Sadhu et al.[123] and 10−20 nm diameter smoother NWs and possibly 1D phonon modes in Boukai et al.[39] More studies are needed to further elucidate the role of phonon drag in Si and other Group IV NWs.

DOI: 10.1021/acs.chemrev.8b00627
Chem. Rev. XXXX, XXX, XXX−XXX

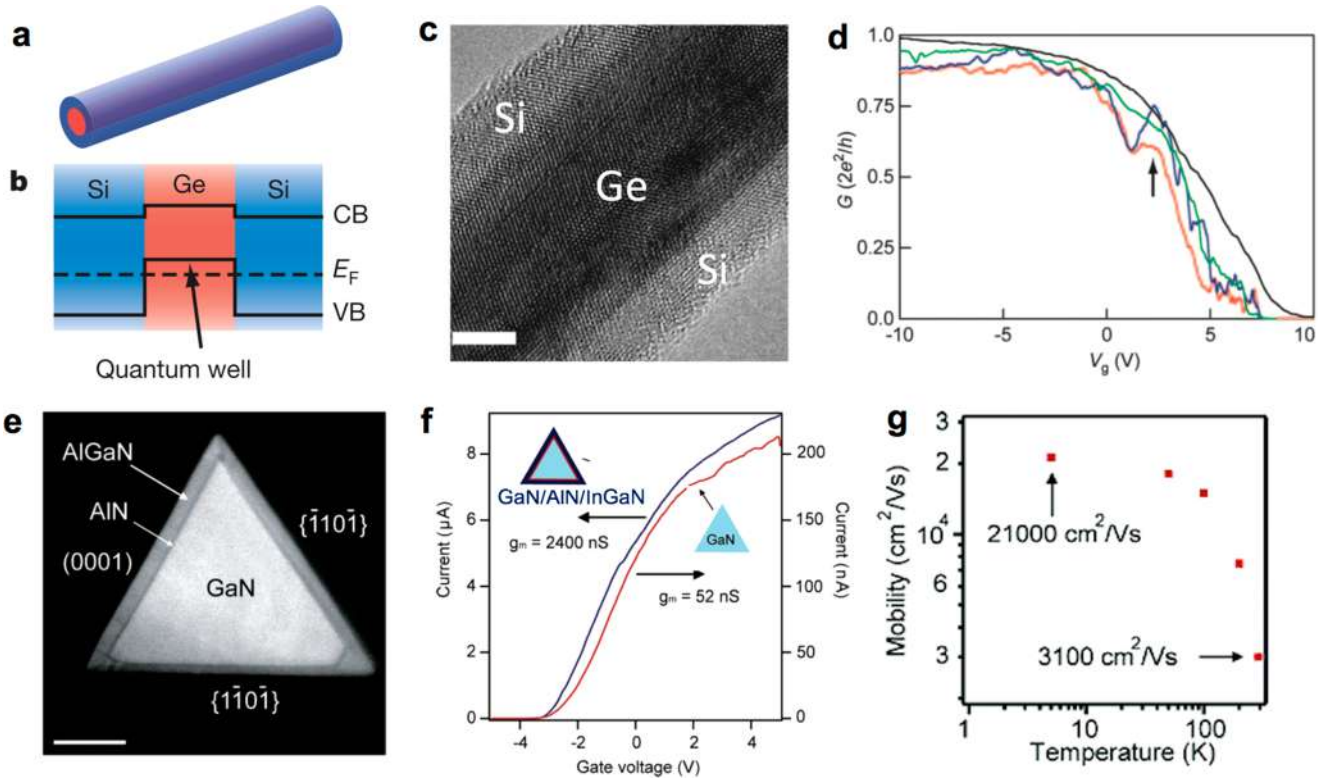

Figure 9. High mobility in radial core−shell heterostructured nanowires. (a) Schematic of a Ge−Si core−shell nanowire, where the red represents the Ge core and blue represents the Si shell. (b) Cross-section energy diagram in the Ge−Si core−shell nanowire showing the formation of the Ge quantum well with quasi-1D hole gas, injected from the Si shell due to the Fermi level pinning effect.[18] CB and VB represent the conduction band and valence band, respectively. Reprinted with permission from ref 144. Copyright 2006 Nature Publishing Group. (c) High-resolution TEM image of a Ge−Si core−shell nanowire with ∼15 nm Ge core diameter and ∼5 nm Si shell thickness. The scale bar is 5 nm. (d) Conductance G (normalized by the quantum of conductance, $\frac{2e^2}{h}$) vs gate voltage V_g, showing the quantized and ballistic conductance at various temperatures (represented by different colors of the curves; black, green, blue, and red correspond to 300, 50, 10, and 4.7 K, respectively). Reprinted with permission from ref 18. Copyright 2005 National Academy of Sciences, USA. (e) Cross-sectional TEM image of GaN-AlN-AlGaN radial nanowire heterostructures. The scale bar is 50 nm. (f) Current vs gate voltage curves for a GaN nanowire (red curve, right axis) and a GaN/AlN/InGaN core−shell nanowire (blue curve, left axis), showing the giant enhancement in the conductance with the heterostructures. (g) Mobility of the GaN-AlN-AlGaN core−shell nanowires as a function of temperature; very high mobilities were realized at room and low temperature. (e−g) Reprinted with permission from ref 147. Copyright 2006 American Chemical Society.

SiGe alloy NWs also draw a lot of interest due to the anticipated reduction in lattice thermal conductivity caused by boundary scattering on low-frequency phonons, which are the main contributors to lattice thermal conductivity in bulk SiGe due to the alloy scattering.[124] Amato et al. recently reviewed the progress in SiGe NWs, including their thermoelectric properties.[125] From the experimental work, power factor of SiGe alloy NWs was found to be lower compared to the corresponding bulk values[43,126] due to the scattering of carriers by the surface states. For instances, systematic measurements on a series of Si_xGe_{1-x} NWs by Lee et al.[43] showed appreciable reduction in electrical conductivity (Figure 8e) but comparable Seebeck coefficient compared to bulk SiGe (Figure 8f). The reduced electrical conductivity is caused by surface scattering of the charge carriers.[43] However, despite this reduction in the electrical conductivity and power factor, the ZT is still much larger ($ZT \approx 0.46$ at 300 K) compared to those of SiGe bulks due to the reduction in lattice thermal conductivity, and was theoretically projected to be even higher (over 2) at 800 K.[43] Interestingly, the reduction of electrical conductivity is perhaps a practical issue due to the surface scattering, rather than an intrinsic one caused by the alloy scattering. Atomic-scale calculations by Amato et al.[127] on electrical conductance of SiGe alloy NWs in the ballistic regime showed that the electrical transport is rather insensitive to Ge doping, and hence the alloying approach can be utilized to reduce the thermal conductivity and enhance the ZT.

These studies on thermopower and conductivity of Group IV NWs revealed a significant effect dictating the power factor, which is the scattering of charge carriers by NW surfaces and the consequent reduction of mobility and conductivity. This issue is certainly not unique in thermoelectrics and has been extensively investigated in the earlier days of NW research for a variety of applications, such as microelectronics and photovoltaics, for which the device performance is also hinged on mobility and carrier lifetime.[128−130] Work on NW transistors have suggested promising pathways to mitigate the surface effects for enhanced mobility, such as surface passivation by SiO_2,[131] amorphous Si,[132] carbon coating,[133] and diamond coating,[134] etc. On the other hand, the small diameters of NWs may also be utilized to boost the mobility. For instance, calculations have shown that for small-diameter Si NWs, the phonon-limited mobility can actually be enhanced over that of bulk values, for instance, hole mobility in ∼3.5 nm diameter Si NWs, due to the modified electron and phonon spectra.[135,136] In addition, strain engineering has been suggested to increase

DOI: 10.1021/acs.chemrev.8b00627
Chem. Rev. XXXX, XXX, XXX−XXX

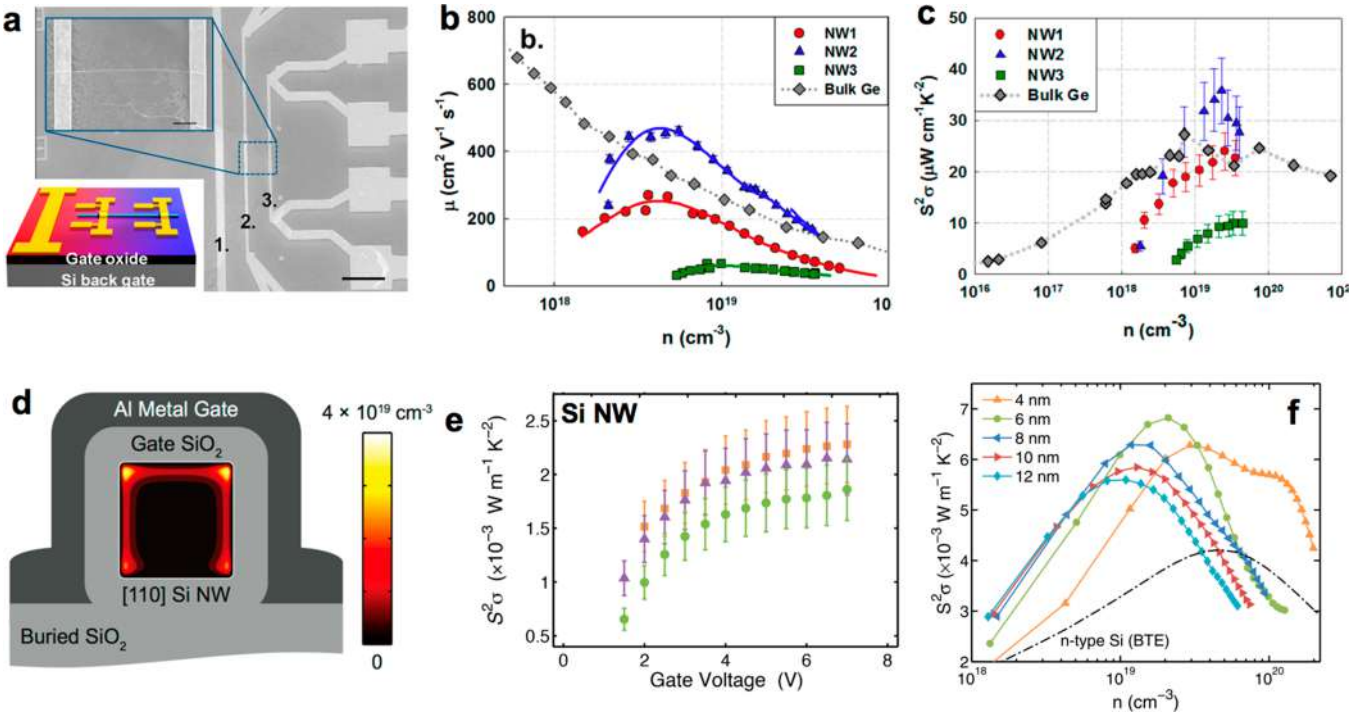

Figure 10. Thermoelectric power factor of nanowires with modulation doping, induced via field effect and/or core−shell modulation. (a) SEM image of a microfabricated device utilized for the field effect thermopower and electrical conductivity measurements. Electrode 1 is for heating and electrodes 2 and 3 are used for $I-V$ as well as voltage and temperature measurements. The scale bar is 10 μm. The top inset shows a close-up image of a nanowire (NW) between electrodes 2 and 3 (scale bar 1 μm), and the bottom inset is a schematic of the device with Si back gate. (b) Mobility μ vs carrier concentration n of the Ge−Si NWs extracted from field effect measurements shown in (a). The Ge-core diameters are 24.0, 15.1, and 11.4 for NW 1, 2, and 3, respectively. The gray diamonds show the μ of bulk Ge. (c) Measured power factor ($S^2\sigma$) of the measured Ge−Si core−shell NWs. (a−c) Reprinted with permission from ref 86. Copyright 2013 American Chemical Society. (d) Schematic of a Si NW wrapped around by Al metal gates. The color scale represents the carrier concentration induced by the field effect modulation. (e) Measured power factor ($S^2\sigma$) vs gate voltage of three gated Si NWs. (d, e) Reprinted with permission from ref 88. Copyright 2013 American Chemical Society. (f) Computed power factor of gate-all-around Si NWs with varying cross-section area. Reprint with permission from ref 158. Copyright 2014 American Institute of Physics.

the mobility in Si NWs.[137,138] These ideas are attractive for enhancing the power factor and are therefore worth investigating for thermoelectric applications.

3.6. Radial Core−Shell Heterostructured Nanowires with Modulation Doping

As shown earlier, the NW surface can be a foe for thermoelectric transport due to the carrier surface scattering that typically reduces the carrier mobility and ultimately the thermoelectric power factor. However, when properly engineered, the extensive surface area of NWs can also become beneficial for the power factor. In addition to the aforementioned surface passivation and coating approaches, a more exciting opportunity offered by semiconductor NWs is the radial heterostructures, such as core−shell or core−multi-shell structures, which are more controllable and hence have been systematically studied in the literature. While most of these studies were primarily intended for applications in electronics and optoelectronics, they nevertheless provide important insights into the strategies to reduce the carrier scattering and enhance the mobility, which are relevant to thermoelectric transport. In nominally undoped core−shell heterostructured NWs, electron and hole gases can be introduced. These free carriers are created due to the Fermi level pinning effect. In the case of Si-core and Ge-shell NWs, the alignment of the Fermi levels between Ge and Si results in large concentration of free holes accumulated in the Ge core (Figure 9a,b), as indicated by the lower valence band below the Fermi energy, akin to the generation of electron or hole gases in 2D QWs, but now in the quasi-1D geometry. This hole accumulation has been directly observed from electron holography[139] and Raman scattering,[140,141] and has been theoretically studied using first-principles calculations by Amato et al.[142] Core−shell Group IV NWs with sharp Ge−Si interfaces (Figure 9c) have been grown by the common VLS approach, where the intrinsic Si (i-Si) shells were deposited on i-Ge core NWs through the decomposition of Si-containing precursor gases (e.g., SiH_4).[18,143,144] This dopant-free strategy to create free carriers can result in very high carrier mobility in the NWs, due to the absence or mitigation of the ionized impurity scattering, which often is a strong scattering mechanism for charge carriers. The high mobility has been exploited for a number of electronic applications, such as high-performance NW transistors with high mobility (~730 $cm^2/V\cdot s$) or transconductance, high on-current, and short intrinsic delay time.[144] Conductance quantization of the 1D hole gas was also observed in short and thin (L = 160 nm and Ge core diameter ~10 nm) Ge−Si core−shell NWs from low temperature (~4 K) to room temperature (Figure 9d).[18] The ballistic transport can be attributed to long carrier MFP even at room temperature (estimated to be ~500 nm), due to the reduction of ionized impurity and the suppression of acoustic phonon scattering due to the quasi-1D DOS.[18] A comprehensive study by Nguyen et al.[145] showed that the

DOI: 10.1021/acs.chemrev.8b00627
Chem. Rev. XXXX, XXX, XXX−XXX

mobility in Ge−Si core−shell NWs (~200 $cm^2/V·s$) is largely independent of the diameter for NWs with diameters ranging from 15 to 50 nm and a Si shell of 3 nm, whereas the NWs without the Si shell exhibited much lower mobility. Recent measurements by Conesa-Boj et al.[146] showed a high mobility of 1600 $cm^2/V·s$ at room temperature for high hole densities of 10^{19} cm^{-3} in coherently strained Ge−Si core−shell NWs. These observations further confirmed the notion that the modulation doping mechanism induced by the core−shell structure can overcome the surface-induced mobility degradation often seen in single-component NWs.[145]

This co-axial core−shell growth mechanism is quite generic,[125] as has also been shown in Si(core)/Ge (shell), Si/Ge/Si, and p-Si/i-Ge/p-Ge,[143] i-Ge/p-Ge/i-Si,[148] Ge−Si_xGe_{1-x}.[149] Also, the core−shell doping strategy is not limited to the Group IV system. Core−shell (or multi-shell) NWs made of III-V semiconductors and other materials have also been synthesized and shown high performance, including high mobility, as recently reviewed by Royo et al.[150] For instance, Figure 9e shows dopant-free GaN core−AlN-InGaN shell triangular NWs.[147] Compared to intrinsic GaN NWs, the dopant-free GaN/AlN/InGaN core−shell NWs showed 50-fold enhancement in conductance (Figure 9f), and substantially higher mobility, measured to be ~3100 and ~21 000 $cm^2/V·s$ at room temperature and 5 K, respectively, using a field-effect transistor configuration.[147] High mobility has also been observed in a wide range of III-As core−shell or multi-shell NWs.[151−156] The enhanced mobility in core−shell NWs indicates that thermoelectric power factor can in principle be enhanced over that of bulk values. The mechanism of using the spatially confined electron or hole gas in Ge−Si core−shell NWs has been systematically studied by Markussen et al. using atomistic calculations.[157] Enhanced conductance of the hole gas in the Ge core was suggested even with the presence of NW surface disorder, which, along with the reduced thermal conductivity, could lead to a *ZT* as high as 2 in Ge−Si core−shell NWs. Interestingly, the principle has been indeed realized in recent thermoelectric measurements, as discussed in section 3.7.

3.7. Thermoelectric Power Factor of Modulation-Doped Nanowires

The modulation doping introduced by the radial core−shell heterostructures as well as the field effect modulation has been utilized to investigate and enhance the power factor, with the primary mechanism being the suppressed ionized impurity scattering commonly encountered in chemically doped semiconductors. This modulation doping technique has been shown to be effective for enhancing the power factor in nanocomposites,[30,64] and has gained significant interests in NWs due to the capability of producing high-quality core−shell NWs as detailed in the previous section.

Using a measurement configuration similar to that of Liang et al.,[85] Moon et al.[86] reported field effect modulated thermoelectric power factor of individual Ge−Si core−shell NWs, as shown in Figure 10a−c. Figure 10a shows an SEM image of a microfabricated device utilized for the field effect thermopower and conductivity measurements. By varying the gate voltage applied to the Si substrate, the carrier concentration in the NW can be modulated. This leads to the measurements of the carrier mobility as a function of the carrier concentration (Figure 10b). In certain NWs (e.g., the one with a diameter of 15.1 nm), the extracted mobility could actually be ~30% higher than that of bulk Ge. As a result, the peak power factor in this NW was also higher than that of bulk Ge (Figure 10c). This result highlights the promise of using epitaxial core−shell heterostructures to enhance the mobility and power factor in semiconductor NWs. The study also pointed to several factors for further improvement. For instance, detailed analysis of the data showed that the mobility is still below that of the phonon scattering limit, indicating the presence of chemical defects in the Ge core channel (e.g., inter-diffusion between Si and Ge).

Curtin et al.[88] also reported the use of electrostatic gate modulation to tune the carrier concentration and thermoelectric power factor in Si NWs fabricated from SOI device layers. The metal gates, which wrapped around the Si NWs, can induce high-mobility charges through the field effect, see Figure 10d. The mobility in the gated Si NWs is around 170−200 $cm^2/V·s$, substantially higher than that of As-doped n-type Si thin films (~76 $cm^2/V·s$). As a result, the observed optimal power factor in the gated NWs of 35−40 nm^2 in cross sections is similar to the peak values in n-type Si thin films, despite electron transport occurring only at the NW surface (Figure 10e).

While the experimental work has yet to demonstrate a giant increase in the power factor by the electrostatic gating effect, theoretical and computational work has pointed to the large potential of this approach. Curtin and Bowers[158] further used BTE to model the power factor of gate-all-around Si NWs with smaller cross sections (4×4 nm^2 to 12×12 nm^2), and found substantially higher electrical conductivity in the gated NWs than that of doped Si due to the absence of ionized impurities and consequently higher mobility. They theoretically obtained a maximum power factor of 68 $\mu W/cm·K^2$ for Si NWs with 6×6 nm^2 in cross section, which is about 60% higher than the best power factor of Bi−Sb−Te alloys (Figure 10f). In a series of papers,[159,160] Neophytou and coauthors computed the gating effect on the thermoelectric power factor and *ZT* of Si NWs in different crystallographic orientations using atomistic tight-binding simulations for electronic structure calculations, coupled with BTE for transport calculations. They also showed that the mobility in the gated NWs is largely phonon limited (with a small contribution from surface roughness scattering), and can be enhanced over that of the chemically doped NWs.[160] As a result, the power factor of the gated Si NWs can be enhanced by up to 5-fold over that of the doped ones.[160] Despite the corresponding increase in electronic thermal conductivity, the *ZT* was calculated to increase by 3-fold, up to 0.4 at 300 K and 1.2 at 750 K.[159]

3.8. Modulation Doping Due to Dopant Inhomogeneity

The modulation doping mechanism reveals an interesting prospect to enhance the thermoelectric power factor in NWs if the dopant distribution is inhomogeneous, which can be introduced during the NW growth and/or doping process either unintentionally or intentionally.[161−164] In this regard, it is important to quantify the exact dopant and carrier distribution in the NWs, a subject recently reviewed by Ek and Filler.[165] Perea et al.[163] measured the axial and radial distribution of dopant in P-doped Ge NWs using atomically resolved 3D reconstructed images from atom probe tomography, and revealed that the dopant distributions are highly inhomogeneous due to the diffusion nature of dopant incorporation, through both the catalyst regions (pathway "*i*" in Figure 11a) and the uncatalyzed surface decomposition of

DOI: 10.1021/acs.chemrev.8b00627
Chem. Rev. XXXX, XXX, XXX−XXX

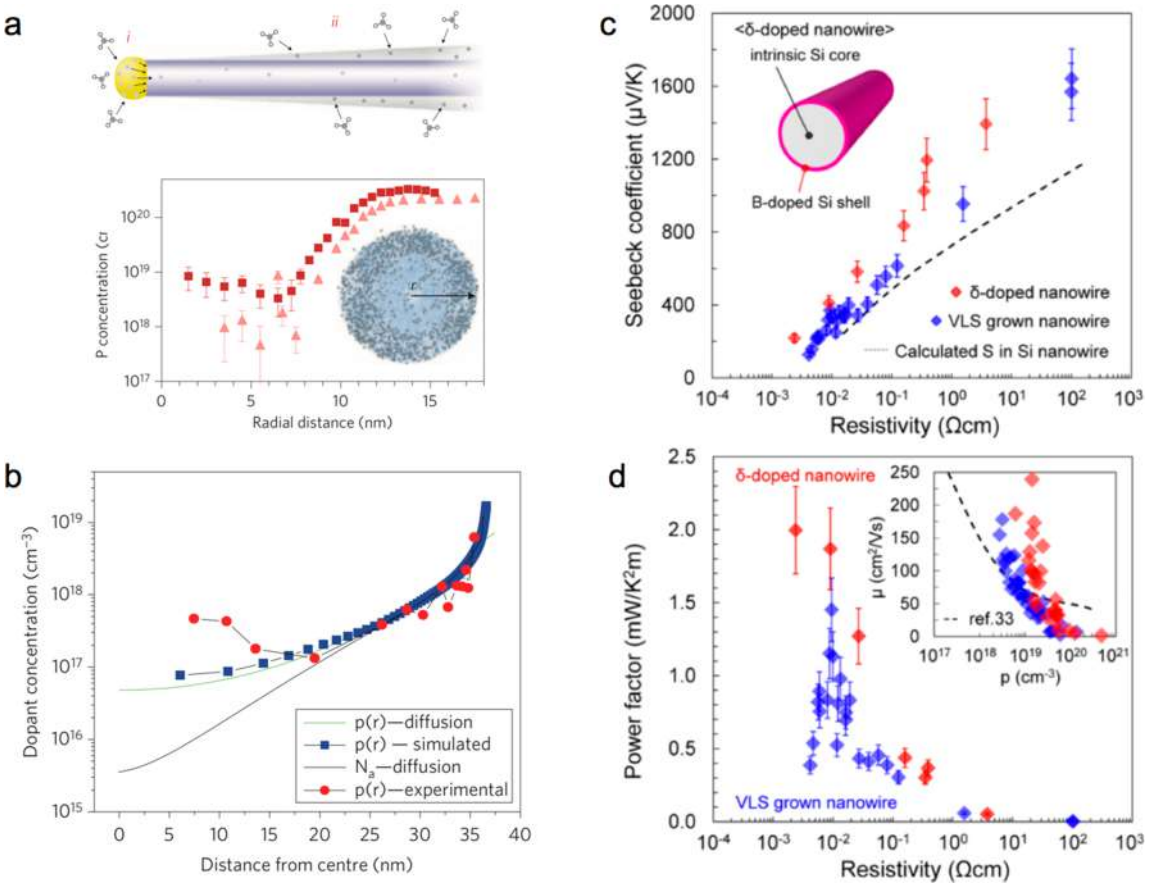

Figure 11. Doping inhomogeneity in nanowires and its impact on thermoelectric power factor. (a) Dopant diffusion pathways (top) and radial distribution of dopant (P) concentration revealed from atomically resolved 3D reconstruction of atom probe tomography in Ge NWs (bottom). Pathway "*i*" represents the introduction of dopants via the catalyst (most commonly Au in most VLS growth of Si and Ge NWs), and pathway "*ii*" represents the incorporation of dopants through uncatalyzed surface decomposition. Triangles and squares in the bottom figure represents PH_3:GeH_4 ratios of 1:1000 and 1:500, respectively. Reprinted with permission from ref 163. Copyright 2009 Nature Publishing Group. (b) Radial dopant profile in B-doped Si NWs extracted from experimental C−V curves. The red symbols are experimentally extracted B profiles. Reprinted with permission from ref 166. Copyright 2009 Nature Publishing Group. (c) Seebeck coefficient and (d) Power factor vs resistivity of Si NWs with different doping profiles. Red diamonds: *δ*-doped NW with a shallow B-doped Si shell and an intrinsic Si core, as schematically shown in the inset in (c). Blue diamonds: VLS grown NWs with presumably uniform doping profile. Dashed line: Calculated *S* in Si NWs based on the Mott relation. Reprinted with permission from ref 167. Copyright 2014 American Chemical Society.

the doping specifies, e.g., PH_3 (pathway "*ii*" in Figure 11a). It was further shown that the core and the shell regimes are substantially under-doped and over-doped, respectively, relative to the stoichiometric dopant concentration for given PH_3:GeH_4 flow ratios of 1:500 and 1:1000. The difference in the dopant concentrations between the core and the shell regimes can be greater than 1 order of magnitude, see Figure 11a. Detailed *C*−*V* measurements done by Garnett et al.[166] on VLS grown B-doped Si NWs also showed similarly large variations in the dopant concentrations as well as the carrier concentrations along the radial direction (Figure 11b).

By exploiting the inherent dopant inhomogeneity in NWs, Zhuge et al.[167] further advanced the modulation doping idea in VLS-grown Si NWs. After the NWs were synthesized, the NWs were post-doped by introducing dopant containing precursor gases at a suitable temperature. For instance, B dopants were introduced with B_2H_6 at 750 °C,[167] which resulted in a naturally inhomogeneous dopant profile along the radial directions. Interestingly, a *δ*-doping profile can be realized by creating a heavily B-doped thin shell on an otherwise nominally intrinsic core through a very brief exposure to B_2H_6, see the inset in Figure 11c. Measurements of thermopower, resistivity, and mobility (through field-effect measurements) revealed that the thermopower was higher in the *δ*-doped Si NWs compared to the uniformly doped ones with similar resistivities (Figure 11c). This enhancement was also attributed to the higher mobility in the *δ*-doped NWs (inset in Figure 11d): as the mobility was higher, the carrier concentration to achieve the same conductivity was lower, thus resulting in a higher thermopower. This effect led to an enhanced power factor in the *δ*-doped NWs (Figure 11d). While the resultant power factor is not higher than that of optimally doped bulk Si or Bi−Sb−Te alloys, the underlying synthetic and physical principles revealed in this study highlight the potential of manipulating the chemistry of NW synthesis to gain thermoelectric performance.

3.9. Thermoelectric Effect of Surface States in Topological Insulator Nanowires

During the past decade, surface states of topological insulators (TIs) have attracted significant interest from the condensed matter community. A TI is a material that is insulating in the bulk form; that is, it has a finite bandgap but has conducting surface states due to the non-trivial symmetry-protected

DOI: 10.1021/acs.chemrev.8b00627
Chem. Rev. XXXX, XXX, XXX−XXX

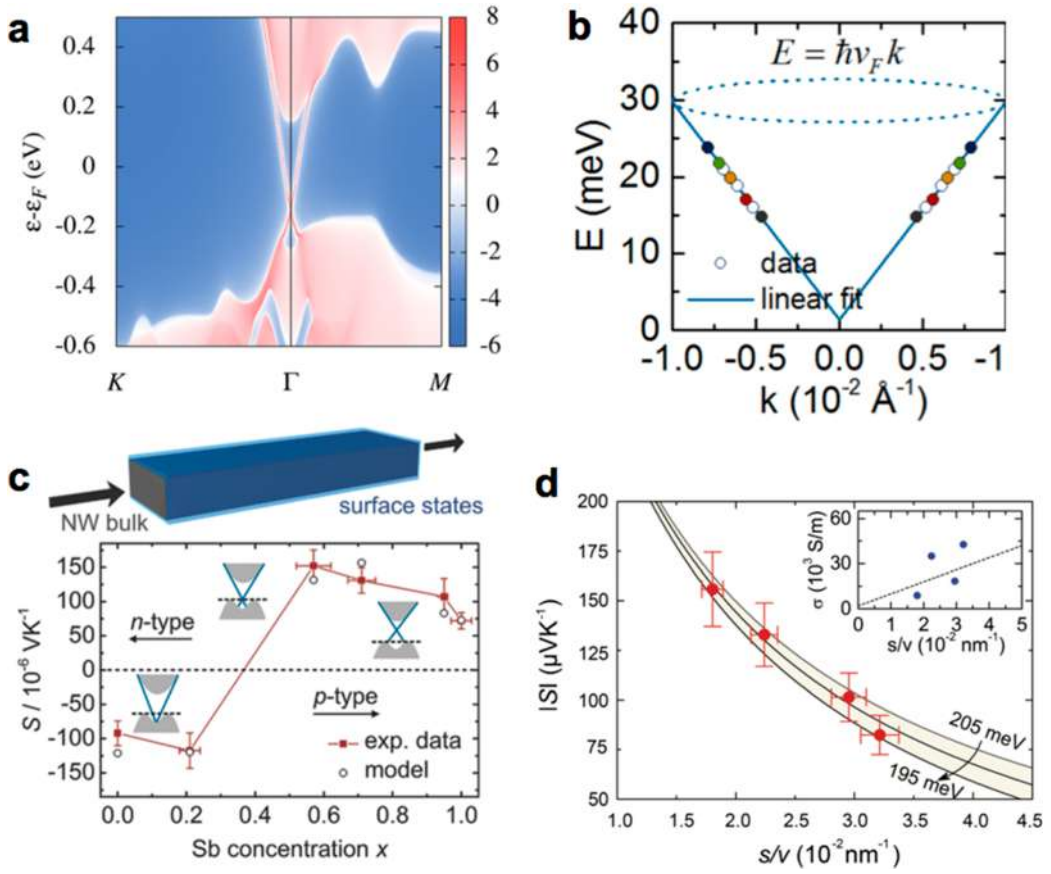

Figure 12. Thermoelectric power factor of topological insulator nanowires. (a) Surface spectral function of (111) surface of Bi_2Se_3, indicating the presence of the Dirac cone. Reprinted with permission from ref 168. Copyright 2018 Wiley-VCH. (b) Band structure of the top surface of a Bi_2Te_3 NW showing the Dirac cone. The data were obtained from the field effect measurement. Reprinted with permission from ref 170. Copyright 2014 American Institute of Physics. (c) Thermopower of $(Bi_{1-x}Sb_x)_2Te_3$ NWs as a function of Sb concentration x. Reprinted with permission from ref 185. Copyright 2015 Wiley-VCH. (d) Thermopower and conductivity (shown in inset) as a function of surface-to-volume ratio in Bi_2Se_3 NWs. Reprinted with permission from ref 186. Copyright 2016 Royal Society of Chemistry.

topological order. These surface states form a gapless Dirac cone (Figure 12a), or a linear dispersion relation, and the time-reversal symmetry ensures that Dirac fermions cannot be scattered by non-magnetic impurities or crystal defects.[168] TI was first experimentally shown in HgTe QW.[169] Interesting, many of the subsequently discovered TI materials are well-known thermoelectric materials due to the strong spin−orbit coupling, such as Bi_2Te_3,[170−174] Sb_2Te_3,[174] Bi_xSb_{1-x},[175,176] and $(Bi_{1-x}Sb_x)_2Te_3$.[177] While the contribution of the surface states to the thermoelectric transport is expected to be negligible compared to the bulk states in bulk materials, nanostructures with a high surface-area-to-volume ratio can signify the surface effect and thus offer a unique opportunity to study the thermoelectric effect of the TI surface states.[168,178,179] Indeed, Gooth et al.[170] revealed the Dirac cone of the surface states in Bi_2Te_3 TI NWs using field-effect measurements (Figure 12b), which are featured with extremely high mobility (38 000−45 000 cm^2/V·s at 2 K).[170]

Because of these intriguing properties, especially the high mobility, there are increasing number of studies on thermoelectric properties of TI NWs. Gooth et al.[180] theoretically analyzed thermoelectric transport in TI NWs with the consideration of contributions from both the metallic surface state and bulk states. They concluded that the ZT of the TI NWs will eventually converge to that of the surface states, regardless of the properties of the bulk states. However, the ZT is not necessarily enhanced relative to the best bulk values (i.e., $ZT \approx 1$). Other calculations also showed hybridization of the top and bottom surface states, which induced a tunable bandgap that could increase the figure of merit well exceeding the unity, especially at low temperature.[181−183] The maximum ZT occurred when the chemical potential lay in the bandgap of the hybridized surface states,[183] a situation highly resembling the idea of achieving high ZT by narrow bandgap induced by SMSC in Bi and $Bi_{1-x}Sb_x$ NWs, originally studied by Dresselhaus and co-workers nearly 20 years ago!

Thermoelectric characterizations in bismuth chalcogenide NWs could be dated back to the 2000s, but have become more active due to the discovery of the TI surface states in these materials. Some of the earlier measurements include Bi_2Te_3 NWs and nanoplates by Shi and co-workers[31,93,97,98] and by Nielsch and co-workers.[184] Studies by Pettes et al. on ∼9 nm thick nanoplates[97,98] did not reveal the contribution of the TI surface states to the power factor, which was attributed to the excess extrinsic chemical doping that overwhelmed the surface states. Hamdou et al.[185] systematically varied the composition of $(Bi_{1-x}Sb_x)_2Te_3$ NWs grown by the VLS method and showed that the dependence of the thermopower on x followed the expectation of surface-state dominant transport (Figure 12c). A further study by Shin et al.[186] showed that the surface-to-volume ratio (S/V) is the key parameter determining the thermopower transport in TI Bi_2Se_3 NWs. As S/V increased in

DOI: 10.1021/acs.chemrev.8b00627
Chem. Rev. XXXX, XXX, XXX−XXX

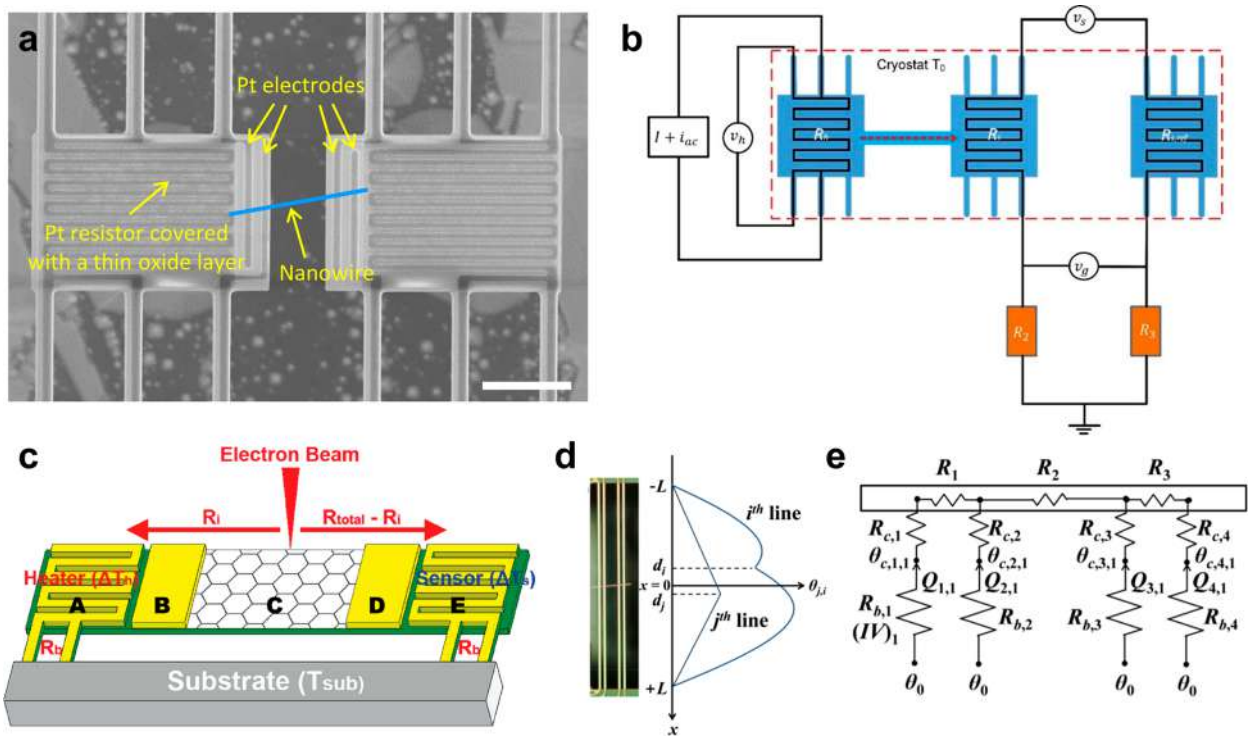

Figure 13. (a) SEM micrograph of the suspended microdevice with electrodes and integrated microheaters/thermometers made from serpentine Pt lines. The scale bar is 10 μm. (b) Simplified electrical measurement circuit (the Wheatstone bridge circuit).[194] (c) Schematic of the localized electron beam heating technique. The connecting beams were only drawn on one side. R_b, R_{total}, and R_i denote the thermal resistances of the connecting beams, from heater to sensor, and from heater to electron beam spot, respectively.[193] Reprinted with permission from ref 193. Copyright 2011 American Chemical Society. (d) Optical image of a 740 nm wide, 220 nm thick patterned Si NW sample assembled across four suspended Pt/SiN$_x$ lines together with a schematic of the temperature profiles along the Pt/SiN$_x$ heater line (ith line) and one Pt/SiN$_x$ resistance thermometer line (jth line, $j \neq i$).[195] (e) Thermal resistance circuit of the measurement device when the first Pt/SiN$_x$ line is electrically heated. R_1, R_2, and R_3 are the thermal resistances of the left, middle, and right suspended segments of the suspended Si NW sample, respectively. $R_{c,j}$ is the contact thermal resistance between the jth Pt/SiN$_x$ line and the sample. $R_{b,j}$ is the thermal resistance of the jth Pt/SiN$_x$ resistance thermometer line. $\theta_{c,j,i}$ is the jth Pt/SiN$_x$ line temperature at the contact to the sample when the ith line is used as the heater line. The temperature rise θ_0 at the two ends of each of the suspended Pt/SiN$_x$ lines is assumed to be negligible.[195] (d, e) Reprinted with permission from ref 195. Copyright 2015 American Physical Society.

smaller NWs, the thermopower decreased while the electrical conductivity increased (Figure 12d). They attributed this behavior to the more dominant metallic (gapless) surface states, as S/V increased, which is consistent with the model by Gooth et al.[180] Further experimental studies to show enhancement of power factor due to gapped surface states in TI NWs would be exciting, but they would also require exquisite control on the doping and geometry of the NWs.

3.10. Summary

The resurgence of thermoelectric research in the past two and a half decades has been largely inspired by the predictions made by Dresselhaus and co-workers on high thermoelectric power factors due to the quantum confinement effect in quantum wells and NWs, and to their earlier work on Bi and BiSb alloy NWs in the search for narrow bandgaps induced by the semimetal-to-semiconductor transition and carrier pocket engineering. While a large thermoelectric figure of merit has not been observed due to the exact same effects in these NWs, these concepts nevertheless have led to breakthroughs toward the understanding and enhancement of power factors in other materials and structures. In the meantime, new concepts have been introduced to boost the power factor in semiconductor NWs, such as the modulation doping in core−shell heterostructures and inhomogeneous doping, as well as hybridized gapped surface states in topological insulator NWs. While these concepts have been demonstrated in recent experiments, the realization of the full potential of these ideas still awaits further investigation, which, fortunately, is expected to benefit from the increasingly sophisticated and precise control of NW synthesis at atomic level.

4. THERMAL TRANSPORT PROPERTIES OF NANOWIRES

In pursuing thermoelectric applications of NWs, one major direction is to reduce the NW thermal conductivity while maintaining its electrical conductivity, which is based on the understanding that the intrinsic phonon mean free path (MFP) in bulk thermoelectric materials could be significantly longer than the corresponding electron MFP. If so, then for NWs, surface scattering could drastically decrease the lattice thermal conductivity without significantly affecting the electrical conductivity, which could lead to much enhanced ZT. This idea, together with other applications that need better understanding of thermal transport through NWs, has motivated extensive experimental and theoretical studies of NW thermal conductivity in the past two decades.

Exciting discoveries have been made that are promising for tuning the thermal conductivity of NWs. The thermal conductivities of many different kinds of NWs/nanoribbons have been explored, and the underlying mechanisms governing

DOI: 10.1021/acs.chemrev.8b00627
Chem. Rev. XXXX, XXX, XXX−XXX

the transport process have been dissected. In general, beyond the well-recognized classical size effect due to phonon-boundary scattering, several new factors, such as surface roughness, acoustic softening, and kink morphology, have been shown to be able to significantly alter the thermal conductivity of NWs. It is important to point out that the fundamental understandings obtained from the study of NWs greatly advanced our knowledge of thermal transport in materials beyond NWs. This is because the wire surface provides new boundary conditions to examine the contributions of different scattering mechanisms to the transport of energy carriers.

Studies of thermal transport through NWs have been carried out by both experimental and theoretical approaches. Experimental measurements of thermal transport through individual NWs are particularly challenging because of several factors. First, as with any thermal transport property measurements, these experiments suffer from the fact that there is no perfect thermal insulator, and thermal radiation occurs even in vacuum. As such, the sample has to be arranged as one branch in a thermal bridge to compete with some other heat transfer routes. Second, sample preparation can be very difficult, especially for NWs of small diameters. Moreover, the total thermal conductance to be measured can be really small. For example, a 20 nm diameter and 5 μm long NW with a thermal conductivity of 10 W/m-K possesses a thermal conductance of only 0.628 nW/K. Finally, contact thermal resistance between the NW and the heat source/sink has to be properly addressed in the measurement scheme. Several experimental techniques have been developed and successfully applied in the measurements of the NW thermal conductivity, and we will briefly review them below.

On the theoretical side, efforts have been made mainly along two approaches: one is to solve the BTE, and the other is to conduct molecular dynamics (MD) simulations. Remarkable progress has been achieved at both fronts, and in fact, open-source software packages are now available for both approaches. These powerful modeling tools allow for explanations and sometimes predictions of thermal transport properties of NWs. Since the fundamentals of these theoretical studies are well-described in several text books,[187] we will only include theoretical research results as part of the physical understanding of thermal transport through NWs.

In the following, we will first very briefly review the experimental measurement techniques for measuring the thermal conductivity of NWs and then summarize the published literatures based on the major nanoscale effects governing thermal transport through NWs. We will emphasize the physical understandings obtained from these studies.

4.1. Experimental Measurement Techniques

Measurements of thermal transport through NWs first became possible with the establishment of the thermal bridge scheme based on a microdevice with two side-by-side suspended SiN_x membranes (Figure 13a) integrated with Pt serpentine coils serving as both resistance heaters and thermometers.[37] A NW sample can be placed between these two membranes and the device is put into a cryostat under high vacuum, which eliminate convection heat transfer between the two membranes. The background conductance was mainly through radiation, which has been determined to be ~300 pW/K at room temperature and reduces as temperature drops.

During the measurements, a DC electrical current is passed through the heating side, which dissipates Joule heat and raise the temperature of the membrane. A portion of the heat will be conducted through the NW sample to the other membrane (sensing side) and increase its temperature. The temperatures on both sides can be measured with a small AC current using the lock-in technique. Considering the thermal resistance network of the whole setup, the total thermal conductance of the NW can be extracted based on the total power dissipation and the temperature rise on the heating and sensing membranes.

The dominant noise source in the original experimental setup is the temperature fluctuations of the two suspended membranes due to the fluctuation of the sample holder temperature in the cryostat. To eliminate this noise, Wingert et al.[188] improved the measurement scheme through introducing a blank device without NW samples and placed it in the cryostat together with the measurement device, which allowed for common-mode rejection to eliminate the noise from membrane temperature fluctuation through constructing a full Whitestone bridge (Figure 13b). This approach leads to a much better measurement resolution and pushes the minimum measurable thermal conductance down to ~10 pW/K. Importantly, this improvement enabled accurate determination of the background conductance, which could be subtracted from that of the sample. Therefore, this is a critical step in the experimental technique allowing for measurements of samples with thermal conductance smaller than the background conductance.

One key issue in these measurements is the thermal resistance at the contacts between the suspended membranes and the NW sample, which has to be minimized to a negligible level or can be determined to allow for extraction of the thermal resistance of the NWs sample. The contact resistance can be significant if the sample is placed on the device through a dry transfer process with loose contact between the sample and the membrane or if the contact area is relatively small. Without proper contact treatment to reduce the contact resistance to a value much smaller than the intrinsic thermal resistance of the sample, the obtained thermal conductivities could be much lower than the actual value, as pointed out by several studies.[48,189,190] Several approaches have been developed to minimize this contact resistance. One common strategy is to locally deposit materials at the contact between the NW sample and the suspended membranes, which can be done using a dual-beam focused ion beam (FIB). It is worth noting that energetic ion beams can easily alter the structure of the NW sample so it is often preferred to use electron beam induced deposition (EBID) with the focused electron beam in the FIB. A mixture of either platinum or gold with amorphous carbon is usually deposited and unless that sample thermal conductance is very high, the treatment can usually reduce the contact thermal resistance to be much lower than the sample resistance. To check whether the treatment reduce the contact resistance to a negligible value, a second deposition can be done after measuring the NW conductance.[33,191] If the extracted conductance after the second EBID is essentially the same as that with a single EBID, then the contact resistance can be regarded as being reduced to a negligible level.

Other approaches have also been developed to evaluate the contribution from the contact thermal resistance. For example, Mavrokefalos et al.[94] developed a four-probe approach to estimate the contact thermal resistance by measuring the Seebeck coefficients across two different pairs of electrodes patterned on the suspended membranes. In addition, through

DOI: 10.1021/acs.chemrev.8b00627
Chem. Rev. XXXX, XXX, XXX−XXX

aligning the same sample multiple times with different suspended lengths between the two membranes, Yang et al.[192] were able to extract the contact thermal resistance as well as the intrinsic thermal conductivity of multiwalled carbon NTs.

Another development based on the suspended microdevice is the incorporation of a local heating source using a focused electron beam inside a scanning electron microscope (Figure 13c).[193] The highly focused electron beam generates a local heating spot on the NW sample with a spatial resolution determined by the electron−phonon interaction volume, typically ∼20 nm for silicon. Since the electron beam can be scanned along the NW sample, this approach can easily measure the resistance of wire segments of different lengths. Through solving the governing equations of heat transfer in the thermal resistance network, the NW thermal conductivity as well as the contact thermal resistance can be extracted.

More recently, Shi and co-workers developed a thermal four-probe measurement scheme (Figure 13d), which includes four metal lines as temperature sensors.[195] The approach allows for simultaneous extraction of the contact thermal resistance together with the intrinsic thermal conductivity of the sample, even though a much more complex thermal resistance network has to been considered (Figure 13e). In addition to the above-mentioned thermal bridge methods, measurement schemes based on self-heating of electrically conducting NWs have also been developed.[196,197] For insulating NW samples, a thin layer of metal can be deposited on the NW and serve as the sensor.[198]

These developments allow for precise measurement of the NW thermal conductance; however, to extract the conductivity, it is necessary to accurately determine the NW dimension. While for a NW of a few micrometers long, its length can usually be extracted using SEM with a small error, the uncertainty associated with the cross-sectional size measurement is often the dominant source of error in the derived thermal conductivity. For NWs with a cross-section of regular shapes such as circles or squares, the cross-sectional size can be easily determined using SEM, even though the relatively uncertainty becomes larger as the wire size gets smaller. For NWs of irregular cross-sectional shape, it is necessary to cut open and image the cross-section directly, as done for several different NWs.[191,199] We also note that for nanoribbons of rectangular cross-section, it is possible to use AFM to extract the cross-sectional size,[200] which could be more accurate than that from SEM for smaller samples.

In addition to the measurement schemes as discussed above, other techniques, such as the T-bridge method,[201] self-heating 3ω method,[202,203] micro-Raman thermometry,[204−206] etc., have also been used to measure thermal and thermoelectric properties of NWs. In fact, the T-bridge method and micro-Raman thermometry have been used by quite a few groups in thermophysical property measurements of carbon NTs and graphene. The T-bridge method can be regarded as a special hot-wire approach with one end of the sample placed on a hot wire and the other side connected to a heat sink and the hot wire temperature profile is similar to that of the heater line for the four-probe approach in Figure 13d. Micro-Raman thermometry takes advantage of the temperature dependence of Raman spectrum to extract the temperature distribution along a NW/NT sample and determine its thermal conductivity. Major challenges of micro-Raman thermometry include the poor temperature sensitivity of tens of kelvin, and difficulty to accurately determine the laser power absorption. Efforts have been made to demonstrate their capabilities of measuring thermophysical properties of NWs, but the relevant publications so far have been focused on showing the capability instead of exploring new thermal transport physics. The main purpose of this section is to provide a brief background of the measurement techniques relevant to the discussion of the thermal and thermoelectric properties of NWs below. For more comprehensive and thorough discussion of the measurement techniques, we refer to recent review articles focusing on nanoscale thermometry.[207,208]

In summary, partly inspired by exploring the thermoelectric properties of NWs, impressive progress has been made in nanoscale thermal metrology, which allowed for extensive experimental studies of the thermal and thermoelectric properties of NWs and led to many exciting scientific discoveries, as reviewed in this paper.

4.2. Nanoscale Effects Governing Thermal Transport through Nanowires

4.2.1. Classical Size Effects. As mentioned in the Introduction, semiconductors possess the best thermoelectric properties, and for semiconductors, heat transport is dominated by quantized lattice vibrations or phonons. Owing to the extremely large surface-area-to-volume ratios of NWs, scattering between phonons and NW surface, or the classical size effect, can drastically reduce the lattice thermal conductivity. In deriving the lattice transport properties, we can treat phonons as particles, and the lattice thermal conductivity can be obtained using the kinetic theory as

$$\kappa = \frac{1}{3} C v \Lambda \tag{16}$$

Here, C, v, and Λ are the volumetric heat capacity, speed of sound, and phonon MFP, respectively. The phonon MFP defines the average distance a phonon travels between two consecutive scattering events, which can be calculated on the basis of the MFP for each specific phonon scattering mechanisms using the Matthiessen's rule, as

$$\frac{1}{\Lambda} = \frac{1}{\Lambda_U} + \frac{1}{\Lambda_d} + \frac{1}{\Lambda_{e\text{-}ph}} + \frac{1}{\Lambda_b} \tag{17}$$

where Λ_U, Λ_d, $\Lambda_{e\text{-}ph}$, and Λ_b are the MFPs determined by the *Umklapp* scattering, defect scattering, electron−phonon scattering, and boundary scattering, respectively. The first three terms determine the intrinsic phonon MFP (Λ_i) in bulk materials and the last term, which is only important at very low temperatures for bulk materials, could become much more significant for NWs. For NWs, if the intrinsic phonon MFP becomes larger than the characteristic length of the wires (i.e., Casimir length, usually taken as the wire diameter), the effective phonon MFP can be drastically reduced by phonon-boundary scattering with Λ_b as the dominant term on the right-hand side in eq 17. This understanding is well-recognized as the classical size effect.

The exploration of classical size effects on thermal transport in nanostructures started with thin films. For example, Ju and Goodson studied Si thin films with a thickness of 74−240 nm and showed that the thermal conductivity of the measured films demonstrated a strong size dependence, with the maximum reduction as much as 50% of the bulk value at room temperature.[209] Their analysis further indicated that the intrinsic phonon MFP in bulk Si could be as long as 300 nm at

DOI: 10.1021/acs.chemrev.8b00627
Chem. Rev. XXXX, XXX, XXX−XXX

room temperature, nearly an order of magnitude larger than the value of 43 nm predicted by eq 16 without considering the phonon dispersion.[209]

The first experimental results on the thermal conductivity of NWs were reported by Li et al. for individual Si NWs of 22, 37, 56, and 115 nm diameters.[17] The measured data show more than 1 order of magnitude reduction from the corresponding bulk values at low temperatures and also demonstrate a strong size dependence with lower thermal conductivity for smaller diameter wires. This set of data attracted significant attention and extensive efforts have been made to model thermal transport in Si NWs and explain the underlying transport mechanisms.[210−213] While most theoretical modeling taking into account the classical size effect can fit the experimental data for the three larger diameter wires reasonably well, all efforts failed to recapture the data for the 22 nm diameter wire.[211]

In addition to NWs with circular cross section, Si NWs of other cross-sectional configurations, such as rectangular, have also been studied.[214,215] These studies show that neither the smallest lateral dimension nor the Casimir length is an appropriate characteristic length to quantitatively determine the classical size effect (Figure 14a). For example, it is pointed out that for NWs of similar Casimir length, the thermal conductivity of NWs of different cross sections can vary by almost three folds.[214] Instead, it appears that the surface-area-to-volume ratio, which better characterizes the phonon-boundary interactions, could well quantify the classical size effect, as evidenced by the monotonic dependence of thermal conductivity on the surface-area-to-volume ratio for different silicon nanostructures (Figure 14b). This is an important understanding from the study of thermal transport through NWs, and physically it is also more reasonable because the surface-area-to-volume ratio represents the relative importance of surface while the Casimir length only emphasizes the equivalence of the cross-sectional area.

One notable consequence due to classical size effects is that as boundary scattering suppresses the capability of acoustic phonons to transport heat, the contribution from optical phonons to heat conduction could become more significant. For bulk materials, optical phonon modes are often neglected when considering thermal transport because of the rather small group velocities of these phonons, which was confirmed to be a reasonable approach for bulk Si and Ge by Ward and Broido.[221] However, in NWs the optical phonons may no longer be negligible. For example, using first-principles calculations, Tian et al. showed that for a 20 nm diameter Si NW, optical phonons can contribute up to 18% at room temperature, as compared to merely 5% for bulk Si.[222] This understanding is also supported by a recent experimental work on thermal conductivity of individual Si NWs in a temperature range up to 700 K.[40] It was shown that for a 20 nm diameter Si NW, the contribution from optical phonons could be 20% at 700 K, and the relative importance of the optical phonons increased for smaller diameter wires.[40]

It is also worth noting that while classical size effects often play a dominant role leading to the most significant contribution to the reduced thermal conductivity, other effects could still be important, which could be utilized to further improve the NW thermoelectric performance. For example, it has been experimentally shown[223] and then theoretically corroborated[224] that for Si NWs, adding isotope atoms could still lead to up to 30% thermal conductivity reduction. It is important to realize that the relative importance of the classical size effect and other phonon scattering mechanisms strongly depends on the NW size. Unfortunately, this information is not readily available in ref 223.

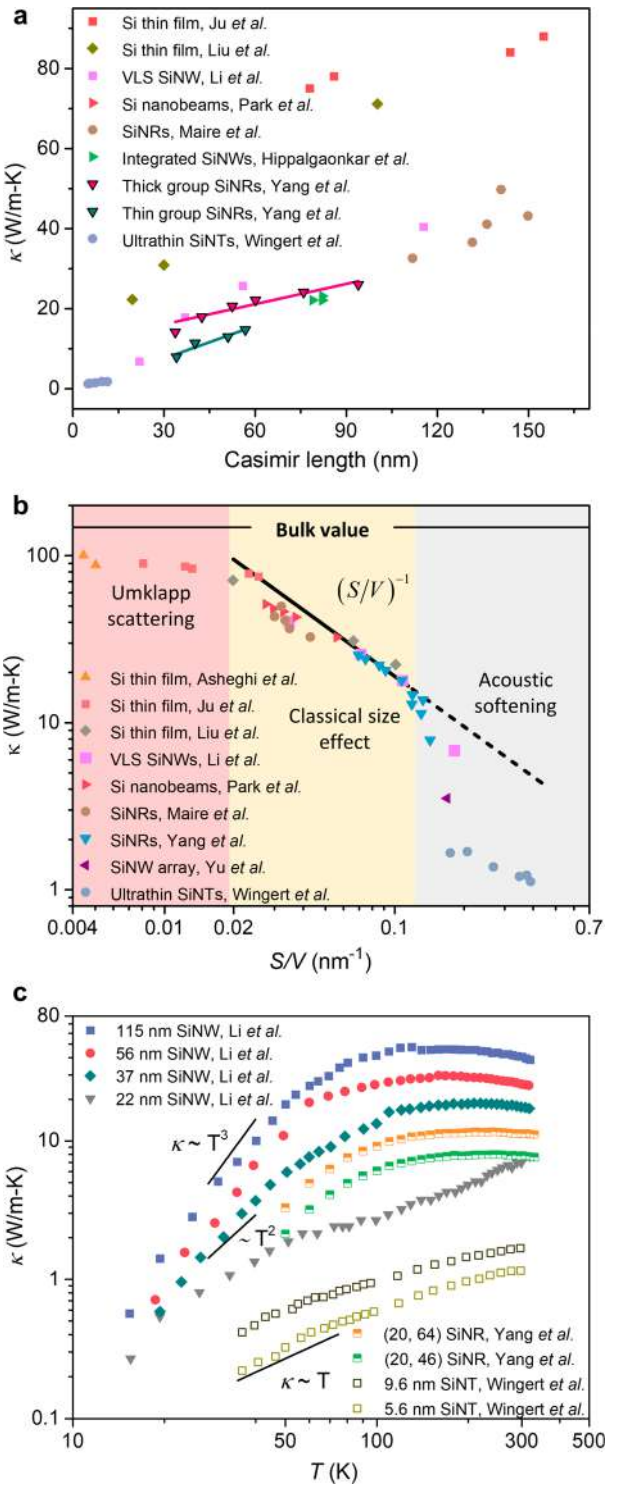

Figure 14. (a, b) Room temperature (300 K) thermal conductivities of various silicon nanostructures versus their (a) Casimir lengths and (b) surface-area-to-volume ratios (S/V).[17,209,214−220] (c) Low-temperature thermal conductivity data of various Si nanostructures on a logarithmic scale.[17,214,220] Also shown are T^3, T^2, and T^1 curves for comparison.

DOI: 10.1021/acs.chemrev.8b00627
Chem. Rev. XXXX, XXX, XXX−XXX

In addition to the silicon nanostructures, thermal transport through other types of NWs has also been extensively studied. For example, following the work on Si NWs, Li et al. reported the thermal conductivity of Si/SiGe superlattice NWs.[22] The obtained data were below the alloy limit set by the corresponding bulk SiGe, which was attributed to the combined effects of two major scattering mechanisms to block phonons of different frequencies. High-frequency phonons are sensitive to atomic scale impurities; and therefore, alloy scattering could pose significant resistance to their transport, which occurs in both bulk SiGe and the SiGe segment of the Si/SiGe superlattice NWs. What helps to beat the alloy limit is the surface scattering of low-frequency phonons, which are not sensitive to alloy scattering and have quite long intrinsic MFP in bulk SiGe.

SiGe is an important high-temperature thermoelectric material, and significant efforts have been devoted to study its thermal properties. By ∼2010, it was realized that because of the significant alloy scattering for high-frequency phonons, low-frequency phonons make relatively more contribution to thermal transport in SiGe and the intrinsic phonon MFP could be actually longer than that of silicon, larger than 1 μm at room temperature.[124,225,226] This understanding allows for further suppression of thermal conductivity in SiGe NWs based on the classical size effect, and hence further enhancement of the thermoelectric figure of merit.

Several groups have explored experimentally the thermal conductivity of SiGe NWs. Kim et al. first measured the thermal conductivity of SiGe NWs with Ge concentration ranging from 0.4% to 9% for NWs of 140−334 nm diameter, and showed that at the same Ge concentration, the thermal conductivity of SiGe NWs became lower as the wire diameter reduced.[21] Even though the decreasing trend is discernible, the observed dependence on the wire diameter is not very significant and the authors concluded that alloy scattering should be the dominant scattering mechanism. A quickly following theoretical study by Wang and Mingo provided a reasonable fitting of the experimental data of Kim et al. and disclosed relatively minor diameter dependence.[227] Wang and Mingo's results also showed that even for 500 nm diameter wires, their thermal conductivity could be significantly lower than that of the corresponding bulk value at the same Ge concentration.[227] We believe this could be due to the fact that the low-frequency phonons could have MFPs much longer than 500 nm and the classical size effect becomes important at rather large sizes. In fact, the thermal conductivity is already reduced to about one-third of the bulk value for 500 nm diameter wires, and because the contribution of low-frequency phonons has been significantly suppressed, the relative importance of higher frequency phonons increases and the size dependence becomes less remarkable. The prediction did suggest that for even smaller wires, the size effect could become more significant again as the wire diameter gets really small and boundary scattering dominates over alloy and anharmonic scattering.

The thermoelectric properties of tapered SiGe NWs were characterized by Martinez et al. for wires of two different boron doping levels and several average diameters through measuring the Seebeck coefficient and electrical and thermal conductivities, respectively.[228] Their results suggest that boundary scattering further suppresses the thermal conductivity and the room temperature ZT is twice that of the bulk SiGe alloy. In additional to boundary scattering, it is claimed that hole−phonon scattering also plays a role in lowering the thermal conductivity to that of silica. In 2012, Yu and co-workers published two papers reporting the thermal and thermoelectric properties of SiGe NWs.[43,126] Their results suggested that the ZT value of SiGe NWs could be ∼0.46 at 450 K, significantly higher than that of bulk SiGe. No clear dependence of the thermal conductivity on the wire diameter can be discerned from these two papers as the Ge concentration varies from sample to sample. We note that at the time of publication of these two papers, accurate background thermal conductance between the heat source and heat sink in the measurement setup had not been able to be extracted through introducing the Whitestone bridge scheme based on the principle of common-mode rejection, and as such, the thermal conductivity data for some small diameter SiGe wires could be influenced significantly by the background conductance.

The most intriguing and puzzling data for the thermal conductivity of SiGe NWs are probably from Hsiao et al., who showed persistent room-temperature ballistic thermal conduction along SiGe NWs up to 8.3 μm.[229] Interestingly, no clear diameter dependence was found in these SiGe NWs with a diameter range from ∼50 to 200 nm and in addition, the thermal conductivity seems insensitive to the Ge concentration for two different compositions with 10% and 60% Ge. These data contradict all previous experimental results and common understanding of the classical size effect, and why phonon-boundary scattering disappears in these NWs is still a mystery. One more interesting observation in the reported data is that the thermal conductivity follows a nearly perfectly linear trend up to 8.3 μm, and change to be flat rather abruptly, instead of the normal asymptotic transition with gradual deviation from the linear curve as expected for the ballistic to diffusive transition.

While the thermal properties of Si and SiGe alloy NWs are the most widely studied, efforts have been made to understand thermal transport in NWs made of other materials. Relevant to thermoelectric applications, quite a few measurements have been done on Bi_2Te_3 NWs. Most of these measurements were conducted on electrodeposited Bi_2Te_3 NWs prepared with anodic alumina template.[31,93,230−232] In addition to the diameter variations, chemical composition and crystalline structure of these NWs can change from wire to wire even for wires prepared in the same run. The diameters of most measured NWs are also quite large compared to the intrinsic phonon MFP in bulk Bi_2Te_3 (<10 nm);[233] and therefore, no solid evidence of thermal conductivity reduction from classical size effects could be discerned. We note that one recent publication claimed that boundary scattering in smaller NWs of 25−52 nm diameter could lead to significant size dependence with lower thermal conductivity for smaller wires;[234] however, the measurement was done on wire-template composite films and the derivation of the NW thermal conductivity involved quite a few parameters. As a result, very large uncertainties are associated with the obtained thermal conductivity. The extremely small lattice thermal conductivity derived for the 25 nm diameter wire, 0.18 W/m-K, also seems too low, given the ∼3 nm intrinsic phonon MFP for Bi_2Te_3, and the observation is also not consistent with the MD simulation result.[235]

Another class of thermoelectric NWs that have been studied is the lead chalcogenide (PbX (X = S, Se, Te)) NWs. Several reports have suggested that the thermal conductivity of these NWs could be reduced by the classical size effect at a rather

DOI: 10.1021/acs.chemrev.8b00627
Chem. Rev. XXXX, XXX, XXX−XXX

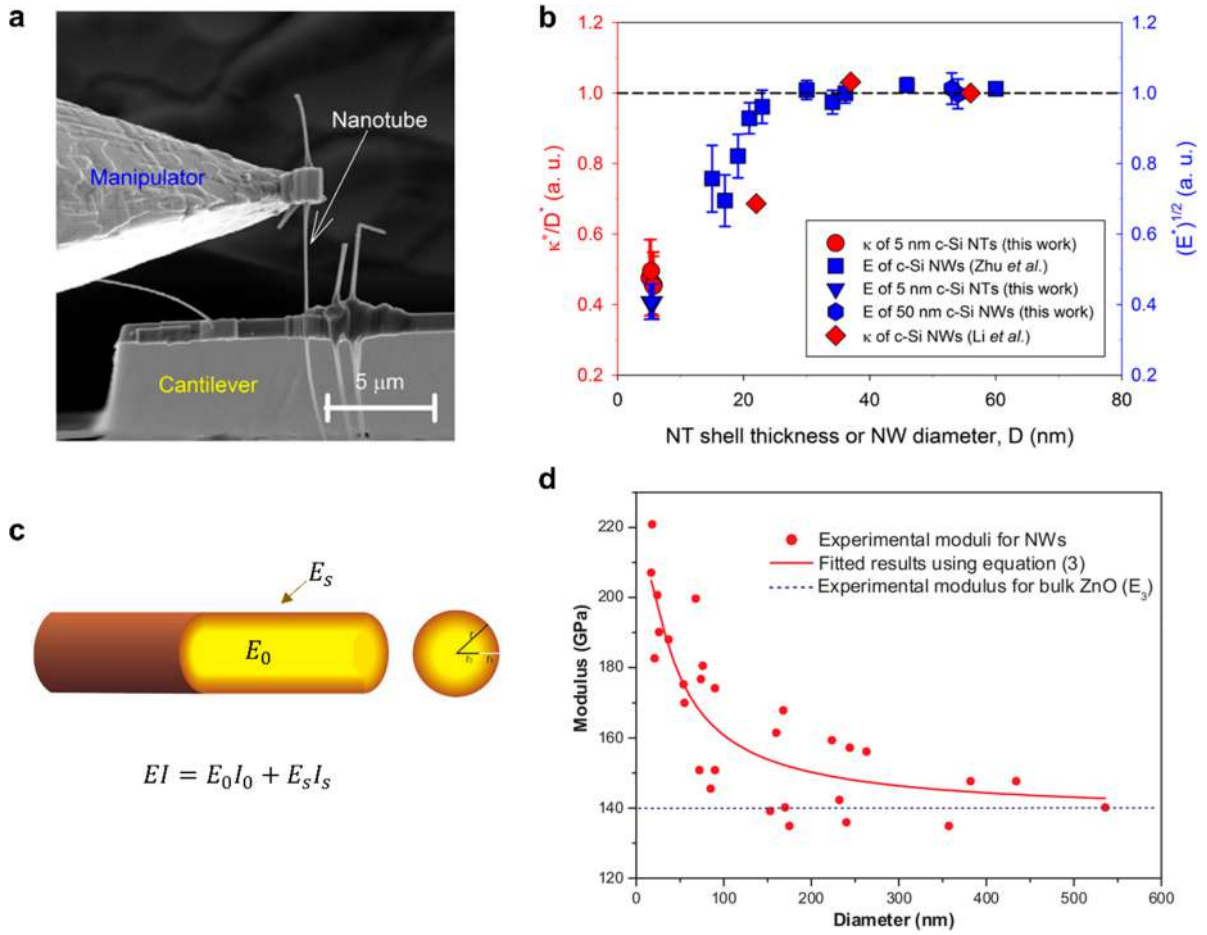

Figure 15. (a) Elastic modulus tensile measurement using a manipulator probe to pull a Si NT attached to the end of an AFM cantilever.[220] (b) Elastic moduli of silicon NTs and NWs.[220] (a, b) Reprinted with permission from ref 220. Copyright 2015 American Chemical Society. (c) Schematic illustration of the core−shell composite NW model.[240] (d) Diameter dependence of the effective Young's modulus in [0001] oriented ZnO NWs for bending: (red dot) experimental results, (solid line) fitted results by the core−shell composite NW model, (blue dotted line) modulus for bulk ZnO (E_3) calculated using the experimental data.[240] (c, d) Reprinted with permission from ref 240. Copyright 2006 American Physical Society.

large diameter of ∼250 nm, which could be very beneficial to thermoelectric applications.[27,236] However, MD simulations suggested that the classical size effect should be significant only when the wire diameter reached tens of nanometers.[237] This discrepancy needs to be addressed by further studies.

In general, the classical size effect could lead to much reduced NW thermal conductivity, as long as the NW characteristic size is less than the intrinsic phonon MFP in the corresponding bulk materials, which has been clearly demonstrated from the above-discussed NW systems and a few other types of NWs. In fact, one major conclusion from studying phonon transport in nanostructures in the past 20 years is that the intrinsic phonon MFP in bulk materials could be drastically larger than that derived based on simple kinetic theory (i.e., eq 16) because many high-frequency phonons, while taking heavy weight in the heat capacity, do not contribute to thermal transport due to their extremely small group velocity. As such, the phonon MFP for many thermoelectric materials could be significantly larger than the electron MFP, which allows for tailoring the lattice thermal conductivity of NWs to enhance ZT.

4.2.2. Acoustic Softening. As mentioned previously, the thermal conductivity of the 22 nm diameter Si NW cannot be accounted for by any theoretical modeling purely based on the classical size effect. To confirm this, Chen and co-workers measured more thin Si NWs and thin Ge NWs, which showed similar trends that could not be recaptured based on the classical size effects in these thin NWs.[212,238] In addition to the lower thermal conductivity values, the temperature dependence of the thermal conductivity of these thin NWs is also significantly different from the larger NWs. For example, at low temperature, the temperature dependence deviates from the Debye T^3 law, while for larger wires, NW thermal conductivity follows the Debye T^3 law very well at low temperature (Figure 14c).

The intriguing behavior of the thermal conductivity of small diameter Si and Ge NWs has attracted a great deal of attention without convincing physical explanations until 2015, when Wingert et al. reported a systematic study of the thermal conductivity of ultra-thin Si NTs with wall thickness as small as 5 nm.[220] Similar to thin Si and Ge NWs, the Si NTs also displayed thermal conductivities much lower than that could be accounted for by the classical size effect; and in fact, the values are even lower than that of amorphous Si NTs with similar geometries. Importantly, they noticed that the Young's modulus of individual Si NWs measured from the elastic tensile tests demonstrated a sharp reduction from the bulk value as the wire diameter became smaller than 30 nm.[239]

DOI: 10.1021/acs.chemrev.8b00627
Chem. Rev. XXXX, XXX, XXX−XXX

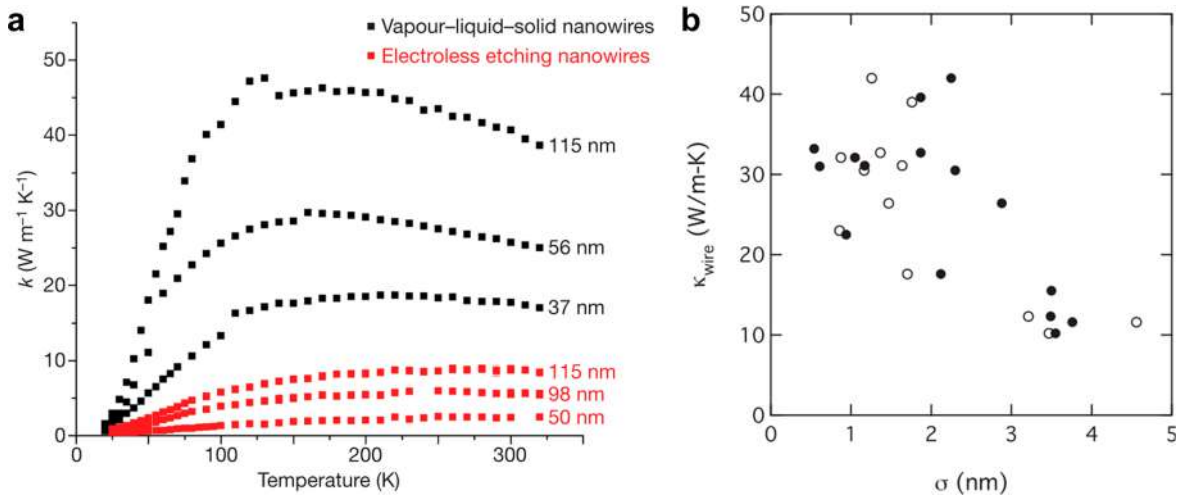

Figure 16. (a) Temperature-dependent thermal conductivity of VLS Si nanowires[17] (black squares) and EE-Si nanowires (red squares).[33] Reprinted with permission from ref 33. Copyright 2007 Nature Publishing Group. (b) Measured room temperature thermal conductivity of rough Si NWs versus RMS roughness, σ.[247] Reprinted with permission from ref 247. Copyright 2012 American Institute of Physics.

Similar characterization on each individual Si NTs (Figure 15a) yielded tube Young's moduli up to 6-fold lower than the bulk value (Figure 15b). Since speed of sound is proportional to the square root of Young's modulus, the drastically reduced Young's modulus value indicates strong elastic softening in thin Si and Ge NWs as well as the crystalline Si NTs with thin walls, which subsequently leads to lower thermal conductivity.[220] This new finding by Wingert et al. thus points out a new route to further reduce the lattice thermal conductivity and enhance the thermoelectric performance of NWs.[220]

In fact, the alteration of the Young's modulus has more profound effects. The Young's modulus can be derived as the ratio of the interatomic spring constant to the crystal lattice constant. The lattice constant does not change significantly even for thin NWs; therefore, the change of the Young's modulus must mainly come from the variation of the interatomic spring constant, which is a key parameter in the derivation of phonon dispersion. As such, the mechanical property change will totally alter the phonon properties and lead to very different thermal conductivity behavior. For NWs with reduced Young's modulus, if the electronic properties are not significantly altered, acoustic softening could be a viable approach to enhance *ZT*.

One potential issue is that structural defects could play a significant role in the reduced Young's modulus,[241] which raised questions about the quality of the Si NTs and whether structural defects play any roles in the observed Young's modulus reduction. This has been addressed by a following up work that measured Si nanoribbons of two different thicknesses (~20 and 30 nm).[214] The Si nanoribbons were prepared through nanofabrication from the high-quality single crystalline device silicon layer of SOI wafers and should not have much structural defects. Importantly, even there are defects, the defect density should be approximately the same for different thickness ribbons. Therefore, the observation that the 20 nm thick ribbons, whose Young's moduli are much lower than those of 30 nm thick ribbons, have much reduced thermal conductivities beyond that predicted on the basis of the classical size effect strongly suggests that the acoustic softening is not from structural defects but from different states of surface atoms (Figure 15c). The importance of surface effects in acoustic softening can be clearly seen from Figure 14b, which indicates that as the surface-area-to-volume ratio becomes larger than a critical value, the thermal conductivity does not follow the trend delineated by the classical size effect.

Recently, the acoustic softening effect has also been used to explain the ultra-low thermal conductivity of porous Si NWs (~0.33 W/m-K at 300 K for a porosity of 43%);[242] however, in general, the multi-physics phenomena of acoustic softening still have not been well-explored. For example, while acoustic softening and the associated thermal conductivity reduction have been confirmed for Si NWs, no combined study of both mechanical and thermal properties for other type of NWs have been carried out, while Young's modulus reduction has been observed for several other kinds of nanostructures. For example, measurements on thin Cr cantilevers suggested that the Young's modulus continuously decreased as the size reduced to below 83 nm.[243] On the other side, there have been reports for several types of NWs, including Ag, Pb, GaN, and ZnO wires,[240,241,244] whose Young's moduli increase rapidly with decreasing diameters. For example, as shown in Figure 15d, the Young's moduli of ZnO NWs along the axial direction have been measured for wires with diameters ranging from 17 to 550 nm; it was found that the Young's modulus increased drastically as the size reduced to below 120 nm.[240] However, results from separate thermal measurement of ZnO NWs conducted by Bui et al.[245] did not reflect the effects of the Young's modulus change. This could be due to the fact that the smallest pristine NW they measured is still 70 nm diameter, while more remarkable Young's modulus enhancement occurs for wires of <50 nm in diameter according to Chen et al.[240] In addition, a full scope study of all changes in the heat capacity, phonon group velocity and MFP from the Young's modulus change in small NWs should be carried out to dissect how different factors contribute to thermal conductivity variations. Finally, further study is still needed to elucidate the role of acoustic softening on the deviation of T^3 dependence of thermal conductivity in smaller-sized Si nanostructures (Figure 14c). Important for thermoelectrics, it is critical to explore whether acoustic softening is accompanied by any side effects on electrical transport to determine whether acoustic softening

DOI: 10.1021/acs.chemrev.8b00627
Chem. Rev. XXXX, XXX, XXX−XXX

can be a viable approach to further enhance the thermoelectric figure of merit.

4.2.3. Surface Roughness. One of the most remarkable *ZT* enhancements over the bulk value reported so far is from Si NWs with rough surfaces,[33] which has been attributed to the ultra-low thermal conductivity of the wires prepared via electroless etching (EE-Si NWs). As shown in Figure 16a, compared with Si NWs of smooth surfaces and similar diameters, the Si NWs with rough surfaces demonstrate much lower thermal conductivity, even approaching the amorphous limit for a ∼50 nm diameter wire, which is far below any prediction based on the classical size effect. This intriguing observation attracted a great deal of attention and fueled a lot of research to explore the detailed mechanisms responsible for the ultra-low thermal conductivity.

Experimentally, Park et al. explored the roughness effects with Si NWs synthesized through VLS or vapor−solid (VS) method and showed that surface roughness could indeed significantly reduce the NW thermal conductivity, even though the lowest thermal conductivity achieved was still rather high (∼18 W/m-K), since only relatively large diameter NWs of well over 100 nm diameters were studied.[246] Later, Lim et al. conducted extensive measurements of rough-surface Si NWs through simultaneously characterizing both the thermal conductivity and surface roughness of the same NW.[42] Instead of using NWs prepared via electroless etching, the NWs were prepared through surface etching of smooth NWs prepared with the VLS method. Quantitative parameters describing the surface roughness were extracted from detailed transmission electron microscopy (TEM) characterization of the surface roughness. It was shown that larger surface roughness corresponded to lower thermal conductivity, and importantly, the thermal conductivity value could indeed drop far below the Casimir limit. In addition, Feser et al. measured the thermal conductivity of Si NW arrays prepared by a two-step process through first etching Si into NWs and then roughen the wire surface to avoid potential nanoscale pores in the wire.[247] Their results also showed that the thermal conductivity of the NWs dropped as the surface roughness enhanced (Figure 16b). The author also conducted Raman spectroscopy examination of the NWs and found broadened Raman line widths, on the basis of which it was proposed that microstructural changes might be associated with rough NWs. In a separate effort, Blanc et al. fabricated Si nanoribbons with corrugated sidewalls using e-beam lithography and the measured thermal conductivity values were shown to be strongly reduced compared with straight wire, which provided additional evidence for that surface roughness could indeed reduce the thermal conductivity below the Casimir limit.[248] To explore the underlying mechanisms, Monte Carlo (MC) ray-tracing simulations were carried out, which indicated that backscattering of ballistic phonons on the corrugated surfaces could pose significant resistance to phonon transport. One limitation is that the experiment was done in a relatively small range of very low temperature spanning 0.3−5 K, where the wavelength of thermal phonons could be much larger than the random surface roughness.

Theoretically, the effect of a non-smooth surface on the thermal transport of NWs was first investigated by Moore et al. through applying MC simulations to study phonon transport in a NW with periodic sawtooth features on the surface.[249] Their results suggested that despite the overall increase in the solid volume of the NW, backscattering of the phonons could suppress the thermal conductivity. However, the reduction is not significant enough to account for the low thermal conductivity reported for the rough EE-Si NWs. Later on, Wang et al. further showed with MC simulations that for rough NWs with sharp roughness features of less than 90° apex angles, multiple scattering events could further reduce the NW thermal conductivity.[250] However, to fit the experimental data of EE-Si NWs, the impurity scattering strength has to be enhanced. In addition, Sansoz conducted extensive MD simulations on thermal transport through Si NWs with periodic sawtooth facets, and the results suggested that these surface features could reduce the thermal conductivity by up to 55% as compared to NWs of the same size with circular sidewalls.[251] Importantly, given that Si surface usually has a thin oxide layer, it was shown that addition of a thin amorphous layer to the surface of the Si NWs did not alter the trend.

To understand the effects of surface roughness, Martin et al. introduced an additional frequency-dependent phonon scattering term to characterize the phonon interaction with the surface roughness.[41] Based on the first-order perturbation theory, also known as the Born approximation, the roughness induced scattering rate was calculated and the thermal conductivity was derived. Their results suggested drastic reduction of thermal conductivity as the root-mean-square (RMS) roughness increased to 3 nm. However, while they showed that surface roughness could indeed lead to thermal conductivity lower than the Casimir limit, Carrete et al. argued that the Born approximation should break down at wavelengths similar to the size of the scatterers.[252] Using an atomistic Green's function calculation, it was claimed that the phonon MFP and the thermal conductivity of a NW should not be far below the Casimir limit unless the roughness became more than 20% of the NW diameter. Realizing the limitation of the Born approximation, Sadhu and Sinha adopted the less restricted Bourret approximation in their Green's function study.[253] Based on a series of assumptions, they obtained the phonon transmission coefficients for both smooth and rough NWs that could match the experimental data reasonably well. One important point they made is that in addition to the RMS surface roughness, the correlation length could also play a critical role. However, validation of the assumptions for the model need to be done to confirm the accuracy of the model.

Efforts have also been made to clarify the surface roughness effects through MD simulations. Using non-equilibrium MD (NEMD) simulations, Liu and Chen showed that as the periodic length of the surface roughness reduced, the derived thermal conductivity became smaller.[254] However, since the simulation is conducted on very small NWs (∼1.63 nm diameter), the roughness RMS is limited, no quantitative comparison with experimental data can be made. He and Galli conducted a comprehensive equilibrium MD study of Si NWs of 15 nm diameter of different surface morphologies and both with and without internal structural defects (vacancies and grain boundaries).[255] Their results suggested that amorphous surface layers, surface oxide, surface roughness, and internal structural defects could all contribute to reduced thermal conductivity. For smooth Si NW core coated with 1 nm thick amorphous oxide, the thermal conductivity could achieve about 10-fold reduction from the bulk value. Surface roughness could further reduce the NW thermal conductivity by another 3-fold. However, only through combining the surface rough-

DOI: 10.1021/acs.chemrev.8b00627
Chem. Rev. XXXX, XXX, XXX−XXX

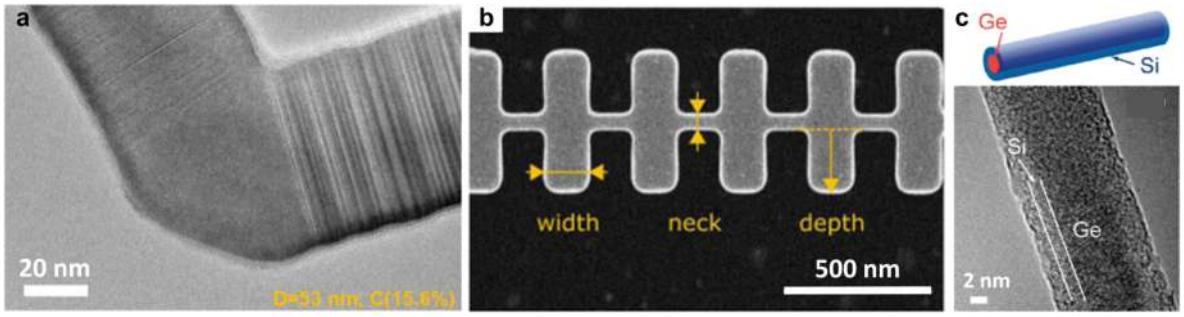

Figure 17. (a) HRTEM image showing a kinked boron carbide nanowire with 53 nm diameter. Reprinted with permission from ref 261. Copyright 2017 American Chemical Society. (b) SEM image showing a Si fishbone nanoribbon. Reprinted with permission from ref 262. Copyright 2018 Springer Nature. (c) Top: schematic illustration of a Ge-core Si-shell NW. Bottom: an HRTEM image of a single crystalline Ge−Si core−shell NW. The Ge core axial direction is [110], and the Si shell is epitaxially grown on Ge.[238] Reprinted with permission from ref 238. Copyright 2011 American Chemical Society.

ness and internal structural defects, the thermal conductivity could be reduced by about ∼100 times as seen in the EE-Si NWs. Even though this comprehensive MD study provides a lot of insights, the NW size in the modeling is still much less than the ∼50 nm diameter in the experimental study of EE-Si NWs.

In addition to Si NWs, Kim et al.[256] showed that the thermal conductivity of rough VLS-grown $Si_{0.96}Ge_{0.04}$ NWs of ∼250 nm diameter with a surface roughness of ∼23 nm was four times lower than that of corresponding smooth NWs. Through introducing an additional scattering term due to surface roughness that are most effective for mid-frequency phonons, the authors could fit the measured thermal conductivity reasonably well. Moreover, rather large Bi_2Te_3 NWs (∼270 nm diameter) with significant surface roughness (diameter varies from 190 to 320 nm) was found to have a thermal conductivity that is one-half that of a smaller (∼177 nm diameter) NW with smooth surface through a self-heating 3ω measurement.[257] The authors attributed the lower thermal conductivity to phonon backscattering at the indents on the boundaries. However, it seems that the authors did not distinguish the electron and phonon contributions to the measured thermal conductivity while the electrical conductivity of the surface rough NW is ∼40% lower than the smooth NW. Theoretically, Qiu et al. conducted equilibrium MD (EMD) simulations to model both smooth and surface rough (sawtooth) Bi_2Te_3 NWs; it was found that the thermal conductivity of the surface rough NWs could be ∼35% lower than that of the surface smooth NWs.[235]

Taken together, it seems that surface roughness could indeed be very effective in reducing the thermal conductivity of NWs; however, to date, a straightforward physical picture that can quantitatively account for how surface roughness leads to drastically reduced thermal conductivity is still not available. Further experimental and theoretical studies of the NWs with well-characterized and even designed surface roughness should be carried out to clarify this important issue. It is also worth noting that for EE-Si NWs etched from highly doped Si wafers, the etching process might generate some internal structural defects such as voids,[258] which was utilized by Zhao et al. to pursue the ultra-low thermal conductivity in nanoporous Si NWs.[242] A separate study[259] on porous Si NWs fabricated through metal-assisted chemical etching also indicated ultra-low thermal conductivity; however, the obtained thermal conductivity still displayed a linear dependence on the wire diameter, which was attributed to the anisotropic porous structure that arose during chemical etching. While nanoscale voids were not observed in the rough EE-Si NWs studied by Hochbaum et al.,[33] which were etched from lightly doped Si wafers, the impact on the low thermal conductivity by smaller, atomistic scale vacancies cannot be completely ruled out.

4.2.4. Effects of Complex Wire Morphology. In addition to the simple straight wire morphology and one single chemical composition, NWs of more complex morphologies have been synthesized and the effects of the more complex structure on thermal transport have been investigated. In terms of thermoelectric applications, several strategies can help to tune the NW thermal conductivity, which are discussed as follows.

Nanowires of more complex morphology, such as those with kinks, have been synthesized in controllable manners and demonstrated for different applications.[23] The effects of kinks on thermal transport were first studied numerically by Jiang et al. using NEMD simulations through constructing Si NWs with periodic kinks.[24] Their results showed that compared with the corresponding straight NW, at 300 K, the thermal conductivity could be reduced by more than 20% with a single kink and reaching a maximum reduction of up to ∼70% with 11 kinks. Based on the detailed information disclosed by the MD data, they reason that the reduction mechanisms are (1) the mandatory interchanging between the longitudinal and transverse phonon modes at the kink, and (2) the pinching effect for the twisting and transverse phonon modes at the kink, which comes from the different phonon wave vector directions for the same phonon mode at each side of the kink. Another numerical study reported by Xiong et al. calculated the thermal conductivity of Si NWs of a twinning superlattice structure with turning angle of 109.4°, leading to a zigzag configuration with many kinks along the wire.[260] The modeling results yield a level of thermal conductivity reduction of up to 65%, and mode analysis reveals that the minimal thermal conductivity arises from the disappearance of favored atom polarization directions, which is consistent with the physical picture of Jiang et al.[24]

Experimental demonstration of the kink effect on thermal transport only became available very recently.[261] Through systematic experimental measurements of the thermal conductivity of straight and kinked boron carbide NWs of different diameters and carbon concentrations (Figure 17a), Zhang et al. found that a single kink could lead to up to 36% thermal conductivity reduction. Evaluating the kink effect via thermal conductivity reduction could be misleading because

DOI: 10.1021/acs.chemrev.8b00627
Chem. Rev. XXXX, XXX, XXX−XXX

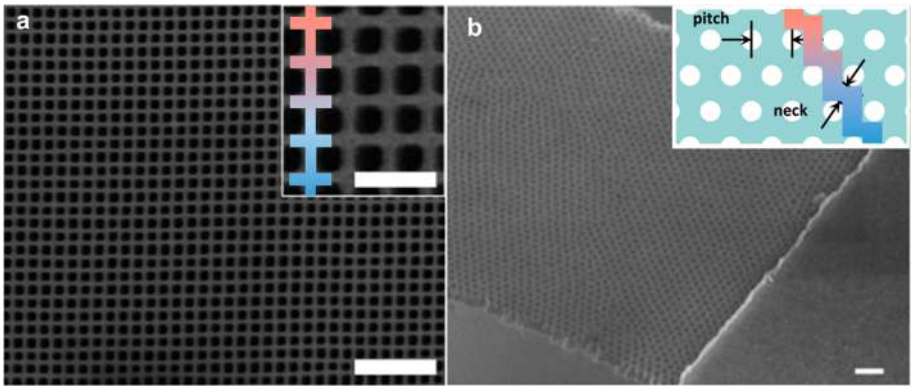

Figure 18. (a) SEM image of a periodic Si nanomesh with a controlled periodicity of 100 nm. The inset image shows that fishbone nanoribbons could be regarded as building blocks for nanomeshes with aligned hole arrangement. Scale bars are 200 nm (inset) and 600 nm (main).[268] Reprinted with permission from ref 268. Copyright 2017 Springer Nature. (b) Tilted SEM image shows the holey structure of the nanomesh ribbon, and the inset shows that kinked nanoribbons could be regarded as building blocks for nanomeshes with staggered hole arrangement. Scale bar is 200 nm.[269] Reprinted with permission from ref 269. Copyright 2016 American Chemical Society.

the difference could be influenced by the sample length; and a more informative approach of measuring the kink effect is to compare the kink induced additional resistance with the resistance of a straight wire segment of equivalent length to the kink. Doing so, it was found that the kink in these boron carbide NWs could pose a thermal resistance up to ∼30 times that of a straight wire segment of equivalent length, ∼ 7 times more pronounced than that from MD simulation of kinked Si NWs. Based on MC simulation, Zhang et al. attributed this remarkable kink resistance to the combined effects of backscattering of highly focused phonons and required mode conversion at the kink. Their argument is strongly supported by the finding that defects in the kink, instead of posing resistance, could actually facilitate phonon transmission through the kink via scattering phonons into the opposite arm. An important point here is the significant effect of phonon-focusing—the strong elastic anisotropy of boron carbides helps to align phonons along the wire axis, and enhance the backscattering of phonons, which could be taken advantage to design materials with desirable properties.

In addition to kinked NWs, another type of NWs that have drawn some attention is the fishbone NWs, prepared through top-down fabrication with fins attached to a backbone nanoribbon, as shown in Figure 17b.[262−264] Extracting the thermal conductivity using an effective width, it was shown that the thermal conductivity of the fishbone nanoribbon was significantly lower than that of corresponding straight nanoribbon, which was attributed to the reduced phonon group velocity in the fishbone wire. In fact, the authors named their fishbone NW as 1D phononic crystals to emphasize the reduced phonon group velocity due to phonon coherence effects and zone folding. Note that an earlier atomistic calculation of the thermoelectric property of a nanotree structure with ideal flat surfaces, which is essentially the building block of a fishbone NW, suggested that the thermal conductance of the nanotree could be lower by 17% as compared to that of pristine NW.[265] Phonon coherence, however, requires very strict conditions and its effects have only been observed unambiguously in superlattices with nearly perfect interfaces between the alternating layers.[266] It is difficult to imagine that the rather rough (∼1 nm) wire surface from reactive-ion-etching can specularly reflect thermal phonons and retain their coherence. In fact, an MD study of SiC NWs with periodic diameter modulation could provide some insights into the observed lower thermal conductivity of the fishbone NWs.[267] Although both are based on the backbone diameter, the derived thermal conductivity of the diameter modulated NW is ∼10% lower than that of the corresponding straight NW, which is attributed to the constriction resistance due to the phonon reflection when the cross-section area reduces.

The insights gained from the study of kinked and fishbone NWs could also be used to explain thermal transport through nanomeshes. In additional to NWs, nanomeshes have been extensively explored in the past decade for reduced thermal conductivity and thermoelectric applications.[219,269−273] As shown in Figure 18, kinked and fishbone NWs can be regarded as the building blocks of nanomeshes with staggered and aligned square holes.

Single-crystalline Si nanomeshes of ∼20 nm thick with periodic aligned holes were first fabricated and measured by Yu et al.,[219] and very low thermal conductivity of about 1.9 W/m-K at room temperature were obtained. The authors believed that a possible reason for this ultra-low thermal conductivity could be phonon coherence and zone folding that would lead to reduced phonon group velocity. It was argued that the holes played the role of Bragg reflectors, and thus phonons reflected from the successive sidewalls of the nanomeshes would interfere with each other, resulting in phononic band gaps in the dispersion relation, and hence lower phonon group velocity. Later, this phonon coherence picture was applied to explain the measured low thermal conductivities of other Si nanomeshes with various configurations.[270,271]

However, detailed analysis suggested that the conditions for phonon coherence to be predominant were very strict.[274] It was argued that interference between coherent phonons could occur only if (1) phonons scatter specularly off the pore sidewalls to keep their phase information and (2) no scattering occurs for phonons traveling between consecutive pore interfaces that can alter their frequency and phase information. For the first requirement, as there always exists a thin layer of native amorphous oxide (∼2 nm) on the surface of silicon, phonons traveling to the surfaces will mostly be diffusively scattered at room temperature, as is the case for Si NWs, making the quality of the nanomeshes unfavorable for phonon coherence. As for the second, in order to ensure low phonon−

DOI: 10.1021/acs.chemrev.8b00627
Chem. Rev. XXXX, XXX, XXX−XXX

phonon scattering rates, phonon MFP should be much larger than the characteristic length, and the number of populated phonon modes should be very small, which can both be realized only at low temperatures. Meanwhile, following the particle picture of phonons in the MC model with bulk properties modified by phonon-boundary scattering, the calculated in-plane thermal conductivity of Si nanomeshes agree well with the experimental results.[274] Therefore, it was concluded that it would still be valid to treat phonons as particles for thermal transport in nanomeshes with feature sizes greater than 100 nm.

Later, using MC simulations to solve the BTE, Ravichandran and Minnich[275] showed that, taking into account the surface amorphous layer of 3.5 nm thick, the simulation results purely based on a particle picture of phonons could match the experimental data reported by Yu et al.[219] However, the thickness of native oxide on the silicon surface is usually only ∼2 nm, significantly less than the 3.5 nm required to achieve a good fit. However, we note that the nanomeshes studied by Yu et al. have a large surface-area-to-volume ratio, in the regime where significant acoustic softening could occur, and as such, some additional reduction could be due to reduced Young's modulus and related phonon dispersion change and reduced phonon group velocity.

More recently, in order to elucidate the contribution from phonon coherence and phonon backscattering to the thermal conductivity reduction in Si nanomeshes, Lee et al. fabricated and measured thermal conductivity of Si nanomeshes with periodic and aperiodic pore arrangements.[268] As the surface-area-to-volume ratio of these two groups of the nanomeshes are kept the same to ensure the same boundary scattering effects, they could isolate the wave-related coherence effects by comparing the measured thermal conductivity of periodic and aperiodic nanomeshes. The fact that the measured thermal conductivity of these two nanomeshes are very close to each other (within 6% measurement uncertainty), and more importantly, the measured data can both be well-explained based on the MC ray-tracing simulation combined with BTE based on the phonon particle picture, led to the conclusion that phonon coherence is unimportant for thermal transport in Si nanomeshes with periodic length larger than 100 nm and at temperatures above 14 K, and phonon backscattering is the underlying mechanism for the thermal conductivity reduction.

In addition to Si nanomeshes with aligned holes, Tang et al. measured thermal conductivity of holey Si thin films with similar porous structure but with staggered holes,[272] which have zigzag solid path as in kinked NWs. Ultra-low thermal conductivity of ∼1.7 W/m-K was obtained at room temperature, which was attributed to the necking effect by the authors. As the neck length of the nanopores is smaller than the phonon MFP, compared with a straight NW, the phonons traveling in the holey silicon would experience more scattering by reflection from the nanohole sidewalls; therefore, they could be trapped and become non-propagating heat carriers. This explanation corresponds well with the understanding of phonon transport in kinked NWs. We note that based on the understanding of kinked NWs, it can be expected that even more remarkable thermal conductivity reduction should be feasible if the materials are of high elastic anisotropy, which has the potential to further enhance *ZT*.

Beyond the complex geometrical configurations, the effects of other morphological variations, such as core−shell and superlattice NWs, on thermal transport have also been explored. Most studies of core−shell NWs are carried out through modeling while a couple of experiments have also been done.[238,276−282] Yang et al. first presented their analysis of the thermal conductivity of Si core−Ge shell NWs based on solving the phonon Boltzmann equation and discussed the effects of the specularity parameter at the surface of the core and shell.[277] Using NEMD simulations, Hu et al. showed that a thin layer Ge shell of only 1−2 unit cells in thickness on a single-crystalline Si NW could lead to a surprisingly large reduction of up to 75% in the thermal conductivity at room temperature.[279,281] Through analyzing the phonon vibrational DOS, the authors attributed the reduction to the depression and localization of long-wavelength phonon modes at the Si/Ge interface and to the high-frequency non-propagating diffusive modes. In a separate study, it was demonstrated that the thermal conductivity variation with wire length for the core−shell NW was much weaker than that for pure NWs, and the thermal conductivity was almost independent of temperature in the wide region between 50 and 600 K.[279]

The results of Hu et al. could also be understood in a more straightforward way based on the classical size effect.[279,281] In MD simulations, the NW surface is rather smooth and specular phonon reflection leads to a thermal conductivity value significantly higher than that obtained in experiment where phonon scattering at the surface is nearly fully diffuse. Therefore, adding a layer of Ge, which has a rather significant lattice mismatch with Si, could introduce strong diffuse scattering at the interface and hence shorter phonon MFP and lower thermal conductivity. This simple picture, however, is not fully consistent with the results reported by Chen et al.[280,283] From their EMD simulation results, they found that unlike uniform Si, Ge, or SiGe alloy NWs, the heat current autocorrelation function for the Ge core and Si shell NW decayed much slower and maintained an oscillation pattern for a long time. They attributed this to the coupling and coherent resonance effect between the transverse and longitudinal phonon modes at the core−shell interface. A follow-up study by the same authors showed that introducing interface roughness by switching the Si and Ge atoms could further reduce the thermal conductivity of the NW with lower thermal conductivity as more atoms were switched, which was attributed to localization of higher-frequency phonons.[283]

Experimentally, Wingert et al. first measured the thermal conductivity of Ge core and Si shell NWs (Figure 17c).[238] Different from the reported significant thermal conductivity reduction of core−shell NWs from uniform composition NWs, the measured thermal conductivity of the core−shell NWs is comparable to the thermal conductivity of Ge NWs of similar diameter. However, the core−shell NW does demonstrate a very different temperature dependence, indicating interesting physics that are currently not well-understood. Another experimental study of core−shell NWs is composed of Bi core and Te shell.[282] NWs with both smooth and rough interfaces between the core and shell were prepared and it was found that the NWs with rough interface could have a thermal conductivity 2- to 5-fold lower than that of NWs with smooth interface. The mechanisms for this lower thermal conductivity could be similar to that of surface-rough Si NWs. The same group later performed measurement of *ZT* of these NWs and showed a rather high value of up to 0.5.[284]

As to superlattice NWs, actually experimental results on their thermal properties were first reported on Si/SiGe superlattice NWs.[22] However, due to the low Ge concentration

DOI: 10.1021/acs.chemrev.8b00627
Chem. Rev. XXXX, XXX, XXX−XXX

of <10% in the SiGe section and the large period length (100−150 nm), phonon scattering at the interfaces was deemed unimportant as compared to alloy and boundary scattering. No follow-up experimental studies have been done but several theoretical analyses and MD simulations have been carried out to explore the effects of the superlattice morphology on thermal transport in NWs. Dames and Chen[213] developed a theoretical model to calculate the thermal conductivity of superlattice NWs, and they predicted that compared to superlattice thin films, the additional sidewall scattering in superlattice nanowires could further reduce the thermal conductivity by a factor of 2 or more. MD simulations[285−287] in general confirmed that NW surfaces could pose additional resistance and some novel thermal properties of superlattice thin films due to phonon wave nature could also be observed. For example, Hu and Poulikakos showed the minimum thermal conductivity at certain periodic length as those observed for superlattice thin films.[286] However, it is worth noting that these results are based on perfect flat NW surfaces that specularly reflect phonons to a large extent. In reality, minor surface roughness or amorphous coating would destroy phonon coherence so its experimental realization could be very challenging, especially at room temperature.

4.2.5. Dimensional Crossover. In the literature, NWs are often referred to as "one-dimensional"; however, in most cases this designation is purely from a geometric consideration, but not in the physical sense since phonons with wave vectors along all directions are excited. As such, at what diameter true physical dimensionality transition occurs and the consequence of this transition on thermal conductivity is an interesting question. In fact, the divergent thermal conductivity of truly moment-conserved 1D system is a classical problem in physics.[288−290] This transition dimension could also set a theoretical limit of the minimum wire size suitable for thermoelectric applications as even smaller wires could have very high thermal conductivity.

Even though no solid experimental observation of thermal transport in truly physically 1D NWs has been reported, several MD simulations have shown enhanced thermal conductivity as the NW diameter reduces to the scale of a few nanometers.[291−293] For example, using NEMD simulations, Ponomareva et al. reported that as the Si NW diameter reduces from 7.7 to 3.4 nm, the thermal conductivity drops because of the surface scattering of phonons.[291] However, as the diameter further reduces, the thermal conductivity started to increases rapidly, reaching a value of ∼65 W/m·K as the diameter dropped to 1.46 nm.[291] Through examining the phonon spectral density, this enhancement trend at ultra-small diameter was attributed to a confinement induced shift to higher frequency of the lowest populated frequency modes, which could carry larger amount of energy. Donadio and Galli calculated the thermal conductivity of 1.1, 2, and 3 nm diameter Si NWs using EMD and their results suggested increasing thermal conductivity for smaller diameter wires.[292] They attributed this to more propagating phonon modes in smaller wires. More recently, Zhou et al. conducted a comprehensive EMD study of Si NWs using all Tersoff, environmental-dependent interatomic potential (EDIP), and Stillinger−Webber (SW) interatomic potentials.[293] Their data suggest that stable Si NWs only exits at certain smallest diameter and for NWs with diameters smaller than ∼2 nm, thermal conductivity increases rapidly with decreasing diameter and can reach a value that is more than 10-fold of the bulk value as the NW diameter becomes smaller than 1.0 nm. Detailed analysis shows that as the NW diameter drops below 2 nm, the phonon dispersion alters significantly with enlarged energy gaps between the acoustic and optical branches.[293] This leads to drastically lower *Umklapp* scattering rate and most scattering events are momentum-conserved normal scattering. However, the authors concluded that the residue *Umklapp* scattering would result in converged thermal conductivity.

While extensive theoretical analyses and numerical modeling have been done on thermal transport of physically 1D system, direct experimental observation of the thermal behavior during the dimensionality transition process is still lacking, and it will be extremely exciting to see direct experimental evidence of material thermal behavior during this process.

4.3. Summary

Motivated by the potential thermoelectric applications and the fundamental scientific interest, extensive studies on thermal transport through various kinds of NWs have been carried out in the past two decades, which has led to significant advance in our understanding of phonon dynamics at surfaces and interfaces and thermal transport through nanostructures. The dramatic thermal conductivity reduction in NWs is promising for enhanced *ZT*. While significant progress has been made, some underlying mechanisms, such as how surface roughness reduces lattice thermal conductivity, are still not fully understood, and combining various strategies in experiments to achieve a minimal thermal conductivity has not been well-explored yet.

5. INTEGRATION OF NANOWIRES FOR THERMOELECTRIC APPLICATIONS

As discussed above, NWs possess unique thermal and electrical properties that are promising for thermoelectric applications such as power generation and refrigeration. NW-based thermoelectric devices can take advantage of intrinsic small size of NWs and be manufactured at both single-NW and bulk scales with suitable manufacturing processes. In this section, we will describe various efforts to create NW-based thermoelectric devices.

Yang et al. attempted to experimentally study single Sb-doped ZnO nanobelts for thermoelectric nanogenerators.[294] The *ZT* of the nanobelts is found to be 0.13. Further, they demonstrated that the power output of the thermoelectric generator made out of the single nanobelt is ∼1.94 nW under a temperature difference of 30 K around room temperature. This power output can be employed for self-powered nanodevices. While this material is not a typical NW form, this work shows the potentials in that single nanostructures or NWs can be used to generate required power for nanoscale devices.

Often larger macroscale thermoelectric devices are required to generate meaningful power or to achieve significant cooling capacity. In such cases, NW arrays and NW composites are viable routes to achieve power output and to utilize large surface area. For NW arrays, common synthetic approaches could be either top-down or bottom-up. We first review the bottom-up approach for thermoelectric applications, followed by top-down approach.

One of the most well-known bottom-up approaches to manufacture NWs is the CVD method. CVD can produce high-quality NWs with single-crystalline quality. Numerous NWs including GaN,[295] ZnO,[296] Zn_3P_2,[297] SiC,[298] TiO_2,[299]

DOI: 10.1021/acs.chemrev.8b00627
Chem. Rev. XXXX, XXX, XXX−XXX

Ge,[300] etc. have been produced through various CVD methods.

Among various CVD methods, the VLS mechanism is particularly widely used to synthesize aligned NWs due to its simplicity. The VLS mechanism was introduced by Wagner et al.[14] and became a very powerful scheme to grow various semiconductor NWs with the superior quality. Various NW arrays have been successfully synthesized and some examples of NW arrays, GaN and Si are shown in Figure 19a,b.[16,301] Further, superlattice NWs have also been produced through the VLS mechanism, and Si/SiGe superlattice NWs are shown in Figure 19c,d.[20]

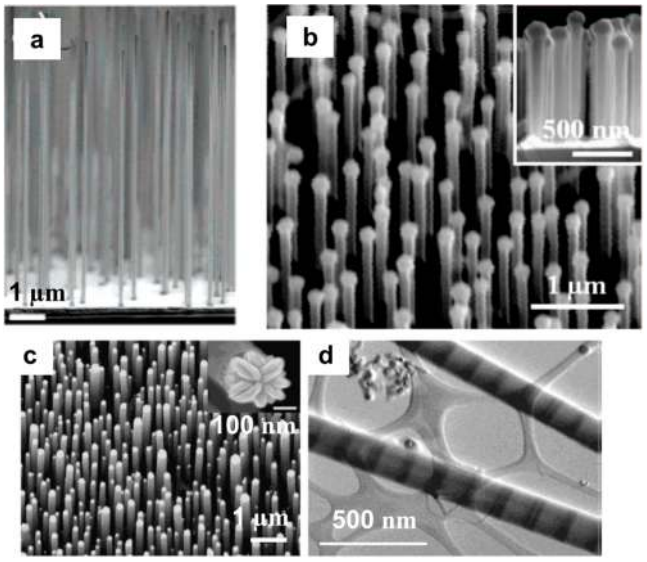

Figure 19. Various nanowire arrays grown by VLS mechanism. (a) SEM image of Si NW array. Reprinted with permission from ref 16. Copyright 2005 American Chemical Society. (b) SEM image of GaN NW array. Reprinted with permission from ref 301. Copyright 2008 American Chemical Society. (c) SEM image of Si/SiGe superlattice NW array, and (d) TEM image of Si/SiGe superlattice NWs. (c, d) Reprinted with permission from ref 20. Copyright 2002 American Chemical Society.

While detailed characterizations of thermoelectric properties have been investigated on numerous single NWs as discussed in the previous section, studies on integrating NW arrays into the thermoelectric devices have been limited despite its importance in technological advancements of several applications such as wireless sensor networks and wearable devices. Davila et al. demonstrated a prototype thermoelectric generator that integrates well-oriented Si NWs laterally grown by bottom-up CVD-VLS process into a device that is compatible with standard top-down silicon microfabrication processes, as shown in Figure 20.[302] The average diameter and length of the Si NWs are 100 nm and 10 μm, respectively. The resulting fabricated thermoelectric generator can generate power densities of 1.44 mW/cm^2 and 9 μW/cm^2 under temperature differences of 300 and 27 K, respectively. Follow-up study estimated that ZT of the Si NW arrays at ambient temperature ranges between 0.09 and 0.27.[303]

Further, Davila et al. proposed a thermoelectric generator integrating vertical CVD-VLS grown Si NW arrays, in contrast to the lateral Si NW arrays in previous studies.[304] They proposed p- and n-type Si NW arrays grown on two independent substrates and bond these two structures to

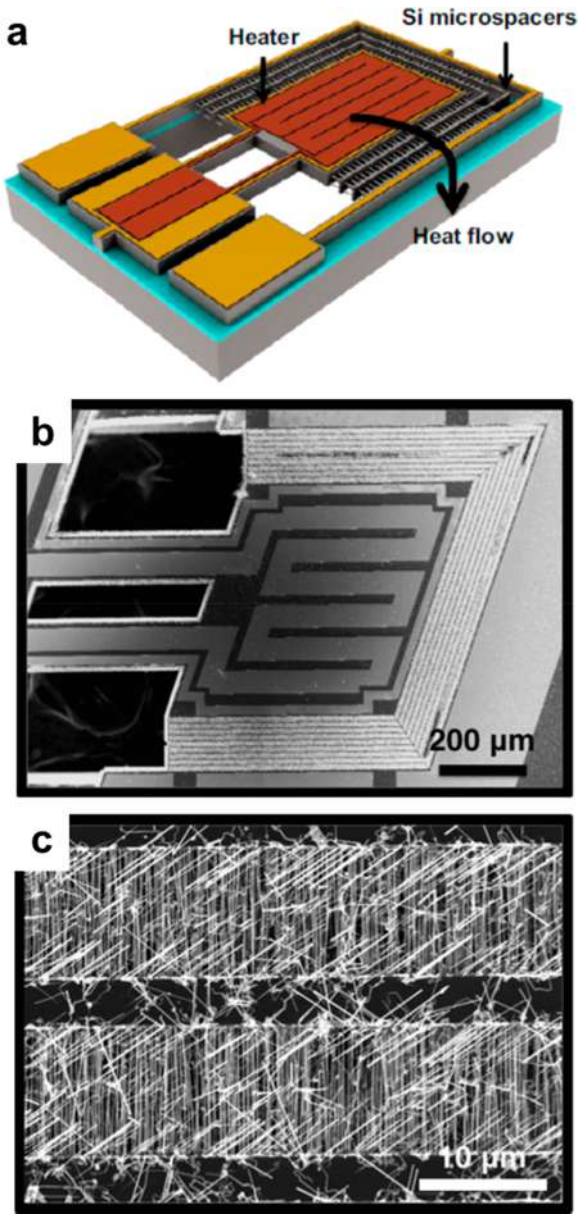

Figure 20. (a) Schematic of the thermoelectric generator that integrates CVD-VLS grown Si NWs into a device. (b) SEM image of a device with an integrated heater and silicon microspacers linking nine 10 μm long NW arrays. (c) Si NW arrays connected through Si microspacers. Reprinted with permission from ref 302. Copyright 2012 Elsevier.

complete the thermoelectric circuit, as shown in Figure 21. However, they only reported initial work on fabrication of the thermoelectric generator with vertical Si NW arrays. The characterization of the performance of the thermoelectric generator has not been reported. Vertically aligned thermoelectric generators would be advantageous over lateral/horizontal thermoelectric generators since temperature gradients can be readily applied by simply contacting a top plate with a large surface area on the heat source. Nonetheless, thermoelectric generators[302−304] proposed by Davila et al. is compatible with CMOS technology and uses abundant and inexpensive Si.

Abramson et al. proposed a thermoelectric device comprised of doped Si NW arrays embedded in a polymer matrix.[305]

DOI: 10.1021/acs.chemrev.8b00627
Chem. Rev. XXXX, XXX, XXX−XXX

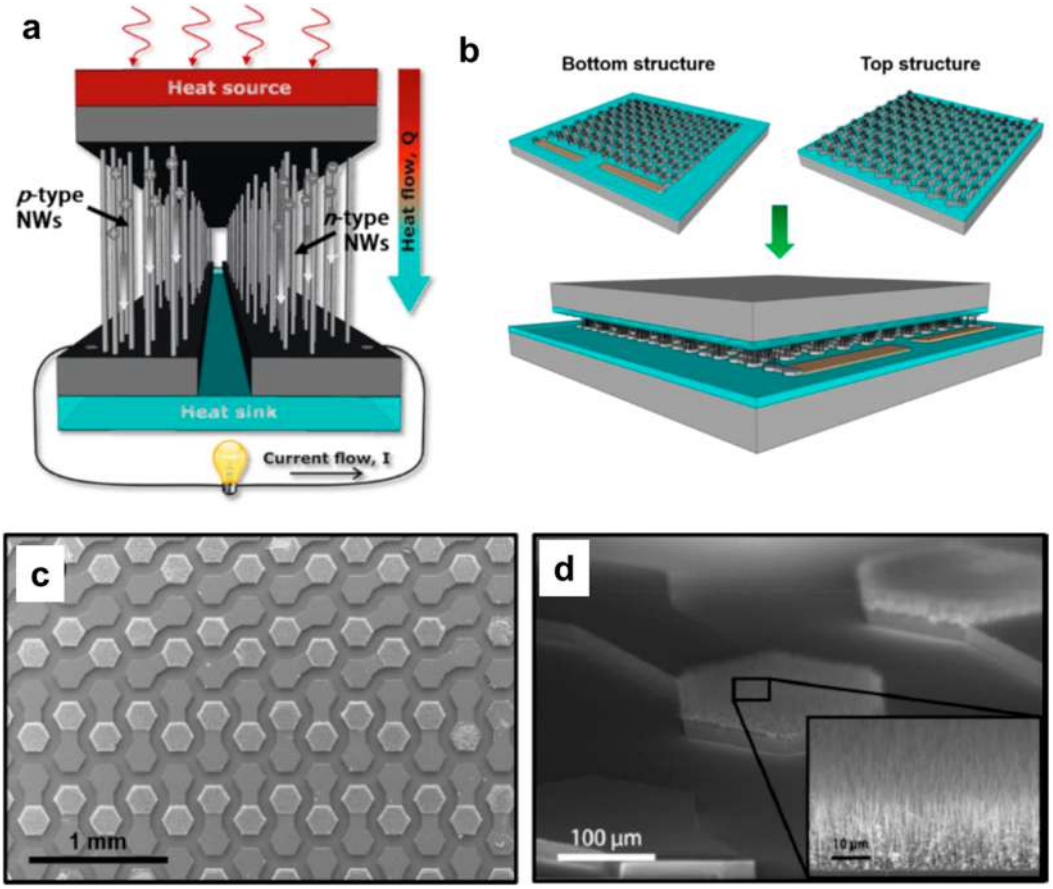

Figure 21. (a) Schematic of the thermoelectric generator integrating vertical Si NW arrays. (b) p- and n-type Si NW arrays are separately grown on two independent substrates and then two substrates are aligned to complete thermoelectric circuit. (c) SEM image of the hexagonal design of the thermoelectric elements. (d) Dense and aligned Si NW arrays grown on selected area of the substrate. Reprinted with permission from ref 304. Copyright 2015 Elsevier.

These Si NW arrays are synthesized by CVD-VLS method and subsequently doped by boron. Parylene polymer is deposited to conformally coat Si NW arrays and thus fills the gaps between NWs. The polymer matrix improves the structural stability, and the final structure is shown in Figure 22. They estimated the *ZT* at room temperature as $\sim 3.6 \times 10^{-4}$.

In addition to the bottom-up approaches reviewed above, top-down approaches have also been explored to synthesize NW arrays. Top-down fabrication usually starts with bulk materials such as silicon wafer or SOI wafer. Advanced lithographic techniques, such as electron beam lithography,[306] atomic force lithography,[307] optical lithography,[308,309] and nanoimprint lithography,[310] are used to transfer patterns onto substrates. Following lithography, etching or other fabrication processes are used to create NW arrays. Although a top-down approach involves more complicated and expensive microfabrication process compared to bottom-up approach, it can enable precise control of uniform dimension of NW arrays such as the diameter and length. Further, since standard microfabrication process is used, resultant devices after suitable fabrication processes can be completely functional devices with electrical contacts and also readily integrated with the existing integrated circuit technology and applications.

Li et al. demonstrated a thermoelectric generator with 5 mm × 5 mm in size based on top-down high-density Si NW arrays, which is capable of generating power output of 1.5 nW under 0.12 K temperature difference around room temperature.[311] These Si NW arrays are manufactured by deep ultraviolet lithography and plasma etching, and the resulting NWs after oxidation have dimensions with a diameter of ∼80 nm and a length of 1.2−1.5 μm (Figure 23). Subsequently, n- and p-type thermoelectric elements are prepared by selective ion implantation using a photoresist mask (Figure 23b). The pair of p- and n-type element is isolated (Figure 23c) and the bottom electrode is formed by selective silicidation process using Nickel (Figure 23d). Next, SiO_2 is deposited to fill the gaps between wires and top electrode is created by TaN/Al deposition (Figure 23e). The fabrication process involves multiple steps, but it is CMOS compatible and fully functional devices have been achieved through standard microfabrication process. The corresponding *ZT* value of the device is estimated to be 0.017.

Later, the same group improved the performance by replacing the filling material from SiO_2 to polyimide.[312] Polyimide reduces parasitic thermal conduction as well as the damage to the Si NWs. They report that a maximum power output of 0.47 μW under a temperature difference of 70 K across the experimental setup. The estimated *ZT* is 0.047, which is about three times larger than the previous device. In addition, a large temperature difference was accomplished with low thermal conductivity polyimide, resulting in a larger power output.

Curtin et al. reported thermoelectric performance of n-type Si NW arrays using a similar device architecture.[313] The Si NW

DOI: 10.1021/acs.chemrev.8b00627
Chem. Rev. XXXX, XXX, XXX−XXX

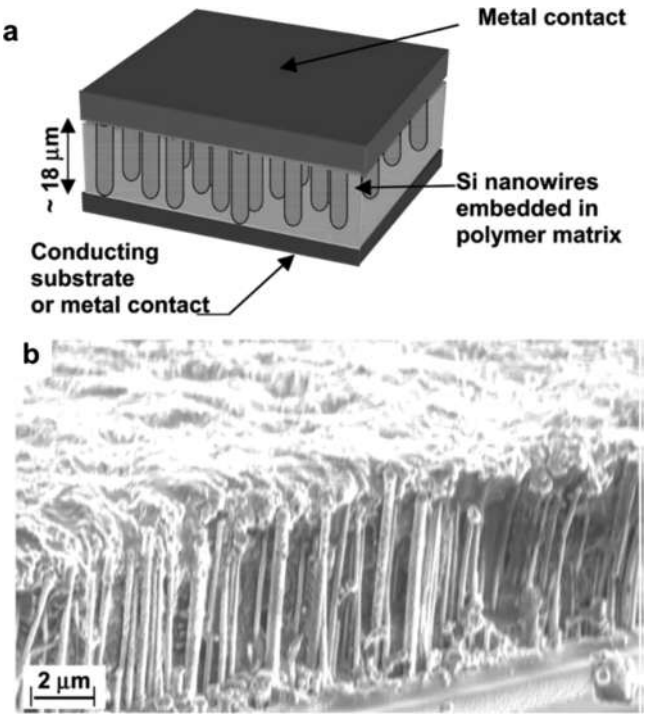

Figure 22. (a) Schematic of a proposed thermoelectric device component. (b) SEM side view of the composite with Si NW arrays and parylene matrix. Metal layer is deposited on top. Reprinted with permission from ref 305. Copyright 2004 IEEE.

arrays were created by interference lithography and a single-step deep reactive ion etch (DRIE). They used spin-on-glass (SOG) as a filling material due to its low thermal conductivity, electrical insulating properties, and high-temperature stability. The dimension of the Si NWs is ~85 nm in diameter and 1 μm in height. The maximum output power from the fabricated device with 50 μm × 50 μm cross-sectional size is measured to be 29.3 μW with a temperature difference of 56 K. Compared to the work performed by Li et al.,[312] the power output is greater due to the higher density of Si NW arrays.[314] However, this device only has n-type Si NW arrays and may require further integration of p-type NW arrays to complete the thermoelectric circuit.

Another route to synthesize NW arrays using top-down approach is the template assisted growth method.[315] A common base material is porous anodic alumina (PAA). Rabin et al. suggested one possible device architecture using the PAA template, as illustrated in Figure 24.[316] Briefly describing the process, Al is deposited on top of the pre-deposited substrate and a top surface is polished to minimize the surface roughness. Then, the aluminum layer is anodized, during which a self-organized and highly ordered array of pores are produced. Next, barrier oxide layer in close proximity to the substrate is selectively etched away, which gives high-density nanopore arrays. Various deposition techniques such as electrochemical deposition[317,318] and pressure injection method[319,320] are used to fill the pores to create NW arrays. If necessary, further patterning can be performed by etching NW arrays with an adequate mask. Similar to the proposed device architecture by Rabin et al., Keyani et al. fabricated n-type $Bi_{0.3}Sb_{0.7}$ NW arrays via the template assisted growth method using the porous anodized alumina.[321] They then demonstrated a thermoelectric device that is composed of n-type NW array element and a bulk p-type $Bi_{0.4}Sb_{1.6}Te_3$ element (Figure 25). The ZT of the hybrid device was estimated to be 0.12, comparable to the bulk $Bi_{0.3}Sb_{0.7}$ devices. The authors argued that despite the parasitic thermal conduction through the alumina template, the ZT of the hybrid device was maintained due to NW arrays with uniform NW lengths and a high areal density.

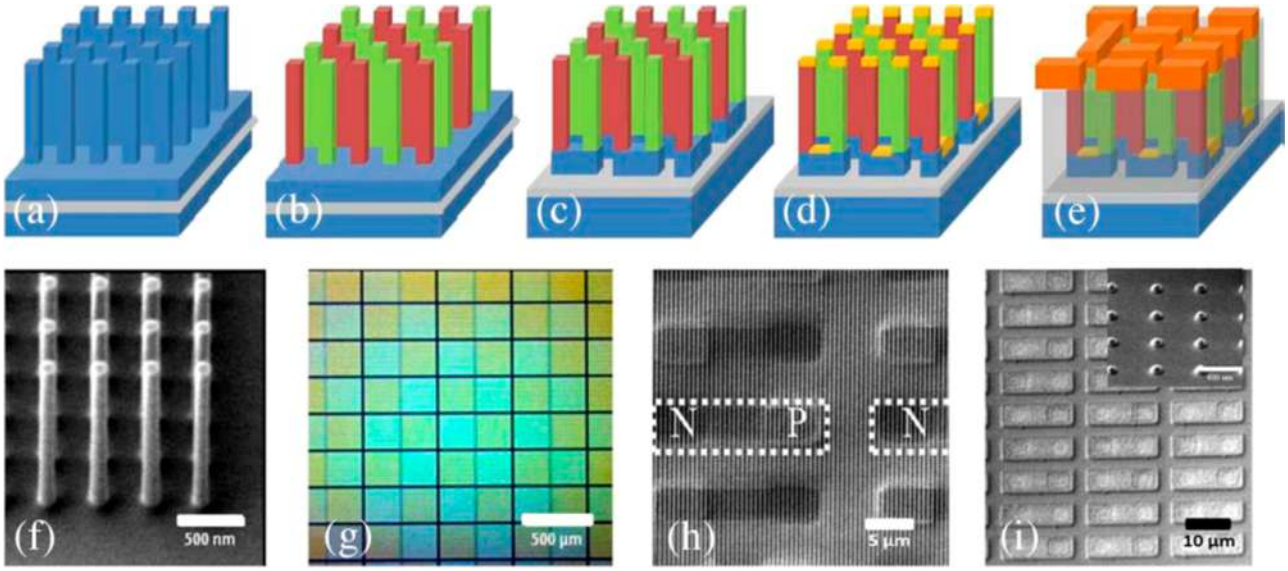

Figure 23. Schematic of the fabrication processes and images of device. (a) SiNW arrays by plasma etch. (b) Selective ion implantation to create p- and n-type thermoelectric device elements. Each element is composed of hundreds of Si NW. (c) A pair of p- and n-type component is separated by etching. (d) Silicidation is performed to create electrical connects. (e) SiO_2 is deposited to fill the gaps between NWs and subsequently top electrode is created by a metal deposition. (f) SEM images of Si NW arrays. (g) p- and n-type thermoelectric device elements are seen by a clear contrast under a microscope. (h) SEM images of p- and n-type Si NW arrays. (i) SEM image of several pairs of p- and n-type component. Inset shows the Si NWs exposed before the metal deposition to create the top electrode. Reprinted with permission from ref 311. Copyright 2011 IEEE.

DOI: 10.1021/acs.chemrev.8b00627
Chem. Rev. XXXX, XXX, XXX−XXX

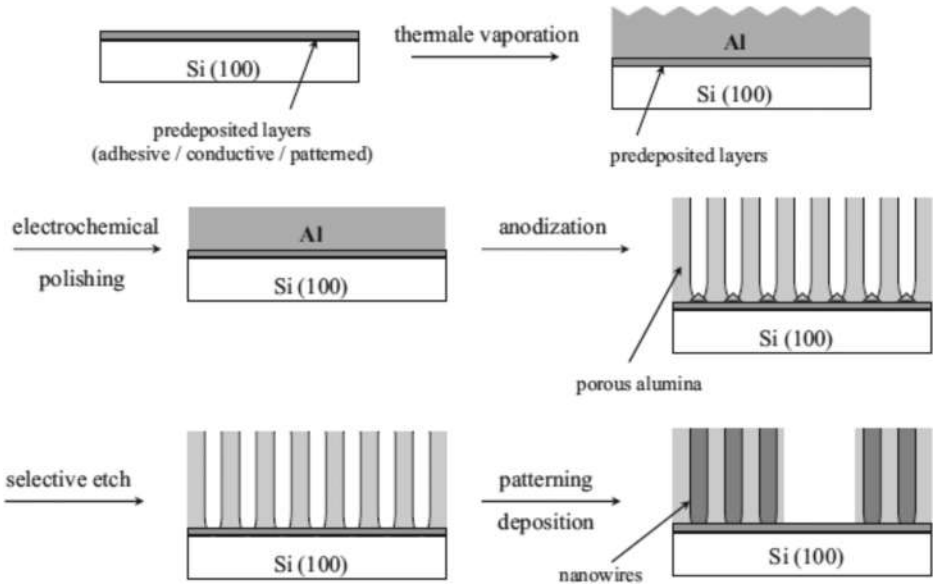

Figure 24. Schematic of the fabrication process of porous anodized alumina and NW arrays on the substrate. Reprinted with permission from ref 316. Copyright 2003 Wiley-VCH.

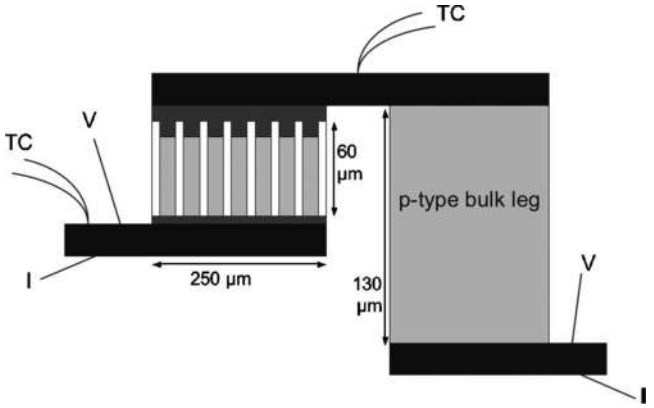

Figure 25. Schematic of the hybrid thermoelectric device composed of n-type $Bi_{0.3}Sb_{0.7}$ NW array and p-type bulk element. Reprinted with permission from ref 321. Copyright 2006 American Institute of Physics.

Metal-assisted chemical etching (MACE) method to synthesize large-area Si NW arrays is another powerful top-down approach since this method offers a simple process with good controllability.[322−325] The length and surface roughness of Si NWs can be tuned by varying the etching conditions and doping concentrations of silicon substrates.[258,326] Thermoelectric properties of the Si NWs synthesized via the metal-assisted chemical etching method were investigated and it was found that the thermal conductivity of these Si NWs was especially intriguing, with a value lower than that set by the Casimir limit.[33,247] Owing to the desirable low thermal conductivity, these Si NWs prepared by MACE have a great potential as excellent thermoelectric materials. It would be interesting to integrate these Si NW arrays into innovative thermoelectric device architectures including the ones described above.

In addition to traditional inorganic NWs described above, NW-based hybrid organic/inorganic composites recently have gained increasing attention due to low manufacturing cost from solution-processability and novel physical properties arising from organic/inorganic interface. See et al.[55] demonstrated the synthesis of inorganic Te NWs coated with a conducting polymer, poly(3,4-ethylendedioxythiophene):poly(styrenesulfonate) (PEDOT:PSS). The resultant hybrid film shows an electrical conductivity higher than either individual component, a Seebeck coefficient comparable to bulk Te, and a low thermal conductivity similar to the thermal conductivity of the polymer matrix. These desirable properties lead to a *ZT* value of 0.1, which is several orders of magnitude higher than

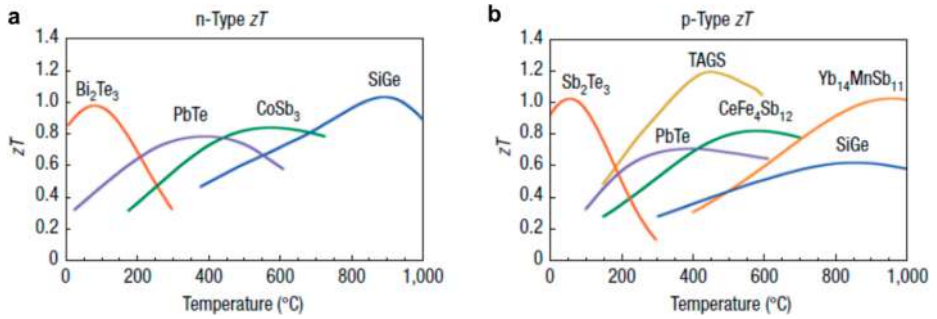

Figure 26. Figures of merit of various materials for (a) n-type and (b) p-type thermoelectric elements. Reprinted with permission from ref 19. Copyright 2008 Nature Publishing Group.

DOI: 10.1021/acs.chemrev.8b00627
Chem. Rev. XXXX, XXX, XXX−XXX

the ZT value of either PEDOT:PSS or Te NW. Follow-up work reveals that the conductive interface between the Te NW and the bulk PEDOT:PSS polymer is responsible for the unique thermoelectric properties.[327] Hybrid composites based on Te NW has been further investigated to engineering thermoelectric properties by optimizing the synthesis protocol and Te weight fraction.[328,329] Further, Sahu et al. showed that by chemically modifying the surfaces of inorganic Bi_2Te_3 NWs, both p- and n-type hybrid Bi_2Te_3/PEDOT:PSS materials can be constructed from one common base.[329] Intriguing interface effects have also been observed in tradition Si NW arrays. For example, Rasool et al. reported that the electrical conductivity of Si NW arrays could be enhanced by covering poly(acrylic acid) (PAA) polymer over Si NWs, and they attributed the electrical conductivity enhancement to the formation of acceptor-like states at NW/polymer interface.[330] In terms of the thermoelectric device performance, Zhou et al. demonstrated a flexible thermoelectric device based on the copper telluride NW and polyvinylidene fluoride (PVDF) polymer matrix with a power factor maintained at 23 $\mu W \cdot m^{-1} \cdot K^{-2}$ during 300 bending cycles, demonstrating a potential for wearable and bio-integrated thermoelectric devices.[331]

6. ADDITIONAL CONSIDERATIONS

The ZT of materials highly depends on the temperature, as clearly seen in Figure 26.[19] For example, ZT of n-type Bi_2Te_3, one of the materials that have been widely used in commercial thermoelectric modules, has a peak value of ~1 at slightly above 50 °C and rapidly decreases as temperature deviates from 50 °C. Other materials have peak ZT values at various temperatures ranging from room temperature to high temperatures close to 1000 °C. Further, some materials have relatively flatter ZT values than others over a wide temperature range, which is helpful for operation over large temperature difference. Therefore, specific thermoelectric materials have to be chosen depending on the desired operating temperature range. Moreover, positioning the peak value of ZT within the operating temperature regime is desirable when engineering thermoelectric properties of materials.

Considering the fact that the ultimate goal is to produce commercially viable thermoelectric devices using novel nanowire thermoelectric materials, both the performance and the cost of thermoelectric devices must be carefully examined. Although the ZT of some thermoelectric elements is low, lowering manufacturing cost for thermoelectric elements such as raw material costs and processing costs can be a promising route to reach the goal. One way to lower the costs is to reduce the processing cost. For conventional semiconductor materials, very expensive high-temperature and energy-intensive processes are required to prepare thermoelectric modules. Recently, more cost-effective synthesis methods such as solution process have been developed to synthesize novel thermoelectric nanomaterials.[332] Such novel synthesis methods can potentially decrease the cost further, finding a path to be utilized in commercially competitive thermoelectric devices. If the cost of synthesizing thermoelectric materials is high, high ZT needs to be achieved to be considered as attractive thermoelectric materials. Several studies applied cost analysis at the thermoelectric system level and showed that improving ZT at almost any cost is critical when legs' length and fill factor of the thermoelectric elements are minimized such that the cost of heat exchanger and heat spreading plates is dominant.[333−335]

Flexible and wearable thermoelectric devices have recently gained increasing attention due to their potentials as power sources for wearable and biointegrated devices.[332,336] Thermoelectric materials for such devices require flexibility, low-energy processing, and personal comfort such as lightweight and texture. For such devices, organic materials and hybrid inorganic/organic materials have been investigated and some interesting results have been reported.[337] For example, Kim et al. reported a maximum ZT value of 0.42 from DMSO-mixed PEDOT:PSS at room temperature through optimizing carrier concentrations.[338] Toward realization of flexible thermoelectric devices, several thermoelectric devices using hybrid composites have been fabricated. Choi et al. demonstrated flexible thermoelectric devices that are composed of reduced graphene oxide (rGO), PEDOT:PSS, and Te NWs and reported a maximum electrical power density of 650 nW/cm^2 at a temperature difference of 50 K.[339] Further, they demonstrated innovative thermoelectric generators based on all-carbon NT yarn without metal electrodes and 60 n- and p-type element pairs, which showed a maximum power density of 697 $\mu W/g$ at the temperature difference of 40 K.[340]

Over the past decade, significant efforts have been made to create efficient and inexpensive flexible thermoelectric materials. Developing innovative device architectures along with fundamental understanding of thermoelectric materials to engineering properties would be a key to manufacture commercially viable various kinds of thermoelectric devices.

Fundamental studies on NW thermoelectric properties have been focused either on individual NWs or NW composites. While both are critical, establishing relationship between individual NWs and composites made from those individual NWs is also important, since for certain scenarios where interface effects are dominant, conventional approaches such as effective medium theory are no longer valid. Better understanding of the relationship between NWs and composites could pave the road for a variety of routes to achieve better thermoelectric energy conversion.

7. SUMMARY AND OUTLOOK

Intensive studies over the past two and a half decades on the thermoelectrics of nanowires have led to breakthroughs in both fundamental understandings and device demonstration. Many early insightful ideas, such as significantly enhanced power factor due to quantum confinement and density of states engineering, as well as reduced thermal conductivity due to classical size effects, have been confirmed experimentally. Several unexpected scientific discoveries, especially on thermal transport through NWs, including the significant effects of acoustic softening, surface roughness, and complex morphology, have also been obtained. In general, all these effects point to the tremendous potential of NWs as thermoelectric materials. Because of the inherent challenges of working with NWs, the achievements obtained so far are really impressive and lay a solid foundation for revolutionizing thermoelectrics with NWs. Importantly, many insights collected from studying NWs have important implications beyond NWs and can be applied to structures such as nanomeshes.

Continued efforts must be made to break new grounds in this promising research field. Research should be carried out to pursue both fundamental understanding and high-performance engineering devices. Several potential routes to move forward are suggested as follows. (1) Additional studies need to be carried out to further understand the effects of several factors,

DOI: 10.1021/acs.chemrev.8b00627
Chem. Rev. XXXX, XXX, XXX−XXX

such as how surface roughness affects thermal transport in NWs, the limit of thermal conductivity reduction using kink morphology in elastically anisotropic materials, and how strain effects at the interface in core−shell NWs tune electrical and thermal transport. (2) New approaches based on the insights obtained so far should also be explored. For example, acoustic softening in NWs is attributed to the different atomic structure at the surface from the bulk. It would be interesting to probe whether it is possible to induce acoustic softening in core−shell NWs to further reduce the thermal conductivity. Also, with continued advancement in high-quality NW synthesis, it may now be possible to search for high power factor via narrow bandgap induced by semimetal−semiconductor transition or gapped topological insulator surface states. (3) To date, most studies have been focused on demonstrating the impact of one specific factor on the thermoelectric properties of NWs. With many effects conducive to higher ZT now demonstrated, it is time to integrate multiple factors to pursue highest possible ZT of NWs. For instance, it would be interesting to explore if heterostructured core−shell NWs can possess both high power factor owning to the enhanced mobility and low thermal conductivity via acoustic softening. It would be also valuable to revisit and explore the limits of thermoelectric properties of rough and thin Si NWs as now we are armed with better understandings and experimental capabilities achieved over the past decade. (4) Novel device integration approach to fabricate NW-based thermoelectric devices with high performance at low costs is always a key for real impacts of thermoelectric NWs. NW-based thermoelectric devices could be particularly promising to be integrated with tiny sensors and actuators being used in an environment with sustained temperature difference and only demanding low power to run.

Overall, built upon the tremendous progress achieved in the past two and a half decades, we are armed with unprecedented knowledge and capabilities to pursue the thermoelectrics of NWs, and new breakthroughs in the coming years should allow us to further understand thermoelectric transport in NWs and to construct NW-based high-performance thermoelectric devices.

AUTHOR INFORMATION

Corresponding Author

*E-mail: deyu.li@vanderbilt.edu.

ORCID

Renkun Chen: 0000-0001-7526-4981
Deyu Li: 0000-0001-8364-0924

Notes

The authors declare no competing financial interest.

Biographies

Renkun Chen is an Associate Professor of Mechanical Engineering and Materials Science at the University of California, San Diego. He received a B.S. degree in Thermo-physics at Tsinghua University, Beijing, in 2004, and a Ph.D. degree in Mechanical Engineering from the University of California, Berkeley, in 2008. He was a postdoctoral researcher at Berkeley prior to joining UCSD in 2009. Advised by Prof. Arun Majumdar and in collaboration with Prof. Peidong Yang, he studied thermoelectricity and thermal transport in Si nanowires during his doctoral and postdoctoral work. His research group at UCSD is generally interested in fundamentals and applications of thermal energy transport and conversion, including nanoscale energy transport phenomena, thermoelectric and solar-thermal energy conversion, phase change heat transfer, and thermal insulation technologies.

Jaeho Lee is an Assistant Professor of Mechanical and Aerospace Engineering at University of California, Irvine, with a joint appointment in Materials Science and Chemical Engineering. He received a B.S. degree in Mechanical Engineering from Georgia Institute of Technology in 2007 with highest honors, and M.S. and Ph.D. degrees in Mechanical Engineering with a minor in Electrical Engineering from Stanford University in 2012. His dissertation focused on nanoscale thermal phenomena in electronic devices and phase-change materials, studying with Prof. Ken Goodson. Prior to joining UC Irvine in 2015, he worked as a postdoctoral scholar in the Materials Sciences Division at Lawrence Berkeley National Laboratory with Prof. Peidong Yang. He worked as a summer faculty fellow at the Jet Propulsion Laboratory in 2016. He is a recipient of the Hellman Faculty Fellowship. His research interests lie at the intersection of heat transfer and materials science, targeting novel devices in the areas of thermal management, thermoelectrics, and phononics.

Woochul Lee is currently an Assistant Professor in the Department of Mechanical Engineering at the University of Hawaii at Manoa. He received his B.S. degree in Mechanical Engineering from Yonsei University, Korea, in 2008. He then joined Prof. Pramod Reddy's lab and received his M.S. and Ph.D. degrees in Mechanical Engineering at the University of Michigan, Ann Arbor, in 2010 and 2014, respectively. He did postdoctoral studies with Prof. Peidong Yang and Dr. Jeffrey J. Urban at UC Berkeley and Lawrence Berkeley National Laboratory. His research interests include fundamental understanding of nanoscale energy transport and conversion, and thermal management.

Deyu Li is currently a professor in the Department of Mechanical Engineering at Vanderbilt University. He received his B.S., M.S., and Ph.D. degrees from the University of Science and Technology of China, Tsinghua University, and the University of California, Berkeley, respectively. Prof. Li's research interests include nanoscale energy transport as well as microfluidics and nanofluidics, and he has published over 80 peer-reviewed journal papers.

ACKNOWLEDGMENTS

The authors thank Lin Yang and Zhiliang Pan for help in putting together some of the figures and references. R.C. acknowledges financial support for his work on nanoscale thermoelectric transport from the National Science Foundation (CBET-1140121, CBET-1336428, DMR-1508420, and CMMI-1762560), a Hellman Faculty Award, and an ACS-PRF grant (54109-ND10). J.L. acknowledges financial support from the National Science Foundation (ECCS-1807825) and the Henry Samueli School of Engineering, the University of California at Irvine. W.L. acknowledges support from the College of Engineering, University of Hawaii at Manoa. D.L. acknowledges financial support for his work on nanoscale thermal transport from the National Science Foundation (CMMI-0800306, CBET-1067213, DMR-1308550, CBET-1403456, CMMI-1462866, DMR-1532107, and CBET-1805924), as well as support from the Lockheed Martin Corporation.

DOI: 10.1021/acs.chemrev.8b00627
Chem. Rev. XXXX, XXX, XXX−XXX

REFERENCES

(1) Hicks, L. D.; Dresselhaus, M. S. Effect of Quantum-Well Structures on the Thermoelectric Figure of Merit. *Phys. Rev. B: Condens. Matter Mater. Phys.* **1993**, *47*, 12727−12731.

(2) Majumdar, A. Thermoelectricity in Semiconductor Nanostructures. *Science* **2004**, *303*, 777−778.

(3) Heremans, J. P.; Dresselhaus, M. S.; Bell, L. E.; Morelli, D. T. When Thermoelectrics Reached the Nanoscale. *Nat. Nanotechnol.* **2013**, *8*, 471−473.

(4) Rurali, R. *Colloquium*: Structural, Electronic, and Transport Properties of Silicon Nanowires. *Rev. Mod. Phys.* **2010**, *82*, 427−449.

(5) Benenti, G.; Casati, G.; Saito, K.; Whitney, R. S. Fundamental Aspects of Steady-State Conversion of Heat to Work at the Nanoscale. *Phys. Rep.* **2017**, *694*, 1−124.

(6) Swinkels, M. Y.; Zardo, I. Nanowires for Heat Conversion. *J. Phys. D: Appl. Phys.* **2018**, *51*, 353001.

(7) Nolas, G. S.; Sharp, J.; Goldsmid, H. J. *Thermoelectrics - Basic Principles and New Materials Developments*. Springer: Berlin, 2001; p 2−5.

(8) Goupil, C.; Seifert, W.; Zabrocki, K.; Müller, E.; Snyder, G J. Thermodynamics of Thermoelectric Phenomena and Applications. *Entropy* **2011**, *13*, 1481−1517.

(9) Xia, B. Y.; Yang, P.; Sun, Y.; Wu, Y.; Mayers, B.; Gates, B.; Yin, Y.; Kim, F.; Yan, H. One-Dimensional Nanostructures: Synthesis, Characterization, and Applications. *Adv. Mater.* **2003**, *15*, 353−389.

(10) Hochbaum, A. I.; Yang, P. Semiconductor Nanowires for Energy Conversion. *Chem. Rev.* **2010**, *110*, 527−546.

(11) Hobbs, R. G.; Petkov, N.; Holmes, J. D. Semiconductor Nanowire Fabrication by Bottom-Up and Top-Down Paradigms. *Chem. Mater.* **2012**, *24*, 1975−1991.

(12) Wang, N.; Cai, Y.; Zhang, R. Q. Growth of Nanowires. *Mater. Sci. Eng., R* **2008**, *60*, 1−51.

(13) Dasgupta, N. P.; Sun, J.; Liu, C.; Brittman, S.; Andrews, S. C.; Lim, J.; Gao, H.; Yan, R.; Yang, P. 25th Anniversary Article: Semiconductor Nanowires - Synthesis, Characterization, and Applications. *Adv. Mater.* **2014**, *26*, 2137−2184.

(14) Wagner, R. S.; Ellis, W. C. Vapor-Liquid-Solid Mechanism of Single Crystal Growth. *Appl. Phys. Lett.* **1964**, *4*, 89−90.

(15) Wu, Y.; Yang, P. Direct Observation of Vapor-Liquid-Solid Nanowire Growth. *J. Am. Chem. Soc.* **2001**, *123*, 3165−3166.

(16) Hochbaum, A. I.; Fan, R.; He, R.; Yang, P. Controlled Growth of Si Nanowire Arrays for Device Integration. *Nano Lett.* **2005**, *5*, 457−460.

(17) Li, D.; Wu, Y.; Kim, P.; Shi, L.; Yang, P.; Majumdar, A. Thermal Conductivity of Individual Silicon Nanowires. *Appl. Phys. Lett.* **2003**, *83*, 2934.

(18) Lu, W.; Xiang, J.; Timko, B. P.; Wu, Y.; Lieber, C. M. One-Dimensional Hole Gas in Germanium/Silicon Nanowire Heterostructures. *Proc. Natl. Acad. Sci. U. S. A.* **2005**, *102*, 10046−10051.

(19) Snyder, G. J.; Toberer, E. S. Complex Thermoelectric Materials. *Nat. Mater.* **2008**, *7*, 105−114.

(20) Wu, Y.; Fan, R.; Yang, P. Block-by-Block Growth of Single-Crystalline Si/SiGe Superlattice Nanowires. *Nano Lett.* **2002**, *2*, 83−86.

(21) Kim, H.; Kim, I.; Choi, H. J.; Kim, W. Thermal Conductivities of $Si_{1-x}Ge_x$ Nanowires with Different Germanium Concentrations and Diameters. *Appl. Phys. Lett.* **2010**, *96*, 233106.

(22) Li, D.; Wu, Y.; Fan, R.; Yang, P.; Majumdar, A. Thermal Conductivity of Si/SiGe Superlattice Nanowires. *Appl. Phys. Lett.* **2003**, *83*, 3186−3188.

(23) Tian, B.; Xie, P.; Kempa, T. J.; Bell, D. C.; Lieber, C. M. Single-Crystalline Kinked Semiconductor Nanowire Superstructures. *Nat. Nanotechnol.* **2009**, *4*, 824−829.

(24) Jiang, J. W.; Yang, N.; Wang, B. S.; Rabczuk, T. Modulation of Thermal Conductivity in Kinked Silicon Nanowires: Phonon Interchanging and Pinching Effects. *Nano Lett.* **2013**, *13*, 1670−1674.

(25) Wang, F.; Yu, H.; Jeong, S.; Pietryga, J. M.; Hollingsworth, K. J. A.; Gibbons, P. C.; Buhro, W. E. The Scaling of the Effective Band Gaps in Indium Arsenide Quantum Dots and Wires. *ACS Nano* **2008**, *2*, 1903−1913.

(26) Tian, Y.; Sakr, M. R.; Kinder, J. M.; Liang, D.; MacDonald, M. J.; Qiu, R. L. J.; Gao, H. J.; Gao, X. P. A. One-Dimensional Quantum Confinement Effect Modulated Thermoelectric Properties in InAs Nanowires. *Nano Lett.* **2012**, *12*, 6492−6497.

(27) Liang, W.; Rabin, O.; Hochbaum, A. I.; Fardy, M.; Zhang, M.; Yang, P. Thermoelectric Properties of p-Type PbSe Nanowires. *Nano Res.* **2009**, *2*, 394−399.

(28) Zhang, G.; Kirk, B.; Jauregui, L. a.; Yang, H.; Xu, X.; Chen, Y. P.; Wu, Y. Rational Synthesis of Ultrathin n-Type Bi_2Te_3 Nanowires with Enhanced Thermoelectric Properties. *Nano Lett.* **2012**, *12*, 56−60.

(29) Finefrock, S. W.; Zhang, G.; Bahk, J. H.; Fang, H.; Yang, H.; Shakouri, A.; Wu, Y. Structure and Thermoelectric Properties of Spark Plasma Sintered Ultrathin PbTe Nanowires. *Nano Lett.* **2014**, *14*, 3466−3473.

(30) Yang, H.; Bahk, J. H.; Day, T.; Mohammed, A. M. S.; Snyder, G. J.; Shakouri, A.; Wu, Y. Enhanced Thermoelectric Properties in Bulk Nanowire Heterostructure-Based Nanocomposites through Minority Carrier Blocking. *Nano Lett.* **2015**, *15*, 1349−1355.

(31) Zhou, J.; Jin, C.; Seol, J. H.; Li, X.; Shi, L. Thermoelectric Properties of Individual Electrodeposited Bismuth Telluride Nanowires. *Appl. Phys. Lett.* **2005**, *87*, 133109.

(32) Li, L.; Xu, S.; Li, G. Enhancement of Thermoelectric Properties in Bi-Sb-Te Alloy Nanowires by Pulsed Electrodeposition. *Energy Technol.* **2015**, *3*, 825−829.

(33) Hochbaum, A. I.; Chen, R.; Delgado, R. D.; Liang, W.; Garnett, E. C.; Najarian, M.; Majumdar, A.; Yang, P. Enhanced Thermoelectric Performance of Rough Silicon Nanowires. *Nature* **2008**, *451*, 163−167.

(34) Melosh, N. A.; Boukai, A.; Diana, F.; Gerardot, B.; Badolato, A.; Petroff, P. M.; Heath, J. R. Ultrahigh-Density Nanowire Lattices and Circuits. *Science* **2003**, *300*, 112−115.

(35) Xu, B.; Khouri, W.; Fobelets, K. Two-Sided Silicon Nanowire Array/Bulk Thermoelectric Power Generator. *IEEE Electron Device Lett.* **2014**, *35*, 596−598.

(36) Zhang, T.; Wu, S.; Xu, J.; Zheng, R.; Cheng, G. High Thermoelectric Figure-of-Merits from Large-Area Porous Silicon Nanowire Arrays. *Nano Energy* **2015**, *13*, 433−441.

(37) Shi, L.; Li, D.; Yu, C.; Jang, W.; Kim, D.; Yao, Z.; Kim, P.; Majumdar, A. Measuring Thermal and Thermoelectric Properties of One-Dimensional Nanostructures Using a Microfabricated Device. *J. Heat Transfer* **2003**, *125*, 881.

(38) Zhou, F.; Szczech, J.; Pettes, M. T.; Moore, A. L.; Jin, S.; Shi, L. Determination of Transport Properties in Chromium Disilicide Nanowires via Combined Thermoelectric and Structural Characterizations. *Nano Lett.* **2007**, *7*, 1649−1654.

(39) Boukai, A. I.; Bunimovich, Y.; Tahir-Kheli, J.; Yu, J.-K.; Goddard, W. A.; Heath, J. R. Silicon Nanowires as Efficient Thermoelectric Materials. *Nature* **2008**, *451*, 168−171.

(40) Lee, J.; Lee, W.; Lim, J.; Yu, Y.; Kong, Q.; Urban, J. J.; Yang, P. Thermal Transport in Silicon Nanowires at High Temperature up to 700 K. *Nano Lett.* **2016**, *16*, 4133−4140.

(41) Martin, P.; Aksamija, Z.; Pop, E.; Ravaioli, U. Impact of Phonon-Surface Roughness Scattering on Thermal Conductivity of Thin Si Nanowires. *Phys. Rev. Lett.* **2009**, *102*, 125503.

(42) Lim, J.; Hippalgaonkar, K.; Andrews, S. C.; Majumdar, A.; Yang, P. Quantifying Surface Roughness Effects on Phonon Transport in Silicon Nanowires. *Nano Lett.* **2012**, *12*, 2475−2482.

(43) Lee, E. K.; Yin, L.; Lee, Y.; Lee, J. W.; Lee, S. J.; Lee, J.; Cha, S. N.; Whang, D.; Hwang, G. S.; Hippalgaonkar, K.; et al. Large Thermoelectric Figure-of-Merits from SiGe Nanowires by Simultaneously Measuring Electrical and Thermal Transport Properties. *Nano Lett.* **2012**, *12*, 2918−2923.

(44) Chen, C. L.; Chen, Y. Y.; Lin, S. J.; Ho, J. C.; Lee, P. C.; Chen, C. D.; Harutyunyan, S. R. Fabrication and Characterization of Electrodeposited Bismuth Telluride Films and Nanowires. *J. Phys. Chem. C* **2010**, *114*, 3385−3389.

DOI: 10.1021/acs.chemrev.8b00627
Chem. Rev. XXXX, XXX, XXX−XXX

(45) Shin, H. S.; Jeon, S. G.; Yu, J.; Kim, Y. S.; Park, H. M.; Song, J. Y. Twin-Driven Thermoelectric Figure-of-Merit Enhancement of Bi_2Te_3 Nanowires. *Nanoscale* **2014**, *6*, 6158−6165.
(46) Zhou, F.; Moore, A. L.; Pettes, M. T.; Lee, Y.; Seol, J. H.; Ye, Q. L.; Rabenberg, L.; Shi, L. Effect of Growth Base Pressure on the Thermoelectric Properties of Indium Antimonide Nanowires. *J. Phys. D: Appl. Phys.* **2010**, *43*, 025406.
(47) Lee, S. H.; Shim, W.; Jang, S. Y.; Roh, J. W.; Kim, P.; Park, J.; Lee, W. Thermoelectric Properties of Individual Single-Crystalline PbTe Nanowires Grown by a Vapor Transport Method. *Nanotechnology* **2011**, *22*, 295707.
(48) Yazji, S.; Swinkels, M. Y.; De Luca, M.; Hoffmann, E. A.; Ercolani, D.; Roddaro, S.; Abstreiter, G.; Sorba, L.; Bakkers, E. P. A. M.; Zardo, I. Assessing the Thermoelectric Properties of Single InSb Nanowires: The Role of Thermal Contact Resistance. *Semicond. Sci. Technol.* **2016**, *31*, 064001.
(49) Lee, W.; Li, H.; Wong, A. B.; Zhang, D.; Lai, M.; Yu, Y.; Kong, Q.; Lin, E.; Urban, J. J.; Grossman, J. C.; Yang, P. Ultralow Thermal Conductivity in All-Inorganic Halide Perovskites. *Proc. Natl. Acad. Sci. U. S. A.* **2017**, *114*, 8693−8697.
(50) Li, Z.; Xu, E.; Losovyj, Y.; Li, N.; Chen, A.; Swartzentruber, B.; Sinitsyn, N.; Yoo, J.; Jia, Q.; Zhang, S. Surface Oxidation and Thermoelectric Properties of Indium-Doped Tin Telluride Nanowires. *Nanoscale* **2017**, *9*, 13014−13024.
(51) Kim, J.; Oh, M. W.; Kim, G.; Bahk, J. H.; Song, J. Y.; Jeon, S. G.; Chun, D. W.; Bae, J. H.; Shim, W.; Lee, W. Strain-Engineered Allotrope-like Bismuth Nanowires for Enhanced Thermoelectric Performance. *Acta Mater.* **2018**, *144*, 145−153.
(52) Hernandez, J. A.; Ruiz, A.; Fonseca, L. F.; Pettes, M. T.; Jose-Yacaman, M.; Benitez, A. Thermoelectric Properties of SnSe Nanowires with Different Diameters. *Sci. Rep.* **2018**, *8*, 11966.
(53) Andrews, S. C.; Fardy, M. a.; Moore, M. C.; Aloni, S.; Zhang, M.; Radmilovic, V.; Yang, P. Atomic-Level Control of the Thermoelectric Properties in Polytypoid Nanowires. *Chem. Sci.* **2011**, *2*, 706.
(54) Zhang, G.; Wang, W.; Li, X. Enhanced Thermoelectric Properties of Core/Shell Heterostructure Nanowire Composites. *Adv. Mater.* **2008**, *20*, 3654−3656.
(55) See, K. C.; Feser, J. P.; Chen, C. E.; Majumdar, A.; Urban, J. J.; Segalman, R. A. Water-Processable Polymer-Nanocrystal Hybrids for Thermoelectrics. *Nano Lett.* **2010**, *10*, 4664−4667.
(56) Liu, Y. B.; Zhou, S. M.; Yuan, X. Y.; Lou, S. Y.; Gao, T.; Shi, X. J.; Wu, X. P. Synthesis and High-Performance Thermoelectric Properties of Beta-Zn_4Sb_3 Nanowires. *Mater. Lett.* **2012**, *84*, 116−119.
(57) Zhang, G.; Fang, H.; Yang, H.; Jauregui, L. A.; Chen, Y. P.; Wu, Y. Design Principle of Telluride-Based Nanowire Heterostructures for Potential Thermoelectric Applications. *Nano Lett.* **2012**, *12*, 3627−3633.
(58) Fang, H.; Yang, H.; Wu, Y. Thermoelectric Properties of Silver Telluride-Bismuth Telluride Nanowire Heterostructure Synthesized by Site-Selective Conversion. *Chem. Mater.* **2014**, *26*, 3322−3327.
(59) Wang, Y.; Fan, H. J. Improved Thermoelectric Properties of $La_{1-X}Sr_xCoO_3$ Nanowires. *J. Phys. Chem. C* **2010**, *114*, 13947−13953.
(60) Tan, M.; Deng, Y.; Wang, Y. Ordered Structure and High Thermoelectric Properties of $Bi_2(Te,Se)_3$ nanowire Array. *Nano Energy* **2014**, *3*, 144−151.
(61) Ju, H.; Kim, M.; Kim, J. A Facile Fabrication of N-Type Bi_2Te_3 Nanowire/Graphene Layer-by-Layer Hybrid Structures and Their Improved Thermoelectric Performance. *Chem. Eng. J.* **2015**, *275*, 102−112.
(62) Zhou, C.; Dun, C.; Wang, K.; Zhang, X.; Shi, Z.; Liu, G.; Hewitt, C. A.; Qiao, G.; Carroll, D. L. General Method of Synthesis Ultrathin Ternary Metal Chalcogenide Nanowires for Potential Thermoelectric Applications. *Nano Energy* **2016**, *30*, 709−716.
(63) Ko, T. Y.; Shellaiah, M.; Sun, K. W. Thermal and Thermoelectric Transport in Highly Resistive Single Sb_2Se_3 Nanowires and Nanowire Bundles. *Sci. Rep.* **2016**, *6*, 35086.
(64) Fang, H.; Bahk, J. H.; Feng, T.; Cheng, Z.; Mohammed, A. M. S.; Wang, X.; Ruan, X.; Shakouri, A.; Wu, Y. Thermoelectric Properties of Solution-Synthesized n-Type Bi_2Te_3 Nanocomposites Modulated by Se: An Experimental and Theoretical Study. *Nano Res.* **2016**, *9*, 117−127.
(65) Zhou, C.; Shi, Z.; Ge, B.; Wang, K.; Zhang, D.; Liu, G.; Qiao, G. Scalable Solution-Based Synthesis of Component-Controllable Ultrathin $PbTe_{1-x}Se_x$ Nanowires with High n-Type Thermoelectric Performance. *J. Mater. Chem. A* **2017**, *5*, 2876−2884.
(66) Tan, M.; Hao, Y.; Deng, Y.; Chen, J. High Thermoelectric Properties of $(Sb, Bi)_2Te_3$ Nanowire Arrays by Tilt-Structure Engineering. *Appl. Surf. Sci.* **2018**, *443*, 11−17.
(67) Cornett, J. E.; Rabin, O. Effect of the Energy Dependence of the Carrier Scattering Time on the Thermoelectric Power Factor of Quantum Wells and Nanowires. *Appl. Phys. Lett.* **2012**, *100*, 242106.
(68) Hicks, L. D.; Dresselhaus, M. S. Thermoelectric Figure of Merit of a One-Dimensional Conductor. *Phys. Rev. B: Condens. Matter Mater. Phys.* **1993**, *47*, 16631−16634.
(69) Pei, Y.; LaLonde, A. D.; Wang, H.; Snyder, G. J. Low Effective Mass Leading to High Thermoelectric Performance. *Energy Environ. Sci.* **2012**, *5*, 7963.
(70) Mahan, G. D.; Sofo, J. O. The Best Thermoelectric. *Proc. Natl. Acad. Sci. U. S. A.* **1996**, *93*, 7436−7439.
(71) Heremans, J. P.; Jovovic, V.; Toberer, E. S.; Saramat, A.; Kurosaki, K.; Charoenphakdee, A.; Yamanaka, S.; Snyder, G. J. Enhancement of Thermoelectric Efficiency in PbTe by Distortion of the Electronic Density of States. *Science* **2008**, *321*, 554−557.
(72) Zhang, Q.; Liao, B.; Lan, Y.; Lukas, K.; Liu, W.; Esfarjani, K.; Opeil, C.; Broido, D.; Chen, G.; Ren, Z. High Thermoelectric Performance by Resonant Dopant Indium in Nanostructured SnTe. *Proc. Natl. Acad. Sci. U. S. A.* **2013**, *110*, 13261−13266.
(73) Heremans, J. P.; Wiendlocha, B.; Chamoire, A. M. Resonant Levels in Bulk Thermoelectric Semiconductors. *Energy Environ. Sci.* **2012**, *5*, 5510−5530.
(74) Nakpathomkun, N.; Xu, H. Q.; Linke, H. Thermoelectric Efficiency at Maximum Power in Low-Dimensional Systems. *Phys. Rev. B: Condens. Matter Mater. Phys.* **2010**, *82*, 235428.
(75) Van Wees, B. J.; Van Houten, H.; Beenakker, C. W. J.; Williamson, J. G.; Kouwenhoven, L. P.; Van Der Marel, D.; Foxon, C. T. Quantized Conductance of Point Contacts in a Two-Dimensional Electron Gas. *Phys. Rev. Lett.* **1988**, *60*, 848−850.
(76) Kaufman, D.; Berk, Y.; Dwir, B.; Rudra, A.; Palevski, A.; Kapon, E. Conductance Quantization in V-Groove Quantum Wires. *Phys. Rev. B: Condens. Matter Mater. Phys.* **1999**, *59*, R10433−R10436.
(77) Yacoby, A.; Stormer, H. L.; Wingreen, N. S.; Pfeiffer, L. N.; Baldwin, K. W.; West, K. W. Nonuniversal Conductance Quantization in Quantum Wires. *Phys. Rev. Lett.* **1996**, *77*, 4612−4615.
(78) Wu, P. M.; Gooth, J.; Zianni, X.; Svensson, S. F.; Gluschke, J. G.; Dick, K. A.; Thelander, C.; Nielsch, K.; Linke, H. Large Thermoelectric Power Factor Enhancement Observed in InAs Nanowires. *Nano Lett.* **2013**, *13*, 4080−4086.
(79) Liang, G.; Xiang, J.; Kharche, N.; Klimeck, G.; Lieber, C. M.; Lundstrom, M. Performance Analysis of a Ge/Si Core/Shell Nanowire Field-Effect Transistor. *Nano Lett.* **2007**, *7*, 642−646.
(80) Koga, T.; Sun, X.; Cronin, S. B.; Dresselhaus, M. S. Carrier Pocket Engineering to Design Superior Thermoelectric Materials Using GaAs/AlAs Superlattices. *MRS Online Proc. Libr.* **1998**, *545*, 375.
(81) Pei, Y.; Shi, X.; LaLonde, A.; Wang, H.; Chen, L.; Snyder, G. J. Convergence of Electronic Bands for High Performance Bulk Thermoelectrics. *Nature* **2011**, *473*, 66−69.
(82) Small, J. P.; Perez, K. M.; Kim, P. Modulation of Thermoelectric Power of Individual Carbon Nanotubes. *Phys. Rev. Lett.* **2003**, *91*, 256801.
(83) Llaguno, M. C.; Fischer, J. E.; Johnson, A. T.; Hone, J. Observation of Thermopower Oscillations in the Coulomb Blockade Regime in a Semiconducting Carbon Nanotube. *Nano Lett.* **2004**, *4*, 45−49.
(84) Boukai, A.; Xu, K.; Heath, J. R. Size-Dependent Transport and Thermoelectric Properties of Individual Polycrystalline Bismuth Nanowires. *Adv. Mater.* **2006**, *18*, 864−869.

DOI: 10.1021/acs.chemrev.8b00627
Chem. Rev. XXXX, XXX, XXX−XXX

(85) Liang, W.; Hochbaum, A. I.; Fardy, M.; Rabin, O.; Zhang, M.; Yang, P. Field-Effect Modulation of Seebeck Coefficient in Single PbSe Nanowires. *Nano Lett.* **2009**, *9*, 1689−1693.
(86) Moon, J.; Kim, J.-H.; Chen, Z. C. Y.; Xiang, J.; Chen, R. Gate-Modulated Thermoelectric Power Factor of Hole Gas in Ge−Si Core−Shell Nanowires. *Nano Lett.* **2013**, *13*, 1196−1202.
(87) Brovman, Y. M.; Small, J. P.; Hu, Y.; Fang, Y.; Lieber, C. M.; Kim, P. Electric Field Effect Thermoelectric Transport in Individual Silicon and Germanium/Silicon Nanowires. *J. Appl. Phys.* **2016**, *119*, 234304.
(88) Curtin, B. M.; Codecido, E. A.; Krämer, S.; Bowers, J. E. Field-Effect Modulation of Thermoelectric Properties in Multigated Silicon Nanowires. *Nano Lett.* **2013**, *13*, 5503−5508.
(89) Kim, J.; Lee, S.; Brovman, Y. M.; Kim, P.; Lee, W. Diameter-Dependent Thermoelectric Figure of Merit in Single-Crystalline Bi Nanowires. *Nanoscale* **2015**, *7*, 5053−5059.
(90) Zuev, Y. M.; Lee, J. S.; Galloy, C.; Park, H.; Kim, P. Diameter Dependence of the Transport Properties of Antimony Telluride Nanowires. *Nano Lett.* **2010**, *10*, 3037−3040.
(91) Lee, C.-H.; Yi, G.-C.; Zuev, Y. M.; Kim, P. Thermoelectric Power Measurements of Wide Band Gap Semiconducting Nanowires. *Appl. Phys. Lett.* **2009**, *94*, 022106.
(92) Yanagi, K.; Kanda, S.; Oshima, Y.; Kitamura, Y.; Kawai, H.; Yamamoto, T.; Takenobu, T.; Nakai, Y.; Maniwa, Y. Tuning of the Thermoelectric Properties of One-Dimensional Material Networks by Electric Double Layer Techniques Using Ionic Liquids. *Nano Lett.* **2014**, *14*, 6437−6442.
(93) Mavrokefalos, A.; Moore, A. L.; Pettes, M. T.; Shi, L.; Wang, W.; Li, X. Thermoelectric and Structural Characterizations of Individual Electrodeposited Bismuth Telluride Nanowires. *J. Appl. Phys.* **2009**, *105*, 104318.
(94) Mavrokefalos, A.; Pettes, M. T.; Zhou, F.; Shi, L. Four-Probe Measurements of the In-Plane Thermoelectric Properties of Nanofilms. *Rev. Sci. Instrum.* **2007**, *78*, 034901.
(95) Hsin, C.-L.; Wingert, M.; Huang, C.-W.; Guo, H.; Shih, T.-J.; Suh, J.; Wang, K.; Wu, J.; Wu, W.-W.; Chen, R. Phase Transformation and Thermoelectric Properties of Bismuth-Telluride Nanowires. *Nanoscale* **2013**, *5*, 4669.
(96) Valentín, L. A.; Betancourt, J.; Fonseca, L. F.; Pettes, M. T.; Shi, L.; Soszyński, M.; Huczko, A. A Comprehensive Study of Thermoelectric and Transport Properties of β-Silicon Carbide Nanowires. *J. Appl. Phys.* **2013**, *114*, 184301.
(97) Pettes, M. T.; Maassen, J.; Jo, I.; Lundstrom, M. S.; Shi, L. Effects of Surface Band Bending and Scattering on Thermoelectric Transport in Suspended Bismuth Telluride Nanoplates. *Nano Lett.* **2013**, *13*, 5316−5322.
(98) Pettes, M. T.; Kim, J.; Wu, W.; Bustillo, K. C.; Shi, L. Thermoelectric Transport in Surface- and Antimony-Doped Bismuth Telluride Nanoplates. *APL Mater.* **2016**, *4*, 104810.
(99) Lin, Y. M.; Sun, X.; Dresselhaus, M. Theoretical Investigation of Thermoelectric Transport Properties of Cylindrical Bi Nanowires. *Phys. Rev. B: Condens. Matter Mater. Phys.* **2000**, *62*, 4610−4623.
(100) Madelung, O.; Rössler, U.; Schulz, M. *Non-Tetrahedrally Bonded Elements and Binary Compounds I*; Springer: Berlin/Heidelberg, 1998.
(101) Lin, Y.-M.; Cronin, S. B.; Ying, J. Y.; Dresselhaus, M. S.; Heremans, J. P. Transport Properties of Bi Nanowire Arrays. *Appl. Phys. Lett.* **2000**, *76*, 3944.
(102) Heremans, J.; Thrush, C. M.; Lin, Y.-M.; Cronin, S.; Zhang, Z.; Dresselhaus, M. S.; Mansfield, J. F. Bismuth Nanowire Arrays: Synthesis and Galvanomagnetic Properties. *Phys. Rev. B: Condens. Matter Mater. Phys.* **2000**, *61*, 2921−2930.
(103) Lin, Y.-M.; Rabin, O.; Cronin, S. B.; Ying, J. Y.; Dresselhaus, M. S. Semimetal−semiconductor Transition in $Bi_{1-x}Sb_x$ Alloy Nanowires and Their Thermoelectric Properties. *Appl. Phys. Lett.* **2002**, *81*, 2403−2405.
(104) Lin, Y.-M.; Cronin, S. B.; Rabin, O.; Ying, J. Y.; Dresselhaus, M. S. Transport Properties of $Bi_{1-x}Sb_x$ Alloy Nanowires Synthesized by Pressure Injection. *Appl. Phys. Lett.* **2001**, *79*, 677−679.
(105) Murata, M.; Nakamura, D.; Hasegawa, Y.; Komine, T.; Taguchi, T.; Nakamura, S.; Jovovic, V.; Heremans, J. P. Thermoelectric Properties of Bismuth Nanowires in a Quartz Template. *Appl. Phys. Lett.* **2009**, *94*, 192104.
(106) Nikolaeva, A.; Huber, T. E.; Gitsu, D.; Konopko, L. Diameter-Dependent Thermopower of Bismuth Nanowires. *Phys. Rev. B: Condens. Matter Mater. Phys.* **2008**, *77*, 035422.
(107) Koenig, S. H.; Lopez, A. A.; Smith, D. B.; Yarnell, J. L. Location of the Valence-Band Maximum in Bismuth. *Phys. Rev. Lett.* **1968**, *20*, 48−50.
(108) Dresselhaus, M. S.; Chen, G.; Tang, M. Y.; Yang, R. G.; Lee, H.; Wang, D. Z.; Ren, Z. F.; Fleurial, J.-P.; Gogna, P. New Directions for Low-Dimensional Thermoelectric Materials. *Adv. Mater.* **2007**, *19*, 1043−1053.
(109) Shim, W.; Ham, J.; Lee, K.; Jeung, W. Y.; Johnson, M.; Lee, W. On-Film Formation of Bi Nanowires with Extraordinary Electron Mobility. *Nano Lett.* **2009**, *9*, 18−22.
(110) Tu, K. N.; Li, J. C. M. Spontaneous Whisker Growth on Lead-Free Solder Finishes. *Mater. Sci. Eng., A* **2005**, *409*, 131−139.
(111) Shim, W.; Kim, D.; Lee, K.; Jeon, K. J.; Ham, J.; Chang, J.; Han, S.-H.; Jeung, W. Y.; Johnson, M.; Lee, W. Magnetotransport Properties of an Individual Single-Crystalline Bi Nanowire Grown by a Stress Induced Method. *J. Appl. Phys.* **2008**, *104*, 073715.
(112) Shim, W.; Ham, J.; Kim, J.; Lee, W. Shubnikov−de Haas Oscillations in an Individual Single-Crystalline Bismuth Nanowire Grown by on-Film Formation of Nanowires. *Appl. Phys. Lett.* **2009**, *95*, 232107.
(113) Kim, J.; Lee, S.; Brovman, Y. M.; Kim, M.; Kim, P.; Lee, W. Weak Antilocalization and Conductance Fluctuation in a Single Crystalline Bi Nanowire. *Appl. Phys. Lett.* **2014**, *104*, 043105.
(114) Kim, J.; Roh, J. W.; Moon, H.; Lee, W. Observation of Anisotropy in Thermoelectric Properties of Individual Single-Crystalline Bismuth Nanowires. *J. Appl. Phys.* **2017**, *122*, 034303.
(115) Kim, J.; Kim, D.; Chang, T.; Lee, W. Quantum Size Effect on Shubnikov-de Haas Oscillations in 100 nm Diameter Single-Crystalline Bismuth Nanowire. *Appl. Phys. Lett.* **2014**, *105*, 123107.
(116) Cui, Y.; Lieber, C. M.; Bawendi, M. G. Functional Nanoscale Electronic Devices Assembled Using Silicon Nanowire Building Blocks. *Science* **2001**, *291*, 851−853.
(117) Cui, Y.; Lauhon, L. J.; Gudiksen, M. S.; Wang, J.; Lieber, C. M. Diameter-Controlled Synthesis of Single-Crystal Silicon Nanowires. *Appl. Phys. Lett.* **2001**, *78*, 2214−2216.
(118) Holmes, J. D.; Johnston, K. P.; Doty, R. C.; Korgel, B. A. Control of Thickness and Orientation of Solution-Grown Silicon Nanowires. *Science* **2000**, *287*, 1471−1473.
(119) Morales, A. M.; Lieber, C. M. A Laser Ablation Method for the Synthesis of Crystalline Semiconductor Nanowires. *Science* **1998**, *279*, 208−211.
(120) Ma, D. D. D.; Lee, C. S.; Au, F. C. K.; Tong, S. Y.; Lee, S. T. Small-Diameter Silicon Nanowire Surfaces. *Science* **2003**, *299*, 1874−1877.
(121) Yang, J.; Caillat, T. Thermoelectric Materials for Space and Automotive Power Generation. *MRS Bull.* **2006**, *31*, 224−229.
(122) Geballe, T. H.; Hull, G. W. Seebeck Effect in Germanium. *Phys. Rev.* **1954**, *94*, 1134−1140.
(123) Sadhu, J.; Tian, H.; Ma, J.; Azeredo, B.; Kim, J.; Balasundaram, K.; Zhang, C.; Li, X.; Ferreira, P. M.; Sinha, S. Quenched Phonon Drag in Silicon Nanowires Reveals Significant Effect in the Bulk at Room Temperature. *Nano Lett.* **2015**, *15*, 3159−3165.
(124) Garg, J.; Bonini, N.; Kozinsky, B.; Marzari, N. Role of Disorder and Anharmonicity in the Thermal Conductivity of Silicon-Germanium Alloys: A First-Principles Study. *Phys. Rev. Lett.* **2011**, *106*, 045901.
(125) Amato, M.; Palummo, M.; Rurali, R.; Ossicini, S. Silicon−Germanium Nanowires: Chemistry and Physics in Play, from Basic Principles to Advanced Applications. *Chem. Rev.* **2014**, *114*, 1371−1412.

DOI: 10.1021/acs.chemrev.8b00627
Chem. Rev. XXXX, XXX, XXX−XXX

(126) Yin, L.; Kyung Lee, E.; Woon Lee, J.; Whang, D.; Lyong Choi, B.; Yu, C. The Influence of Phonon Scatterings on the Thermal Conductivity of SiGe Nanowires. *Appl. Phys. Lett.* **2012**, *101*, 043114.
(127) Amato, M.; Ossicini, S.; Rurali, R. Electron Transport in SiGe Alloy Nanowires in the Ballistic Regime from First-Principles. *Nano Lett.* **2012**, *12*, 2717−2721.
(128) Kotlyar, R.; Obradovic, B.; Matagne, P.; Stettler, M.; Giles, M. D. Assessment of Room-Temperature Phonon-Limited Mobility in Gated Silicon Nanowires. *Appl. Phys. Lett.* **2004**, *84*, 5270−5272.
(129) Poli, S.; Pala, M. G.; Poiroux, T.; Deleonibus, S.; Baccarani, G. Size Dependence of Surface-Roughness-Limited Mobility in Silicon-Nanowire FETs. *IEEE Trans. Electron Devices* **2008**, *55*, 2968−2976.
(130) Jin, S.; Fischetti, M. V.; Tang, T. Modeling of Electron Mobility in Gated Silicon Nanowires at Room Temperature: Surface Roughness Scattering, Dielectric Screening, and Band Nonparabolicity. *J. Appl. Phys.* **2007**, *102*, 083715.
(131) Cui, Y.; Zhong, Z.; Wang, D.; Wang, W. U.; Lieber, C. M. High Performance Silicon Nanowire Field Effect Transistors. *Nano Lett.* **2003**, *3*, 149−152.
(132) Dan, Y.; Seo, K.; Takei, K.; Meza, J. H.; Javey, A.; Crozier, K. B. Dramatic Reduction of Surface Recombination by in Situ Surface Passivation of Silicon Nanowires. *Nano Lett.* **2011**, *11*, 2527−2532.
(133) Wang, X.; Peng, K.-Q.; Pan, X.-J.; Chen, X.; Yang, Y.; Li, L.; Meng, X.-M.; Zhang, W.-J.; Lee, S.-T. High-Performance Silicon Nanowire Array Photoelectrochemical Solar Cells through Surface Passivation and Modification. *Angew. Chem., Int. Ed.* **2011**, *50*, 9861−9865.
(134) Fonoberov, V. A.; Balandin, A. A. Giant Enhancement of the Carrier Mobility in Silicon Nanowires with Diamond Coating. *Nano Lett.* **2006**, *6*, 2442−2446.
(135) Buin, A. K.; Verma, A.; Svizhenko, A.; Anantram, M. P. Significant Enhancement of Hole Mobility in [110] Silicon Nanowires Compared to Electrons and Bulk Silicon. *Nano Lett.* **2008**, *8*, 760−765.
(136) Niquet, Y. M.; Delerue, C.; Rideau, D.; Videau, B. Fully Atomistic Simulations of Phonon-Limited Mobility of Electrons and Holes in < 001>-, < 110>-, and < 111>-Oriented Si Nanowires. *IEEE Trans. Electron Devices* **2012**, *59*, 1480−1487.
(137) Niquet, Y. M.; Delerue, C.; Krzeminski, C. Effects of Strain on the Carrier Mobility in Silicon Nanowires. *Nano Lett.* **2012**, *12*, 3545−3550.
(138) Hashemi, P.; Gomez, L.; Hoyt, J. L. Gate-All-Around n-MOSFETs With Uniaxial Tensile Strain-Induced Performance Enhancement Scalable to Sub-10-nm Nanowire Diameter. *IEEE Electron Device Lett.* **2009**, *30*, 401−403.
(139) Li, L.; Smith, D.; Madras, P.; Dailey, E.; Drucker, J.; McCartney, M. Hole Accumulation in Ge/Si Core/Shell Nanowires Studied by Electron Holography. *Microsc. Microanal.* **2010**, *16*, 566−567.
(140) Zhang, S.; Lopez, F. J.; Hyun, J. K.; Lauhon, L. J. Direct Detection of Hole Gas in Ge-Si Core-Shell Nanowires by Enhanced Raman Scattering. *Nano Lett.* **2010**, *10*, 4483−4487.
(141) Fukata, N.; Yu, M.; Jevasuwan, W.; Takei, T.; Bando, Y.; Wu, W.; Wang, Z. L. Clear Experimental Demonstration of Hole Gas Accumulation in Ge/Si Core-Shell Nanowires. *ACS Nano* **2015**, *9*, 12182−12188.
(142) Amato, M.; Ossicini, S.; Rurali, R. Band-Offset Driven Efficiency of the Doping of SiGe Core−Shell Nanowires. *Nano Lett.* **2011**, *11*, 594−598.
(143) Lauhon, L. J.; Gudiksen, M. S.; Wang, D.; Lieber, C. M. Epitaxial Core-shell and Core-multishell Nanowire Heterostructures. *Nature* **2002**, *420*, 57−61.
(144) Xiang, J.; Lu, W.; Hu, Y.; Wu, Y.; Yan, H.; Lieber, C. M. Ge/Si Nanowire Heterostructures as High-Performance Field-Effect Transistors. *Nature* **2006**, *441*, 489−493.
(145) Nguyen, B.-M.; Taur, Y.; Picraux, S. T.; Dayeh, S. A. Diameter-Independent Hole Mobility in Ge/Si Core/Shell Nanowire Field Effect Transistors. *Nano Lett.* **2014**, *14*, 585−591.
(146) Conesa-Boj, S.; Li, A.; Koelling, S.; Brauns, M.; Ridderbos, J.; Nguyen, T. T.; Verheijen, M. A.; Koenraad, P. M.; Zwanenburg, F. A.; Bakkers, E. P. A. M. Boosting Hole Mobility in Coherently Strained [110]-Oriented Ge-Si Core-Shell Nanowires. *Nano Lett.* **2017**, *17*, 2259−2264.
(147) Li, Y.; Xiang, J.; Qian, F.; Gradečak, S.; Wu, Y.; Yan, H.; Blom, D. A.; Lieber, C. M. Dopant-Free GaN/AlN/AlGaN Radial Nanowire Heterostructures as High Electron Mobility Transistors. *Nano Lett.* **2006**, *6*, 1468−1473.
(148) Dayeh, S. A.; Gin, A. V.; Picraux, S. T. Advanced Core/Multishell Germanium/Silicon Nanowire Heterostructures: Morphology and Transport. *Appl. Phys. Lett.* **2011**, *98*, 163112.
(149) Dillen, D. C.; Kim, K.; Liu, E.-S.; Tutuc, E. Radial Modulation Doping in Core-shell Nanowires. *Nat. Nanotechnol.* **2014**, *9*, 116−120.
(150) Royo, M.; De Luca, M.; Rurali, R.; Zardo, I. A Review on III-V Core-Multishell Nanowires: Growth, Properties, and Applications. *J. Phys. D: Appl. Phys.* **2017**, *50*, 143001.
(151) Funk, S.; Royo, M.; Zardo, I.; Rudolph, D.; Morkötter, S.; Mayer, B.; Becker, J.; Bechtold, A.; Matich, S.; Döblinger, M.; et al. High Mobility One- and Two-Dimensional Electron Systems in Nanowire-Based Quantum Heterostructures. *Nano Lett.* **2013**, *13*, 6189−6196.
(152) Boland, J. L.; Conesa-Boj, S.; Parkinson, P.; Tütüncüoglu, G.; Matteini, F.; Rüffer, D.; Casadei, A.; Amaduzzi, F.; Jabeen, F.; Davies, C. L.; et al. Modulation Doping of GaAs/AlGaAs Core-Shell Nanowires With Effective Defect Passivation and High Electron Mobility. *Nano Lett.* **2015**, *15*, 1336−1342.
(153) Morkötter, S.; Jeon, N.; Rudolph, D.; Loitsch, B.; Spirkoska, D.; Hoffmann, E.; Döblinger, M.; Matich, S.; Finley, J. J.; Lauhon, L. J.; et al. Demonstration of Confined Electron Gas and Steep-Slope Behavior in Delta-Doped GaAs-AlGaAs Core-Shell Nanowire Transistors. *Nano Lett.* **2015**, *15*, 3295−3302.
(154) Tomioka, K.; Yoshimura, M.; Fukui, T. A III-V Nanowire Channel on Silicon for High-Performance Vertical Transistors. *Nature* **2012**, *488*, 189−192.
(155) Gül, Ö.; Günel, H. Y.; Lüth, H.; Rieger, T.; Wenz, T.; Haas, F.; Lepsa, M.; Panaitov, G.; Grützmacher, D.; SchäPers, T. Giant Magnetoconductance Oscillations in Hybrid Superconductor-Semiconductor Core/Shell Nanowire Devices. *Nano Lett.* **2014**, *14*, 6269−6274.
(156) Blömers, C.; Rieger, T.; Zellekens, P.; Haas, F.; Lepsa, M. I.; Hardtdegen, H.; Gül, Ö.; Demarina, N.; Grützmacher, D.; Lüth, H.; et al. Realization of Nanoscaled Tubular Conductors by Means of GaAs/InAs Core/Shell Nanowires. *Nanotechnology* **2013**, *24*, 035203.
(157) Markussen, T. Surface Disordered Ge-Si Core-Shell Nanowires as Efficient Thermoelectric Materials. *Nano Lett.* **2012**, *12*, 4698−4704.
(158) Curtin, B. M.; Bowers, J. E. Thermoelectric Power Factor Enhancement with Gate-All-around Silicon Nanowires. *J. Appl. Phys.* **2014**, *115*, 143704.
(159) Neophytou, N.; Karamitaheri, H.; Kosina, H. Use of Field-Effect Density Modulation to Increase ZT for Si Nanowires: A Simulation Study. *J. Electron. Mater.* **2015**, *44*, 1599−1605.
(160) Neophytou, N.; Kosina, H. Gated Si Nanowires for Large Thermoelectric Power Factors. *Appl. Phys. Lett.* **2014**, *105*, 073119.
(161) Gamalski, A. D.; Ducati, C.; Hofmann, S. Cyclic Supersaturation and Triple Phase Boundary Dynamics in Germanium Nanowire Growth. *J. Phys. Chem. C* **2011**, *115*, 4413−4417.
(162) Oh, S. H.; Chisholm, M. F.; Kauffmann, Y.; Kaplan, W. D.; Luo, W.; Rühle, M.; Scheu, C. Oscillatory Mass Transport in Vapor-Liquid-Solid Growth of Sapphire Nanowires. *Science* **2010**, *330*, 489−493.
(163) Perea, D. E.; Hemesath, E. R.; Schwalbach, E. J.; Lensch-Falk, J. L.; Voorhees, P. W.; Lauhon, L. J. Direct Measurement of Dopant Distribution in an Individual Vapour-liquid-solid Nanowire. *Nat. Nanotechnol.* **2009**, *4*, 315−319.
(164) Connell, J. G.; Yoon, K.; Perea, D. E.; Schwalbach, E. J.; Voorhees, P. W.; Lauhon, L. J. Identification of an Intrinsic Source of

DOI: 10.1021/acs.chemrev.8b00627
Chem. Rev. XXXX, XXX, XXX−XXX

Doping Inhomogeneity in Vapor-Liquid-Solid-Grown Nanowires. *Nano Lett.* **2013**, *13*, 199−206.
(165) Ek, M.; Filler, M. A. Atomic-Scale Choreography of Vapor-Liquid-Solid Nanowire Growth. *Acc. Chem. Res.* **2018**, *51*, 118−126.
(166) Garnett, E. C.; Tseng, Y.-C.; Khanal, D. R.; Wu, J.; Bokor, J.; Yang, P. Dopant Profiling and Surface Analysis of Silicon Nanowires Using Capacitance-voltage Measurements. *Nat. Nanotechnol.* **2009**, *4*, 311−314.
(167) Zhuge, F.; Yanagida, T.; Fukata, N.; Uchida, K.; Kanai, M.; Nagashima, K.; Meng, G.; He, Y.; Rahong, S.; Li, X.; et al. Modulation of Thermoelectric Power Factor via Radial Dopant Inhomogeneity in B-Doped Si Nanowires. *J. Am. Chem. Soc.* **2014**, *136*, 14100−14106.
(168) Ivanov, Y. V.; Burkov, A. T.; Pshenay-Severin, D. A. Thermoelectric Properties of Topological Insulators. *Phys. Status Solidi B* **2018**, *255*, 1800020.
(169) König, M.; Wiedmann, S.; Brüne, C.; Roth, A.; Buhmann, H.; Molenkamp, L. W.; Qi, X.-L.; Zhang, S.-C. Quantum Spin Hall Insulator State in HgTe Quantum Wells. *Science* **2007**, *318*, 766−770.
(170) Gooth, J.; Hamdou, B.; Dorn, A.; Zierold, R.; Nielsch, K. Resolving the Dirac Cone on the Surface of Bi_2Te_3 Topological Insulator Nanowires by Field-Effect Measurements. *Appl. Phys. Lett.* **2014**, *104*, 243115.
(171) Chen, Y. L.; Analytis, J. G.; Chu, J.-H.; Liu, Z. K.; Mo, S.-K.; Qi, X. L.; Zhang, H. J.; Lu, D. H.; Dai, X.; Fang, Z.; et al. Experimental Realization of a Three-Dimensional Topological Insulator, Bi2Te3. *Science* **2009**, *325*, 178−181.
(172) Hsieh, D.; Xia, Y.; Qian, D.; Wray, L.; Dil, J. H.; Meier, F.; Osterwalder, J.; Patthey, L.; Checkelsky, J. G.; Ong, N. P.; et al. A Tunable Topological Insulator in the Spin Helical Dirac Transport Regime. *Nature* **2009**, *460*, 1101−1105.
(173) Zhang, T.; Cheng, P.; Chen, X.; Jia, J.-F.; Ma, X.; He, K.; Wang, L.; Zhang, H.; Dai, X.; Fang, Z.; et al. Experimental Demonstration of Topological Surface States Protected by Time-Reversal Symmetry. *Phys. Rev. Lett.* **2009**, *103*, 266803.
(174) Hsieh, D.; Xia, Y.; Qian, D.; Wray, L.; Meier, F.; Dil, J. H.; Osterwalder, J.; Patthey, L.; Fedorov, A. V.; Lin, H.; et al. Observation of Time-Reversal-Protected Single-Dirac-Cone Topological-Insulator States in Bi_2Te_3 and Sb_2Te_3. *Phys. Rev. Lett.* **2009**, *103*, 146401.
(175) Xia, Y.; Qian, D.; Hsieh, D.; Wray, L.; Pal, A.; Lin, H.; Bansil, A.; Grauer, D.; Hor, Y. S.; Cava, R. J.; et al. Observation of a Large-Gap Topological-Insulator Class with a Single Dirac Cone on the Surface. *Nat. Phys.* **2009**, *5*, 398−402.
(176) Hsieh, D.; Xia, Y.; Wray, L.; Qian, D.; Pal, A.; Dil, J. H.; Osterwalder, J.; Meier, F.; Bihlmayer, G.; Kane, C. L.; et al. Observation of Unconventional Quantum Spin Textures in Topological Insulators. *Science* **2009**, *323*, 919−922.
(177) Zhang, J.; Chang, C.; Zhang, Z.; Wen, J.; Feng, X.; Li, K.; Liu, M.; He, K.; Wang, L.; Chen, X.; et al. Band Structure Engineering in $(Bi_{1-x}Sb_x)_2Te_3$ Ternary Topological Insulators. *Nat. Commun.* **2011**, *2*, 574.
(178) Osterhage, H.; Gooth, J.; Hamdou, B.; Gwozdz, P.; Zierold, R.; Nielsch, K. Thermoelectric Properties of Topological Insulator Bi_2Te_3, Sb_2Te_3, and Bi_2Se_3 Thin Film Quantum Wells. *Appl. Phys. Lett.* **2014**, *105*, 123117.
(179) Chen, Y. L.; Liu, Z. K.; Analytis, J. G.; Chu, J.-H.; Zhang, H. J.; Yan, B. H.; Mo, S.-K.; Moore, R. G.; Lu, D. H.; Fisher, I. R.; et al. Single Dirac Cone Topological Surface State and Unusual Thermoelectric Property of Compounds from a New Topological Insulator Family. *Phys. Rev. Lett.* **2010**, *105*, 266401.
(180) Gooth, J.; Gluschke, J. G.; Zierold, R.; Leijnse, M.; Linke, H.; Nielsch, K. Thermoelectric Performance of Classical Topological Insulator Nanowires. *Semicond. Sci. Technol.* **2015**, *30*, 015015.
(181) Ghaemi, P.; Mong, R. S. K.; Moore, J. E. In-Plane Transport and Enhanced Thermoelectric Performance in Thin Films of the Topological Insulators Bi_2Te_3 and Bi_2Se_3. *Phys. Rev. Lett.* **2010**, *105*, 166603.
(182) Tretiakov, O. A.; Abanov, A.; Murakami, S.; Sinova, J. Large Thermoelectric Figure of Merit for Three-Dimensional Topological Anderson Insulators via Line Dislocation Engineering. *Appl. Phys. Lett.* **2010**, *97*, 073108.
(183) Takahashi, R.; Murakami, S. Thermoelectric Transport in Topological Insulators. *Semicond. Sci. Technol.* **2012**, *27*, 124005.
(184) Hamdou, B.; Kimling, J.; Dorn, A.; Pippel, E.; Rostek, R.; Woias, P.; Nielsch, K. Thermoelectric Characterization of Bismuth Telluride Nanowires, Synthesized via Catalytic Growth and Post-Annealing. *Adv. Mater.* **2013**, *25*, 239−244.
(185) Hamdou, B.; Gooth, J.; Böhnert, T.; Dorn, A.; Akinsinde, L.; Pippel, E.; Zierold, R.; Nielsch, K. Thermoelectric Properties of Band Structure Engineered Topological Insulator $(Bi_{1-x}Sb_x)_2Te_3$ Nanowires. *Adv. Energy Mater.* **2015**, *5*, 1500280.
(186) Shin, H. S.; Hamdou, B.; Reith, H.; Osterhage, H.; Gooth, J.; Damm, C.; Rellinghaus, B.; Pippel, E.; Nielsch, K. The Surface-to-Volume Ratio: A Key Parameter in the Thermoelectric Transport of Topological Insulator Bi_2Se_3 Nanowires. *Nanoscale* **2016**, *8*, 13552−13557.
(187) Chen, G. *Nanoscale Energy Transport and Conversion: A Parallel Treatment of Electrons, Molecules, Phonons, and Photons*; Oxford University Press, 2005.
(188) Wingert, M. C.; Chen, Z. C. Y.; Kwon, S.; Xiang, J.; Chen, R. Ultra-Sensitive Thermal Conductance Measurement of One-Dimensional Nanostructures Enhanced by Differential Bridge. *Rev. Sci. Instrum.* **2012**, *83*, 024901.
(189) Li, D. Thermal Transport in Individual Nanowires and Nanotubes. Ph.D. Thesis, University of California, Berkeley, 2002.
(190) Swinkels, M. Y.; van Delft, M. R.; Oliveira, D. S.; Cavalli, A.; Zardo, I.; van der Heijden, R. W.; Bakkers, E. P. A. M. Diameter Dependence of the Thermal Conductivity of InAs Nanowires. *Nanotechnology* **2015**, *26*, 385401.
(191) Zhang, Q.; Liu, C.; Liu, X.; Liu, J.; Cui, Z.; Zhang, Y.; Yang, L.; Zhao, Y.; Xu, T. T.; Chen, Y.; et al. Thermal Transport in Quasi-1D van Der Waals Crystal $Ta_2Pd_3Se_8$ Nanowires: Size and Length Dependence. *ACS Nano* **2018**, *12*, 2634−2642.
(192) Yang, J.; Yang, Y.; Waltermire, S. W.; Gutu, T.; Zinn, A. a.; Xu, T. T.; Chen, Y.; Li, D. Measurement of the Intrinsic Thermal Conductivity of a Multiwalled Carbon Nanotube and Its Contact Thermal Resistance with the Substrate. *Small* **2011**, *7*, 2334−2340.
(193) Wang, Z.; Xie, R.; Bui, C. T.; Liu, D.; Ni, X.; Li, B.; Thong, J. T. L. Thermal Transport in Suspended and Supported Few-Layer Graphene. *Nano Lett.* **2011**, *11*, 113−118.
(194) Zhang, Q. Thermal Transport in Individual Nanowires of Fine Structures. Ph.D. Thesis,Vanderbilt University, 2017.
(195) Kim, J.; Ou, E.; Sellan, D. P.; Shi, L. A Four-Probe Thermal Transport Measurement Method for Nanostructures. *Rev. Sci. Instrum.* **2015**, *86*, 044901.
(196) Hou, J.; Wang, X.; Vellelacheruvu, P.; Guo, J.; Liu, C.; Cheng, H.-M. Thermal Characterization of Single-Wall Carbon Nanotube Bundles Using the Self-Heating 3ω Technique. *J. Appl. Phys.* **2006**, *100*, 124314.
(197) Li, G.; Liang, D.; Qiu, R. L. J.; Gao, X. P. A. Thermal Conductivity Measurement of Individual Bi_2Se_3 Nano-Ribbon by Self-Heating Three-ω Method. *Appl. Phys. Lett.* **2013**, *102*, 043104.
(198) Huang, X.; Liu, G.; Wang, X. New Secrets of Spider Silk: Exceptionally High Thermal Conductivity and Its Abnormal Change under Stretching. *Adv. Mater.* **2012**, *24*, 1482−1486.
(199) Yang, L.; Tao, Y.; Liu, J.; Liu, C.; Zhang, Q.; Akter, M.; Zhao, Y.; Xu, T. T.; Xu, Y.; Mao, Z.; et al. Distinct Signatures of Electron−Phonon Coupling Observed in the Lattice Thermal Conductivity of $NbSe_3$ Nanowires. *Nano Lett.* **2019**, *19*, 415−421.
(200) Yang, L.; Zhang, Q.; Cui, Z.; Gerboth, M.; Zhao, Y.; Xu, T. T.; Walker, D. G.; Li, D. Ballistic Phonon Penetration Depth in Amorphous Silicon Dioxide. *Nano Lett.* **2017**, *17*, 7218−7225.
(201) Fujii, M.; Zhang, X.; Xie, H.; Ago, H.; Takahashi, K.; Ikuta, T.; Abe, H.; Shimizu, T. Measuring the Thermal Conductivity of a Single Carbon Nanotube. *Phys. Rev. Lett.* **2005**, *95*, 065502.
(202) Yi, W.; Lu, L.; Dian-lin, Z.; Pan, Z. W.; Xie, S. S. Linear Specific Heat of Carbon Nanotubes. *Phys. Rev. B: Condens. Matter Mater. Phys.* **1999**, *59*, R9015−R9018.

DOI: 10.1021/acs.chemrev.8b00627
Chem. Rev. XXXX, XXX, XXX−XXX

(203) Heron, J. S.; Fournier, T.; Mingo, N.; Bourgeois, O. Mesoscopic Size Effects on the Thermal Conductance of Silicon Nanowire. *Nano Lett.* **2009**, *9*, 1861−1865.
(204) Soini, M.; Zardo, I.; Uccelli, E.; Funk, S.; Koblmüller, G.; Fontcuberta i Morral, A.; Abstreiter, G. Thermal Conductivity of GaAs Nanowires Studied by Micro-Raman Spectroscopy Combined with Laser Heating. *Appl. Phys. Lett.* **2010**, *97*, 263107.
(205) Doerk, G. S.; Carraro, C.; Maboudian, R. Single Nanowire Thermal Conductivity Measurements by Raman Thermography. *ACS Nano* **2010**, *4*, 4908−4914.
(206) Yue, Y.; Eres, G.; Wang, X.; Guo, L. Characterization of Thermal Transport in Micro/Nanoscale Wires by Steady-State Electro-Raman-Thermal Technique. *Appl. Phys. A: Mater. Sci. Process.* **2009**, *97*, 19−23.
(207) Weathers, A.; Shi, L. Thermal Transport Measurement Techniques for Nanowires and Nanotubes. *Annu. Rev. Heat Transfer* **2013**, *16*, 101−134.
(208) Yue, Y.; Wang, X. Nanoscale Thermal Probing. *Nano Rev.* **2012**, *3*, 11586.
(209) Ju, Y. S.; Goodson, K. E. Phonon Scattering in Silicon Films with Thickness of Order 100 nm. *Appl. Phys. Lett.* **1999**, *74*, 3005.
(210) Mingo, N. Calculation of Si Nanowire Thermal Conductivity Using Complete Phonon Dispersion Relations. *Phys. Rev. B: Condens. Matter Mater. Phys.* **2003**, *68*, 113308.
(211) Mingo, N.; Yang, L.; Li, D.; Majumdar, A. Predicting the Thermal Conductivity of Si and Ge Nanowires. *Nano Lett.* **2003**, *3*, 1713−1716.
(212) Chen, R.; Hochbaum, A. I.; Murphy, P.; Moore, J.; Yang, P.; Majumdar, A. Thermal Conductance of Thin Silicon Nanowires. *Phys. Rev. Lett.* **2008**, *101*, 105501.
(213) Dames, C.; Chen, G. Theoretical Phonon Thermal Conductivity of Si/Ge Superlattice Nanowires. *J. Appl. Phys.* **2004**, *95*, 682−693.
(214) Yang, L.; Yang, Y.; Zhang, Q.; Zhang, Y.; Jiang, Y.; Guan, Z.; Gerboth, M.; Yang, J.; Chen, Y.; Greg Walker, D.; et al. Thermal Conductivity of Individual Silicon Nanoribbons. *Nanoscale* **2016**, *8*, 17895−17901.
(215) Park, W.; Shin, D. D.; Kim, S. J.; Katz, J. S.; Park, J.; Ahn, C. H.; Kodama, T.; Asheghi, M.; Kenny, T. W.; Goodson, K. E. Phonon Conduction in Silicon Nanobeams. *Appl. Phys. Lett.* **2017**, *110*, 213102.
(216) Asheghi, M.; Touzelbaev, M. N.; Goodson, K. E.; Leung, Y. K.; Wong, S. S. Temperature-Dependent Thermal Conductivity of Single-Crystal Silicon Layers in SOI Substrates. *J. Heat Transfer* **1998**, *120*, 30−36.
(217) Liu, W.; Asheghi, M. Thermal Conduction in Ultrathin Pure and Doped Single-Crystal Silicon Layers at High Temperatures. *J. Appl. Phys.* **2005**, *98*, 123523.
(218) Maire, J.; Anufriev, R.; Nomura, M. Ballistic Thermal Transport in Silicon Nanowires. *Sci. Rep.* **2017**, *7*, 41794.
(219) Yu, J.-K.; Mitrovic, S.; Tham, D.; Varghese, J.; Heath, J. R. Reduction of Thermal Conductivity in Phononic Nanomesh Structures. *Nat. Nanotechnol.* **2010**, *5*, 718−721.
(220) Wingert, M. C.; Kwon, S.; Hu, M.; Poulikakos, D.; Xiang, J.; Chen, R. Sub-Amorphous Thermal Conductivity in Ultrathin Crystalline Silicon Nanotubes. *Nano Lett.* **2015**, *15*, 2605−2611.
(221) Ward, A.; Broido, D. A. Intrinsic Phonon Relaxation Times from First-Principles Studies of the Thermal Conductivities of Si and Ge. *Phys. Rev. B: Condens. Matter Mater. Phys.* **2010**, *81*, 085205.
(222) Tian, Z.; Esfarjani, K.; Shiomi, J.; Henry, A. S.; Chen, G. On the Importance of Optical Phonons to Thermal Conductivity in Nanostructures. *Appl. Phys. Lett.* **2011**, *99*, 053122.
(223) Mukherjee, S.; Givan, U.; Senz, S.; Bergeron, A.; Francoeur, S.; de la Mata, M.; Arbiol, J.; Sekiguchi, T.; Itoh, K. M.; Isheim, D.; et al. Phonon Engineering in Isotopically Disordered Silicon Nanowires. *Nano Lett.* **2015**, *15*, 3885−3893.
(224) Royo, M.; Rurali, R. Tuning Thermal Transport in Si Nanowires by Isotope Engineering. *Phys. Chem. Chem. Phys.* **2016**, *18*, 26262−26267.
(225) Zhu, G. H.; Lee, H.; Lan, Y. C.; Wang, X. W.; Joshi, G.; Wang, D. Z.; Yang, J.; Vashaee, D.; Guilbert, H.; Pillitteri, A.; et al. Increased Phonon Scattering by Nanograins and Point Defects in Nanostructured Silicon with a Low Concentration of Germanium. *Phys. Rev. Lett.* **2009**, *102*, 196803.
(226) Bera, C.; Mingo, N.; Volz, S. Marked Effects of Alloying on the Thermal Conductivity of Nanoporous Materials. *Phys. Rev. Lett.* **2010**, *104*, 115502.
(227) Wang, Z.; Mingo, N. Diameter Dependence of SiGe Nanowire Thermal Conductivity. *Appl. Phys. Lett.* **2010**, *97*, 101903.
(228) Martinez, J. A.; Provencio, P. P.; Picraux, S. T.; Sullivan, J. P.; Swartzentruber, B. S. Enhanced Thermoelectric Figure of Merit in SiGe Alloy Nanowires by Boundary and Hole-Phonon Scattering. *J. Appl. Phys.* **2011**, *110*, 074317.
(229) Hsiao, T.-K.; Chang, H.-K.; Liou, S.-C.; Chu, M.-W.; Lee, S.-C.; Chang, C.-W. Observation of Room-Temperature Ballistic Thermal Conduction Persisting over 8.3 μm in SiGe Nanowires. *Nat. Nanotechnol.* **2013**, *8*, 534−538.
(230) Li, D.; Pricto, A. L.; Wu, Y.; Martin-Gonzalez, M. S.; Stacy, A.; Sands, T.; Gronsky, R.; Yang, P.; Majumdar, A. Measurements of Bi_2Te_3 Nanowire Thermal Conductivity and Seebeck Coefficient. *Proceedings of the IEEE International Conference on Thermoelectrics, ICT*; IEEE, 2002; pp 333−336.
(231) Biswas, K. G.; Sands, T. D.; Cola, B. A.; Xu, X. Thermal Conductivity of Bismuth Telluride Nanowire Array-Epoxy Composite. *Appl. Phys. Lett.* **2009**, *94*, 223116.
(232) Muñoz Rojo, M.; Grauby, S.; Rampnoux, J.-M.; Caballero-Calero, O.; Martin-Gonzalez, M.; Dilhaire, S. Fabrication of Bi_2Te_3 Nanowire Arrays and Thermal Conductivity Measurement by 3ω-Scanning Thermal Microscopy. *J. Appl. Phys.* **2013**, *113*, 054308.
(233) Wang, Y.; Qiu, B.; McGaughey, A. J. H.; Ruan, X.; Xu, X. Mode-Wise Thermal Conductivity of Bismuth Telluride. *J. Heat Transfer* **2013**, *135*, 091102.
(234) Muñoz Rojo, M.; Abad, B.; Manzano, C. V.; Torres, P.; Cartoixà, X.; Alvarez, F. X.; Martín Gonzalez, M. Thermal Conductivity of Bi_2Te_3 Nanowires: How Size Affects Phonon Scattering. *Nanoscale* **2017**, *9*, 6741−6747.
(235) Qiu, B.; Sun, L.; Ruan, X. Lattice Thermal Conductivity Reduction in Bi_2Te_3 Quantum Wires with Smooth and Rough Surfaces: A Molecular Dynamics Study. *Phys. Rev. B: Condens. Matter Mater. Phys.* **2011**, *83*, 035312.
(236) Fardy, M.; Hochbaum, A. I.; Goldberger, J.; Zhang, M. M.; Yang, P. Synthesis and Thermoelectrical Characterization of Lead Chalcogenide Nanowires. *Adv. Mater.* **2007**, *19*, 3047−3051.
(237) Qiu, B.; Bao, H.; Ruan, X.; Zhang, G.; Wu, Y. Molecular Dynamics Simulations of Lattice Thermal Conductivity and Spectral Phonon Mean Free Path of PbTe: Bulk and Nanostructures. *Volume 1: Heat Transfer in Energy Systems; Theory and Fundamental Research; Aerospace Heat Transfer; Gas Turbine Heat Transfer; Transport Phenomena in Materials Processing and Manufacturing*; ASME, 2012; pp 659−670.
(238) Wingert, M. C.; Chen, Z. C. Y.; Dechaumphai, E.; Moon, J.; Kim, J.; Xiang, J.; Chen, R. Thermal Conductivity of Ge and Ge-Si Core-Shell Nanowires in the Phonon Confinement Regime. *Nano Lett.* **2011**, *11*, 5507−5513.
(239) Zhu, Y.; Xu, F.; Qin, Q.; Fung, W. Y.; Lu, W. Mechanical Properties of Vapor-Liquid-Solid Synthesized Silicon Nanowires. *Nano Lett.* **2009**, *9*, 3934−3939.
(240) Chen, C. Q.; Shi, Y.; Zhang, Y. S.; Zhu, J.; Yan, Y. J. Size Dependence of Young's Modulus in ZnO Nanowires. *Phys. Rev. Lett.* **2006**, *96*, 075505.
(241) Dai, S.; Zhao, J.; He, M. R.; Wang, X.; Wan, J.; Shan, Z.; Zhu, J. Elastic Properties of GaN Nanowires: Revealing the Influence of Planar Defects on Young's Modulus at Nanoscale. *Nano Lett.* **2015**, *15*, 8−15.
(242) Zhao, Y.; Yang, L.; Kong, L.; Nai, M. H.; Liu, D.; Wu, J.; Liu, Y.; Chiam, S. Y.; Chim, W. K.; Lim, C. T.; et al. Ultralow Thermal Conductivity of Single-Crystalline Porous Silicon Nanowires. *Adv. Funct. Mater.* **2017**, *27*, 1702824.

DOI: 10.1021/acs.chemrev.8b00627
Chem. Rev. XXXX, XXX, XXX−XXX

(243) Nilsson, S. G.; Borrisé, X.; Montelius, L. Size Effect on Young's Modulus of Thin Chromium Cantilevers. *Appl. Phys. Lett.* **2004**, *85*, 3555−3557.
(244) Cuenot, S.; Frétigny, C.; Demoustier-Champagne, S.; Nysten, B. Surface Tension Effect on the Mechanical Properties of Nanomaterials Measured by Atomic Force Microscopy. *Phys. Rev. B: Condens. Matter Mater. Phys.* **2004**, *69*, 165410.
(245) Bui, C. T.; Xie, R.; Zheng, M.; Zhang, Q.; Sow, C. H.; Li, B.; Thong, J. T. L. Diameter-Dependent Thermal Transport in Individual ZnO Nanowires and Its Correlation with Surface Coating and Defects. *Small* **2012**, *8*, 738−745.
(246) Park, Y.-H.; Kim, J.; Kim, H.; Kim, I.; Lee, K.-Y.; Seo, D.; Choi, H.-J.; Kim, W. Thermal Conductivity of VLS-Grown Rough Si Nanowires with Various Surface Roughnesses and Diameters. *Appl. Phys. A: Mater. Sci. Process.* **2011**, *104*, 7−14.
(247) Feser, J. P.; Sadhu, J. S.; Azeredo, B. P.; Hsu, K. H.; Ma, J.; Kim, J.; Seong, M.; Fang, N. X.; Li, X.; Ferreira, P. M.; et al. Thermal Conductivity of Silicon Nanowire Arrays with Controlled Roughness. *J. Appl. Phys.* **2012**, *112*, 114306.
(248) Blanc, C.; Rajabpour, A.; Volz, S.; Fournier, T.; Bourgeois, O. Phonon Heat Conduction in Corrugated Silicon Nanowires below the Casimir Limit. *Appl. Phys. Lett.* **2013**, *103*, 043109.
(249) Moore, A. L.; Saha, S. K.; Prasher, R. S.; Shi, L. Phonon Backscattering and Thermal Conductivity Suppression in Sawtooth Nanowires. *Appl. Phys. Lett.* **2008**, *93*, 083112.
(250) Wang, Z.; Ni, Z.; Zhao, R.; Chen, M.; Bi, K.; Chen, Y. The Effect of Surface Roughness on Lattice Thermal Conductivity of Silicon Nanowires. *Phys. B* **2011**, *406*, 2515−2520.
(251) Sansoz, F. Surface Faceting Dependence of Thermal Transport in Silicon Nanowires. *Nano Lett.* **2011**, *11*, 5378−5382.
(252) Carrete, J.; Gallego, L. J.; Varela, L. M.; Mingo, N. Surface Roughness and Thermal Conductivity of Semiconductor Nanowires: Going below the Casimir Limit. *Phys. Rev. B: Condens. Matter Mater. Phys.* **2011**, *84*, 075403.
(253) Sadhu, J.; Sinha, S. Room-Temperature Phonon Boundary Scattering below the Casimir Limit. *Phys. Rev. B: Condens. Matter Mater. Phys.* **2011**, *84*, 115450.
(254) Liu, L.; Chen, X. Effect of Surface Roughness on Thermal Conductivity of Silicon Nanowires. *J. Appl. Phys.* **2010**, *107*, 033501.
(255) He, Y.; Galli, G. Microscopic Origin of the Reduced Thermal Conductivity of Silicon Nanowires. *Phys. Rev. Lett.* **2012**, *108*, 215901.
(256) Kim, H.; Park, Y.-H.; Kim, I.; Kim, J.; Choi, H.-J.; Kim, W. Effect of Surface Roughness on Thermal Conductivity of VLS-Grown Rough $Si_{1-x}Ge_x$ Nanowires. *Appl. Phys. A: Mater. Sci. Process.* **2011**, *104*, 23−28.
(257) Kojda, D.; Mitdank, R.; Mogilatenko, A.; Töllner, W.; Wang, Z.; Kröner, M.; Woias, P.; Nielsch, K.; Fischer, S. F. The Effect of a Distinct Diameter Variation on the Thermoelectric Properties of Individual $Bi_{0.39}Te_{0.61}$ Nanowires. *Semicond. Sci. Technol.* **2014**, *29*, 124006.
(258) Hochbaum, A. I.; Gargas, D.; Hwang, Y. J.; Yang, P. Single Crystalline Mesoporous Silicon Nanowires. *Nano Lett.* **2009**, *9*, 3550−3554.
(259) Ferrando-Villalba, P.; D'Ortenzi, L.; Dalkiranis, G. G.; Cara, E.; Lopeandia, A. F.; Abad, L.; Rurali, R.; Cartoixà, X.; De Leo, N.; Saghi, Z.; et al. Impact of Pore Anisotropy on the Thermal Conductivity of Porous Si Nanowires. *Sci. Rep.* **2018**, *8*, 12796.
(260) Xiong, S.; Kosevich, Y. a.; Sääskilahti, K.; Ni, Y.; Volz, S. Tunable Thermal Conductivity in Silicon Twinning Superlattice Nanowires. *Phys. Rev. B: Condens. Matter Mater. Phys.* **2014**, *90*, 195439.
(261) Zhang, Q.; Cui, Z.; Wei, Z.; Chang, S. Y.; Yang, L.; Zhao, Y.; Yang, Y.; Guan, Z.; Jiang, Y.; Fowlkes, J.; et al. Defect Facilitated Phonon Transport through Kinks in Boron Carbide Nanowires. *Nano Lett.* **2017**, *17*, 3550−3555.
(262) Maire, J.; Anufriev, R.; Hori, T.; Shiomi, J.; Volz, S.; Nomura, M. Thermal Conductivity Reduction in Silicon Fishbone Nanowires. *Sci. Rep.* **2018**, *8*, 4452.
(263) Nomura, M.; Maire, J. Mechanism of the Reduced Thermal Conductivity of Fishbone-Type Si Phononic Crystal Nanostructures. *J. Electron. Mater.* **2015**, *44*, 1426−1431.
(264) Maire, J.; Nomura, M. Reduced Thermal Conductivities of Si One-Dimensional Periodic Structure and Nanowire. *Jpn. J. Appl. Phys.* **2014**, *53*, 06JE09.
(265) Markussen, T.; Jauho, A.-P.; Brandbyge, M. Surface-Decorated Silicon Nanowires: A Route to High-ZT Thermoelectrics. *Phys. Rev. Lett.* **2009**, *103*, 055502.
(266) Ravichandran, J.; Yadav, A. K.; Cheaito, R.; Rossen, P. B.; Soukiassian, A.; Suresha, S. J.; Duda, J. C.; Foley, B. M.; Lee, C.-H.; Zhu, Y.; et al. Crossover from Incoherent to Coherent Phonon Scattering in Epitaxial Oxide Superlattices. *Nat. Mater.* **2014**, *13*, 168−172.
(267) Termentzidis, K.; Barreteau, T.; Ni, Y.; Merabia, S.; Zianni, X.; Chalopin, Y.; Chantrenne, P.; Volz, S. Modulated SiC Nanowires: Molecular Dynamics Study of Their Thermal Properties. *Phys. Rev. B: Condens. Matter Mater. Phys.* **2013**, *87*, 125410.
(268) Lee, J.; Lee, W.; Wehmeyer, G.; Dhuey, S.; Olynick, D. L.; Cabrini, S.; Dames, C.; Urban, J. J.; Yang, P. Investigation of Phonon Coherence and Backscattering Using Silicon Nanomeshes. *Nat. Commun.* **2017**, *8*, 14054.
(269) Lim, J.; Wang, H.-T.; Tang, J.; Andrews, S. C.; So, H.; Lee, J.; Lee, D. H.; Russell, T. P.; Yang, P. Simultaneous Thermoelectric Property Measurement and Incoherent Phonon Transport in Holey Silicon. *ACS Nano* **2016**, *10*, 124−132.
(270) Anufriev, R.; Nomura, M. Thermal Conductance Boost in Phononic Crystal Nanostructures. *Phys. Rev. B: Condens. Matter Mater. Phys.* **2015**, *91*, 245417.
(271) Alaie, S.; Goettler, D. F.; Su, M.; Leseman, Z. C.; Reinke, C. M.; El-Kady, I. Thermal Transport in Phononic Crystals and the Observation of Coherent Phonon Scattering at Room Temperature. *Nat. Commun.* **2015**, *6*, 7228.
(272) Tang, J.; Wang, H. T.; Lee, D. H.; Fardy, M.; Huo, Z.; Russell, T. P.; Yang, P. Holey Silicon as an Efficient Thermoelectric Material. *Nano Lett.* **2010**, *10*, 4279−4283.
(273) Hopkins, P. E.; Reinke, C. M.; Su, M. F.; Olsson, R. H.; Shaner, E. a.; Leseman, Z. C.; Serrano, J. R.; Phinney, L. M.; El-Kady, I. Reduction in the Thermal Conductivity of Single Crystalline Silicon by Phononic Crystal Patterning. *Nano Lett.* **2011**, *11*, 107−112.
(274) Jain, A.; Yu, Y. J.; McGaughey, A. J. H. Phonon Transport in Periodic Silicon Nanoporous Films with Feature Sizes Greater than 100 nm. *Phys. Rev. B: Condens. Matter Mater. Phys.* **2013**, *87*, 195301.
(275) Ravichandran, N. K.; Minnich, A. J. Coherent and Incoherent Thermal Transport in Nanomeshes. *Phys. Rev. B: Condens. Matter Mater. Phys.* **2014**, *89*, 205432.
(276) Prasher, R. Thermal Conductivity of Tubular and Core/Shell Nanowires. *Appl. Phys. Lett.* **2006**, *89*, 063121.
(277) Yang, R.; Chen, G.; Dresselhaus, M. S. Thermal Conductivity Modeling of Core-Shell and Tubular Nanowires. *Nano Lett.* **2005**, *5*, 1111−1115.
(278) Pokatilov, E. P.; Nika, D. L.; Balandin, A. A. Acoustic-Phonon Propagation in Rectangular Semiconductor Nanowires with Elastically Dissimilar Barriers. *Phys. Rev. B: Condens. Matter Mater. Phys.* **2005**, *72*, 113311.
(279) Hu, M.; Zhang, X.; Giapis, K. P.; Poulikakos, D. Thermal Conductivity Reduction in Core-Shell Nanowires. *Phys. Rev. B: Condens. Matter Mater. Phys.* **2011**, *84*, 085442.
(280) Chen, J.; Zhang, G.; Li, B. Phonon Coherent Resonance and Its Effect on Thermal Transport in Core-Shell Nanowires. *J. Chem. Phys.* **2011**, *135*, 104508.
(281) Hu, M.; Giapis, K. P.; Goicochea, J. V.; Zhang, X.; Poulikakos, D. Significant Reduction of Thermal Conductivity in Si/Ge Core-Shell Nanowires. *Nano Lett.* **2011**, *11*, 618−623.
(282) Kang, J.; Roh, J. W.; Shim, W.; Ham, J.; Noh, J.-S.; Lee, W. Reduction of Lattice Thermal Conductivity in Single Bi-Te Core/Shell Nanowires with Rough Interface. *Adv. Mater.* **2011**, *23*, 3414−3419.

DOI: 10.1021/acs.chemrev.8b00627
Chem. Rev. XXXX, XXX, XXX−XXX

(283) Chen, J.; Zhang, G.; Li, B. Impacts of Atomistic Coating on Thermal Conductivity of Germanium Nanowires. *Nano Lett.* **2012**, *12*, 2826−2832.
(284) Kim, J.; Kim, G.; Bahk, J. H.; Noh, J. S.; Lee, W. Enhanced Thermoelectric Properties in Bi/Te Core/Shell Heterostructure Nanowires through Strain and Interface Engineering. *Nano Energy* **2017**, *32*, 520−525.
(285) Chen, Y.; Li, D.; Lukes, J. R.; Ni, Z.; Chen, M. Minimum Superlattice Thermal Conductivity from Molecular Dynamics. *Phys. Rev. B: Condens. Matter Mater. Phys.* **2005**, *72*, 174302.
(286) Hu, M.; Poulikakos, D. Si/Ge Superlattice Nanowires with Ultralow Thermal Conductivity. *Nano Lett.* **2012**, *12*, 5487−5494.
(287) Mu, X.; Wang, L.; Yang, X.; Zhang, P.; To, A. C.; Luo, T. Ultra-Low Thermal Conductivity in Si/Ge Hierarchical Superlattice Nanowire. *Sci. Rep.* **2015**, *5*, 16697.
(288) Zaslavsky, G. M. Chaos, Fractional Kinetics, and Anomalous Transport. *Phys. Rep.* **2002**, *371*, 461−580.
(289) Li, B.; Wang, J. Anomalous Heat Conduction and Anomalous Diffusion in One-Dimensional Systems. *Phys. Rev. Lett.* **2003**, *91*, 044301.
(290) Lepri, S.; Livi, R.; Politi, A. Thermal Conduction in Classical Low-Dimensional Lattices. *Phys. Rep.* **2003**, *377*, 1−80.
(291) Ponomareva, I.; Srivastava, D.; Menon, M. Thermal Conductivity in Thin Silicon Nanowires: Phonon Confinement Effect. *Nano Lett.* **2007**, *7*, 1155−1159.
(292) Donadio, D.; Galli, G. Temperature Dependence of the Thermal Conductivity of Thin Silicon Nanowires. *Nano Lett.* **2010**, *10*, 847−851.
(293) Zhou, Y.; Zhang, X.; Hu, M. Nonmonotonic Diameter Dependence of Thermal Conductivity of Extremely Thin Si Nanowires: Competition between Hydrodynamic Phonon Flow and Boundary Scattering. *Nano Lett.* **2017**, *17*, 1269−1276.
(294) Yang, Y.; Pradel, K. C.; Jing, Q.; Wu, J. M.; Zhang, F.; Zhou, Y.; Zhang, Y.; Wang, Z. L. Thermoelectric Nanogenerators Based on Single Sb-Doped ZnO Micro/Nanobelts. *ACS Nano* **2012**, *6*, 6984−6989.
(295) Kim, J. R.; So, H. M.; Park, J. W.; Kim, J. J.; Kim, J.; Lee, C. J.; Lyu, S. C. Electrical Transport Properties of Individual Gallium Nitride Nanowires Synthesized by Chemical-Vapor-Deposition. *Appl. Phys. Lett.* **2002**, *80*, 3548−3550.
(296) Xiang, B.; Wang, P.; Zhang, X.; Dayeh, S. A.; Aplin, D. P. R.; Soci, C.; Yu, D.; Wang, D. Rational Synthesis of p-Type Zinc Oxide Nanowire Arrays Using Simple Chemical Vapor Deposition. *Nano Lett.* **2007**, *7*, 323−328.
(297) Brockway, L.; Vasiraju, V.; Asayesh-Ardakani, H.; Shahbazian-Yassar, R.; Vaddiraju, S. Thermoelectric Properties of Large-Scale Zn_3P_2 Nanowire Assemblies. *Nanotechnology* **2014**, *25*, 145401.
(298) Wong, K. W.; Zhou, X. T.; Au, F. C. K.; Lai, H. L.; Lee, C. S.; Lee, S. T. Field-Emission Characteristics of SiC Nanowires Prepared by Chemical-Vapor Deposition. *Appl. Phys. Lett.* **1999**, *75*, 2918.
(299) Pradhan, S. K.; Reucroft, P. J.; Yang, F.; Dozier, A. Growth of TiO_2 Nanorods by Metalorganic Chemical Vapor Deposition. *J. Cryst. Growth* **2003**, *256*, 83−88.
(300) Wang, D.; Dai, H. Low-Temperature Synthesis of Single-Crystal Germanium Nanowires by Chemical Vapor Deposition. *Angew. Chem., Int. Ed.* **2002**, *41*, 4783−4786.
(301) Tang, Y. B.; Chen, Z. H.; Song, H. S.; Lee, C. S.; Cong, H. T.; Cheng, H. M.; Zhang, W. J.; Bello, I.; Lee, S. T. Vertically Aligned p-Type Single-Crystalline GaN Nanorod Arrays on n-Type Si for Heterojunction Photovoltaic Cells. *Nano Lett.* **2008**, *8*, 4191−4195.
(302) Dávila, D.; Tarancón, A.; Calaza, C.; Salleras, M.; Fernández-Regúlez, M.; San Paulo, A.; Fonseca, L. Monolithically Integrated Thermoelectric Energy Harvester Based on Silicon Nanowire Arrays for Powering Micro/Nanodevices. *Nano Energy* **2012**, *1*, 812−819.
(303) Calaza, C.; Salleras, M.; Dávila, D.; Tarancón, A.; Morata, A.; Santos, J. D.; Gadea, G.; Fonseca, L. Bottom-up Silicon Nanowire Arrays for Thermoelectric Harvesting. *Mater. Today Proc.* **2015**, *2*, 675−679.
(304) Dávila, D.; Huber, R.; Hierold, C. Bottom-up Silicon Nanowire-Based Thermoelectric Microgenerators. *J. Phys.: Conf. Ser.* **2015**, *660*, 012101.
(305) Abramson, A. R.; Kim, W. C.; Huxtable, S. T.; Yan, H.; Wu, Y.; Majumdar, A.; Tien, C. L.; Yang, P. Fabrication and Characterization of a Nanowire/Polymer-Based Nanocomposite for a Prototype Thermoelectric Device. *J. Microelectromech. Syst.* **2004**, *13*, 505−513.
(306) Pennelli, G.; Piotto, M. Fabrication and Characterization of Silicon Nanowires with Triangular Cross Section. *J. Appl. Phys.* **2006**, *100*, 054507.
(307) Martinez, J.; Martínez, R. V.; Garcia, R. Silicon Nanowire Transistors with a Channel Width of 4 nm Fabricated by Atomic Force Microscope Nanolithography. *Nano Lett.* **2008**, *8*, 3636−3639.
(308) Pennelli, G. Top down Fabrication of Long Silicon Nanowire Devices by Means of Lateral Oxidation. *Microelectron. Eng.* **2009**, *86*, 2139−2143.
(309) Kong, Q.; Kim, D.; Liu, C.; Yu, Y.; Su, Y.; Li, Y.; Yang, P. Directed Assembly of Nanoparticle Catalysts on Nanowire Photoelectrodes for Photoelectrochemical CO_2 Reduction. *Nano Lett.* **2016**, *16*, 5675−5680.
(310) Mårtensson, T.; Carlberg, P.; Borgström, M.; Montelius, L.; Seifert, W.; Samuelson, L. Nanowire Arrays Defined by Nanoimprint Lithography. *Nano Lett.* **2004**, *4*, 699−702.
(311) Li, Y.; Buddharaju, K.; Singh, N.; Lo, G. Q.; Lee, S. J. Chip-Level Thermoelectric Power Generators Based on High-Density Silicon Nanowire Array Prepared With Top-Down CMOS Technology. *IEEE Electron Device Lett.* **2011**, *32*, 674−676.
(312) Li, Y.; Buddharaju, K.; Tinh, B. C.; Singh, N.; Lee, S. J. Improved Vertical Silicon Nanowire Based Thermoelectric Power Generator With Polyimide Filling. *IEEE Electron Device Lett.* **2012**, *33*, 715−717.
(313) Curtin, B. M.; Fang, E. W.; Bowers, J. E. Highly Ordered Vertical Silicon Nanowire Array Composite Thin Films for Thermoelectric Devices. *J. Electron. Mater.* **2012**, *41*, 887−894.
(314) Yan, J.; Liao, X.; Yan, D.; Chen, Y. Review of Micro Thermoelectric Generator. *J. Microelectromech. Syst.* **2018**, *27*, 1−18.
(315) Routkevitch, D.; Tager, A. A.; Haruyama, J.; Almawlawi, D.; Moskovits, M.; Xu, J. M. Nonlithographic Nano-Wire Arrays: Fabrication, Physics, and Device Applications. *IEEE Trans. Electron Devices* **1996**, *43*, 1646−1658.
(316) Rabin, O.; Herz, P. R.; Lin, Y.-M.; Akinwande, A. I.; Cronin, S. B.; Dresselhaus, M. S. Formation of Thick Porous Anodic Alumina Films and Nanowire Arrays on Silicon Wafers and Glass. *Adv. Funct. Mater.* **2003**, *13*, 631−638.
(317) Martín-González, M.; Snyder, G. J.; Prieto, A. L.; Gronsky, R.; Sands, T.; Stacy, A. M. Direct Electrodeposition of Highly Dense 50 nm $Bi_2Te_{3-y}Se_y$ Nanowire Arrays. *Nano Lett.* **2003**, *3*, 973−977.
(318) Martín-González, M.; Prieto, A. L.; Gronsky, R.; Sands, T.; Stacy, A. M. High-Density 40 nm Diameter Sb-Rich $Bi_{2x}Sb_xTe_3$ Nanowire Arrays. *Adv. Mater.* **2003**, *15*, 1003−1006.
(319) Huber, C. A.; Huber, T. E.; Sadoqi, M.; Lubin, J. A.; Manalis, S.; Prater, C. B. Nanowire Array Composites. *Science* **1994**, *263*, 800−802.
(320) Zhang, Z.; Ying, J. Y.; Dresselhaus, M. S. Bismuth Quantum-Wire Arrays Fabricated by a Vacuum Melting and Pressure Injection Process. *J. Mater. Res.* **1998**, *13*, 1745−1748.
(321) Keyani, J.; Stacy, A. M.; Sharp, J. Assembly and Measurement of a Hybrid Nanowire-Bulk Thermoelectric Device. *Appl. Phys. Lett.* **2006**, *89*, 233106.
(322) Li, X.; Bohn, P. W. Metal-Assisted Chemical Etching in HF/H_2O_2 Produces Porous Silicon. *Appl. Phys. Lett.* **2000**, *77*, 2572.
(323) Huang, Z.; Zhang, X.; Reiche, M.; Liu, L.; Lee, W.; Shimizu, T.; Senz, S.; Gösele, U. Extended Arrays of Vertically Aligned Sub-10 nm Diameter [100] Si Nanowires by Metal-Assisted Chemical Etching. *Nano Lett.* **2008**, *8*, 3046−3051.
(324) Zhang, M. L.; Peng, K. Q.; Fan, X.; Jie, J. S.; Zhang, R. Q.; Lee, S. T.; Wong, N. B. Preparation of Large-Area Uniform Silicon Nanowires Arrays through Metal-Assisted Chemical Etching. *J. Phys. Chem. C* **2008**, *112*, 4444−4450.

DOI: 10.1021/acs.chemrev.8b00627
Chem. Rev. XXXX, XXX, XXX−XXX

(325) Huang, Z.; Geyer, N.; Werner, P.; de Boor, J.; Gösele, U. Metal-Assisted Chemical Etching of Silicon: A Review. *Adv. Mater.* **2011**, *23*, 285−308.
(326) Wu, S.; Zhang, T.; Zheng, R.; Cheng, G. Facile Morphological Control of Single-Crystalline Silicon Nanowires. *Appl. Surf. Sci.* **2012**, *258*, 9792−9799.
(327) Coates, N. E.; Yee, S. K.; McCulloch, B.; See, K. C.; Majumdar, A.; Segalman, R. A.; Urban, J. J. Effect of Interfacial Properties on Polymer-Nanocrystal Thermoelectric Transport. *Adv. Mater.* **2013**, *25*, 1629−1633.
(328) Yee, S. K.; Coates, N. E.; Majumdar, A.; Urban, J. J.; Segalman, R. A. Thermoelectric Power Factor Optimization in PEDOT:PSS Tellurium Nanowire Hybrid Composites. *Phys. Chem. Chem. Phys.* **2013**, *15*, 4024.
(329) Sahu, A.; Russ, B.; Su, N. C.; Forster, J. D.; Zhou, P.; Cho, E. S.; Ercius, P.; Coates, N. E.; Segalman, R. A.; Urban, J. J. Bottom-up Design of de Novo Thermoelectric Hybrid Materials Using Chalcogenide Resurfacing. *J. Mater. Chem. A* **2017**, *5*, 3346−3357.
(330) Rasool, K.; Rafiq, M. A.; Li, C. B.; Krali, E.; Durrani, Z. A. K.; Hasan, M. M. Enhanced Electrical and Dielectric Properties of Polymer Covered Silicon Nanowire Arrays. *Appl. Phys. Lett.* **2012**, *101*, 023114.
(331) Zhou, C.; Dun, C.; Wang, Q.; Wang, K.; Shi, Z.; Carroll, D. L.; Liu, G.; Qiao, G. Nanowires as Building Blocks to Fabricate Flexible Thermoelectric Fabric: The Case of Copper Telluride Nanowires. *ACS Appl. Mater. Interfaces* **2015**, *7*, 21015−21020.
(332) Chen, Y.; Zhao, Y.; Liang, Z. Solution Processed Organic Thermoelectrics: Towards Flexible Thermoelectric Modules. *Energy Environ. Sci.* **2015**, *8*, 401−422.
(333) Dames, C. Cost Optimization of Thermoelectric Materials for Power Generation: The Case for ZT at (Almost) Any Cost. *Scr. Mater.* **2016**, *111*, 16−22.
(334) LeBlanc, S.; Yee, S. K.; Scullin, M. L.; Dames, C.; Goodson, K. E. Material and Manufacturing Cost Considerations for Thermoelectrics. *Renewable Sustainable Energy Rev.* **2014**, *32*, 313−327.
(335) Yee, S. K.; Leblanc, S.; Goodson, K. E.; Dames, C. $ per W Metrics for Thermoelectric Power Generation: Beyond ZT. *Energy Environ. Sci.* **2013**, *6*, 2561−2571.
(336) Bahk, J.-H.; Fang, H.; Yazawa, K.; Shakouri, A. Flexible Thermoelectric Materials and Device Optimization for Wearable Energy Harvesting. *J. Mater. Chem. C* **2015**, *3*, 10362−10374.
(337) Russ, B.; Glaudell, A.; Urban, J. J.; Chabinyc, M. L.; Segalman, R. A. Organic Thermoelectric Materials for Energy Harvesting and Temperature Control. *Nat. Rev. Mater.* **2016**, *1*, 16050.
(338) Kim, G.-H.; Shao, L.; Zhang, K.; Pipe, K. P. Engineered Doping of Organic Semiconductors for Enhanced Thermoelectric Efficiency. *Nat. Mater.* **2013**, *12*, 719−723.
(339) Choi, J.; Lee, J. Y.; Lee, S.-S.; Park, C. R.; Kim, H. High-Performance Thermoelectric Paper Based on Double Carrier-Filtering Processes at Nanowire Heterojunctions. *Adv. Energy Mater.* **2016**, *6*, 1502181.
(340) Choi, J.; Jung, Y.; Yang, S. J.; Oh, J. Y.; Oh, J.; Jo, K.; Son, J. G.; Moon, S. E.; Park, C. R.; Kim, H. Flexible and Robust Thermoelectric Generators Based on All-Carbon Nanotube Yarn without Metal Electrodes. *ACS Nano* **2017**, *11*, 7608−7614.

DOI: 10.1021/acs.chemrev.8b00627
Chem. Rev. XXXX, XXX, XXX−XXX